

7.6.4 Formation of Mixed Oxide

Discussion of phases containing sodium, rhodium and oxygen where the oxidation state of rhodium is greater than 3 is warranted at this stage. Scheer et al. [18] during their investigation of species formed from platinum metals and alkali oxide found that oxides of the type ABO_2 and A_2BO_4 are formed. Here, A is the alkali ion and B is the platinum group metal ion. Most of the compounds formed are of the type A_2BO_4 and are formed by heating a mixture of platinum group metal and alkali carbonate to 1000C under oxygen for 20 hours. The only rhodium compound was Li_2RhO_4 . $LiRhO_2$ was formed first, and then converted to Li_2RhO_4 . For the mixed oxides containing sodium, only $NaRhO_2$ was formed. The phase Na_2RhO_4 has not been reported in literature in the 30 years since the investigation of Scheer et al. [18]. The reason for absence of A_2BO_4 compounds containing Rh and Na is not clear. The possible reason for non-existence of other compounds of rhodium and sodium oxide may be the absence of oxidation states of rhodium higher than +3. This is relevant to the current investigation, since higher consumption of hydrogen in a TPR spectra can be explained by the presence of mixed oxides containing one transition metal in a higher oxidation state. The amount of hydrogen consumed in the reduction of these catalysts increase with the amount of sodium added. However, when compared to the data of Houalla et al. [19-21] the observed changes are very small. Hence this increase in the hydrogen consumption is not due to increase in the oxidation state of rhodium.

7.6.5 Ensemble Requirement

Thus the overall effect of addition of sodium is to block the rhodium hydrogenation sites. This not only decreases the activity substantially but also reduces the size of many ensembles. A fixed number of rhodium metal atoms in an ensemble required to form hydrocarbons [22,23]. However the ensemble requirement for

CO insertion reaction is less stringent than that for hydrocarbon sites²⁴. Because sodium blocks some of the surface sites, the number of ensembles large enough for hydrocarbon formation decrease faster than the number of sites available for CO insertion and MeOH formation. This causes drastic changes in the reactivity and minor changes in the selectivity.

7.7 Conclusions

The addition of sodium to Rh/Al₂O₃ decreases the rate of CO hydrogenation. The rate decrease exponentially with the amount of sodium added. The selectivity to oxygenates is increased slightly.

Hydrogen chemisorption and XRD shows that addition of sodium poisons blocks or poisons the rhodium crystallite. The rhodium is in metallic state under reaction conditions and the oxidation state of sodium is not changed. The formation of gem-dicarbonyl species is hindered due to the lower amount of surface -OH groups. XPS and IR results show that hexa methyl disilazane reacts with the surface -OH groups to form surface silanes. These silylated catalysts show that the formation of the gem-dicarbonyl species is hindered.

REFERENCES

1. D.G. Blackmond, J.A. Williams, S. Kesraoui and D.S. Blazewick. *J. Catal.* 1986, 101, 496.
2. B.D. Cullity. "Elements of X-Ray Diffraction", Addison-Wesley, Reading, Massachusetts, 1978.
3. J.L. Maitre, P. Govind Menon and F. Delannay, in "Characterization of Heterogeneous Catalysts". Ed. F. Delannay, Marcel Dekker, New York, 1984.
4. "Powder Diffraction File". Alphabetical Index, Inorganic Phases, International Center for Diffraction Data, Swarthmore, Pennsylvania, 1987.
5. H. Arakawa, K. Takeuchi, T. Matsuzaki and Y. Suge, *Chem. Letts. Japan.* 1984, 1607.
6. F. Solymosi, M. Pasztor and G. Rakhely, *J. Phys. Chem.* 1988, 110, 413.
7. P. Basu, D. Panayotov, and J.T. Yates, Jr., *J. Phys. Chem.* 1987, 91, 3133.
8. C.H. Dai and S.D. Worley, *J. Phys. Chem.* 1986, 90, 4219.
9. J.Z. Shyu, J.G. Goodwin, Jr., and D.M. Hercules, *J. Phys. Chem.* 1985, 89, 4983.
10. M.I. Zaki, G. Kunzmann, B.C. Gates and H. Knozinger, *J. Phys. Chem.* 1987, 91, 1486.
11. C.D. Wagner, W.N. Riggs, L.E. Davis, J.F. Moulders and G.E. Mullenberg. "Handbook of X-ray Photoelectron Spectroscopy". Perkin-Elmer Co., Eden Prairie, Minnesota, 1979.
12. T.P. Wilson, W.J. Bartley and P.C. Ellgen. "Advances in Catalytic Chemistry", Proc. Conf. in Salt Lake City, Utah, 1982.
13. H. Knozinger and P. Ratnaswamy, *Cat. Rev. Sci. Eng.* 1978, 17, 31.

14. J.A. Konvalinka, P.H. Van Oeffelt and J.J.F. Scholten. *Appl. Catal.* 1981. 1. 141.
15. J. LeMaitre. in "Characterization of Heterogeneous Catalysts". Ed. F. Delannay. Marcel Dekker. New York, 1984.
16. M. McLaughlin and R.D. Gonzalez. *J. Catal.* 1984. 89. 392.
17. S.C. Chuang, J.G. Goodwin, Jr. and I. Wender. *J. Catal.* 1985. 95. 435.
18. J.J. Scheer, A.E. van Arkel and R.D. Heyding. *Can. J. Chem.* 1955. 33. 683.
19. M. Houalla, F. Delannay and B. Delmon. *J. Phys. Chem.* 1981. 85. 1704.
20. M. Houalla, J. LeMaitre and B. Delmon, *C. R. Acad. Sci. Paris. Ser. C.* 1979. 289. 77.
21. M. Houalla, J. LeMaitre and B. Delmon. *J. Chem. Soc., Faraday Tans.1.* 1981. 78, 1389.
22. W.M.H. Sachtler. 8th Intl. Congr. Catal. 1984, Vol. I. 151. Berlin.
23. G.A. Somorjai. *Chemical Reviews* 1984, 321.
24. W.M.H. Sachtler. *Faraday Discuss.* 1978. 7.

CHAPTER 8

PERFORMANCE OF MOLYBDENA MODIFIED RHODIUM/ALUMINA CATALYSTS

The effect of addition of molybdena on the performance of Rh/Al₂O₃ catalysts is investigated. First catalysts containing different loading of Mo were investigated. Then, the products are separated according to their rank. The activation energies and the power law indices for the rate expressions were also calculated.

8.1 Catalyst Preparation

The catalysts support used was CATAPAL alumina extrudate. The alumina extrudate was first ground to a particle size of 60-100 mesh. The support was then calcined at 500C under flowing air (> 99.999% purity) for two hours. The surface area of the support is about 200 m²/gm. The details of preparation of Rh/Al₂O₃ catalysts are given in chapter 5. A no-excess impregnation technique was used to support rhodium and molybdenum salts on the support. The rhodium was impregnated from a sulfate-free acidic solution (pH=1) from Engelhard. Molybdenum was impregnated using Puratronic grade ammonium molybdate from Alfa Products. All Rhodium was nominally 3 wt.%.

The molybdena-containing catalysts were prepared in stages. In the first stage, Mo was deposited on the alumina using a molybdena solution at a pH of 1-2. The impregnated sample was kept at room temperature for 30-60 minutes, in an oven at 110C for 12-16 hours. The catalysts were later air calcined at 500C for 2 hours. The 2.8 wt. % Mo catalyst was prepared by coimpregnation. All

% Mo numbers quoted are for Mo metal by weight although the Mo is present in an oxide form. In the preparation of 2.8 % Mo catalyst, a white precipitate was formed when Mo solution was added to the rhodium nitrate solution. This precipitate dissolved immediately on shaking. So the addition of ammonium molybdate solution to rhodium nitrate solution was continued drop-wise with vigorous shaking. After addition of three-fourths of the molybdenum solution, further addition of molybdate solution formed a precipitate that did not dissolve on shaking. So, small amounts of concentrated nitric acid was added. Addition of nitric acid dissolved the precipitate and the solution was once again clear. The 7.5 wt. % and 15 wt. % Mo catalyst were prepared by sequential impregnation. First the molybdenum salts were impregnated, followed by drying in air at 110C and air calcination at 500C. Then the rhodium salt was impregnated using rhodium nitrate solution using a no-excess solution impregnation technique. The color of the catalysts on Mo impregnation and after calcination was white. In contrast, the color of catalysts after rhodium impregnation was bright yellow and reddish brown after calcination.

The theory of impregnation of salts from aqueous solution and its relevance to catalysts preparation is discussed in chapter 2. However some results from this theory will be discussed here. Since molybdenum forms anions in solution, molybdenum was impregnated first. In contrast, rhodium exist as hydrated cations in the solution, and hence adsorption of rhodium cation on alumina surface in an acidic solution is not thermodynamically facilitated. In the case of 15 wt. % Mo catalysts, because of the limited solubility of the ammonium molybdate, two successive impregnations were made with a 500C air calcination in between them. Before testing, all catalysts were prereduced with flowing hydrogen with the following schedule, 200C (1/2 hour), 350C (1/2 hour) and at 500C (1 hour).

Catalyst (0.5-1gm) was tested in a flow reactor system. The flow reactor is described in detail in chapter 4 and the procedure for catalysts testing is described

in chapter 6. Unless otherwise specified, all data were obtained at hydrogen:CO ratio of two and a pressure of 30 atm. The analytical system is described in detail in chapter 3. To make activity comparisons, space rates were varied at constant temperature to obtain equal conversions (limited to 6 % CO conversion), then the conversions were obtained by normalizing to 3000 GHSV by multiplying by the factor: GHSV/3000.

8.2 Performance Testing Results

This section shows the effect of molybdena addition on the reactivity and the selectivity of molybdena modified rhodium/alumina catalysts.

8.2.1 Overall Activity and Selectivity

Table 8.1 summarizes the effect of molybdena addition. The % CO conversions given in table 8.1 are the total conversions. However % selectivities to oxygenates and hydrocarbons are % of CO converted to these products on a CO₂ free basis. The % C₂- oxyg. is the percentage of all oxygenates C₂ and above. The Mo/alumina catalysts has very low activity for CO conversion and does not form any oxygenates. The effect of incorporating increasing amounts of molybdena in the Rh/alumina system is to increase the activity for CO conversion. For example, table 8.1 shows that the catalyst with Mo/Rh atom ratio of 2.7 (Rh/7.5Mo) is 12 times as active as Rh/Al₂O₃ when compared at 3000GHSV and at 250C. The water gas shift reaction is greatly enhanced as seen by the appearance of CO₂. Also, the % CO converted to oxygenates(particularly methanol) increases sharply with increasing Mo content, rising from 29 % for Rh/Al₂O₃ to 65 % for Rh/7.5Mo/Al₂O₃ both at 250C. Oxygenates are 89 % for the Rh/15Mo/Al₂O₃ catalyst at 200C.

Table 8.1: Effect of addition of Mo on the reactivity of Rh alumina

Catalyst	T(C)	GHSV hr ⁻¹	%CO Conv.	% CO CO ₂	conv. to Oxyg. (CO ₂ free)	C2- Oxyg. % of Oxyg.
Rh/Al ₂ O ₃	250	3000	5.7	1	29	82
	275	3000	12.5	1	19	87
Rh/2.8Mo/ Al ₂ O ₃	225	3000	9.0	21	59	42
3Rh/7.5Mo Al ₂ O ₃	200	3000	7.3	24	86	17
	250	36000	5.3	25	65	27
Rh/15Mo Al ₂ O ₃	200	3000	6.0	27	89	12
	225	3000	27	37	83	14
15Mo/Al ₂ O ₃	225	3000	<1	61	0	
	250	3000	2	50	0	
	275	3000	5	51	0	

The results for Rh-Mo/Al₂O₃ with low loading of Mo are consistent with other investigations [1-8]. The Rh-Mo/Al₂O₃ catalysts derived from monometallic catalysts were less reactive than the conventional catalysts [5]. In contrast, the catalysts derived from bimetallic cluster RhMo₂CP₃(CO)₆ was more reactive than the conventional catalysts [8].

8.2.2 Product Distribution

Table 8.2 shows the detailed product distribution for Rh/Al₂O₃, Mo/Al₂O₃ and Rh-Mo/Al₂O₃ catalysts. There are significant changes in the product distribution on Mo addition to Rh/Al₂O₃ catalysts. For example, there is a steep increase in the CO₂ formed from the water gas shift reaction. Also, there is a decrease in the C₂+ oxygenate fraction of the total oxygenates. The water gas shift reaction is helpful since this permits use of syngas with lower hydrogen/CO ratios and simplifies the product separation. The complete lack of aldehydes in the product the good hydrogenation capability. The increase in the ethers may be because of the increase in surface acidity due to molybdena addition. Decreased ester formation may be due to decreased acetic acid formation because of increased hydrogenation activity. The most important observations are the drastic reduction in formation of methane, accompanied by a substantial increase in the oxygenates, especially methanol and dimethyl ether.

Further insight can be deduced from the product distribution. The addition of Mo results in oxygenates with much higher percentage of methanol. However, it is important to note that while C₂-oxygenates has decreased the %C₂-oxygenates as a percentage of CO conversion remains nearly at the same level, even though catalyst activity has increased by greater than 10-fold by Mo addition.

In comparison the product distribution for 15 % Mo/Al₂O₃ gives 50 % CO converted to CO₂ and rest to hydrocarbons at 250C with a GHSV of 3000 hr⁻¹.

Table 8.2: Product distribution on CO hydrogenation on Rh-Mo Al₂O₃ catalysts

Catalyst	Rh/Al ₂ O ₃	Rh 2.8Mo ₇ Al ₂ O ₃	Rh 15Mo ₇ Al ₂ O ₃	
Temp(C)	250	225	200	250
GHSV	3000	3000	3000	36000
%CO Conv.	6	9	7	5
% CO to CO ₂	1	22	24	25
of CO converted, % converted to:(CO ₂ free basis)				
Hydrocarbons	72	41.5	13	34
Methane	61	35	9	26
Ethane	4	4.5	3	6
Propane	5	1.5	1	2
Butane	2	0.5	0	0
Oxygenates	28	58.5	87	66
MeOH	2	13	38	16
MeOMe	1	16	30	26
MeCHO	2	0	0	0
EtOH	11	12	6	7
MeOAc	3	2.5	1	1
HOAc	0	0	0	0
EtCHO	0.4	0	0	0
n-PrOH	2.7	2.4	2	1
MeOEt	3	12.6	10	15
EtOAc	3	0	0	0
%of C2+				
Oxygenates	82	42	17	27

The overall carbon monoxide conversion under these condition was 1.8%. The carbon percentage in hydrocarbons is as follows: Methane 61%, ethane 29% and propane 10%.

The effect of the amount of molybdena addition on the selectivity to oxygenates is clearly seen from figure 8.1. In this figure the overall oxygenate selectivity on a carbon dioxide free basis is plotted against the overall conversion (including carbon dioxide). For a given catalyst the selectivity to oxygenates decreases with increasing conversion, e.g., for Rh/Al₂O₃ the selectivity to oxygenates decreases from 35 % to 20 % when the CO conversion was increased from 2% to 18%. The x-axis is the selectivity versus conversion curve for Mo/Al₂O₃ since no oxygenates are formed on this catalysts. As seen in figure 8.1 the addition of Mo to Rh/Al₂O₃ shift the selectivity versus conversion curves to higher selectivity. However the slopes of these curves do not change. Also there is an effect of temperature since the selectivity versus conversion curves are shown for different reaction temperature. The effect of reaction temperature on the selectivity to oxygenates will be discussed in detail while calculating the activation energies.

Table 8.3: Effect of Mo addition on Methane/Methanol product distribution

Catalyst	%CO to CH ₄	%total oxygen	%C2+ oxygen	Oxygenates Dist. C1	C2	C3	%CH ₄ - MeOH
Rh. Al ₂ O ₃	60	30	82	5	21	3	65
Rh/7.5Mo/ Al ₂ O ₃	24	65	27	47	17	1	74

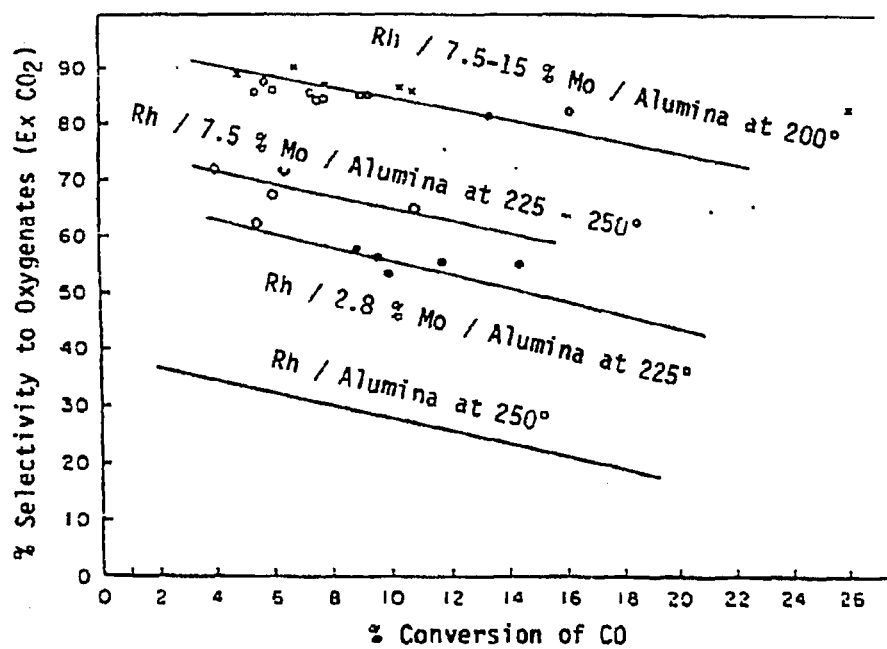


Figure 8.1: Effect of Mo addition and temperature on the selectivity to oxygenates

8.2.3 Approach to Steady State

The initial transient properties of these catalysts show interesting trends. Figure 8.2 shows the approach towards steady state of overall conversion, methane selectivity and oxygenate selectivity. The data in the figure are reported for CO hydrogenation on 3%Rh 7.5%Mo/Al₂O₃ at 200C, 30atm and hydrogen/CO=2. The initial activity of these catalysts is high as seen by the high conversion. However, these data should be interpreted with caution, since the gas phase environment at zero time is only hydrogen and at time zero, carbon monoxide feed is started. Thus the gas phase may contain a different hydrogen/CO ratio than at steady state. However, this transient in gas phase should approach the steady state feed gas composition in an hour. The overall conversion approaches a steady state within 12 hours. Subsequent steady states by changing conditions are approached within 1-2 hours. The methane selectivity also decreases with time and reaches steady state within 12 hours. However, in contrast the percent decrease in methane selectivity is much lower than the percent decrease in the overall conversion. In comparison, the total selectivity to oxygenates increases with time on stream, but the increase is very small compared to the decrease in the overall conversion. This decrease in activity is similar to those reported by Van der Berg[9].

The effect of hydrogen/CO is shown in figure 8.3 on CO hydrogenation on 3%Rh 7.5%Mo/Al₂O₃ is shown in figure 8.3. This set of data was collected at 200C, 30atm and GHSV of 3000hr⁻¹. The conversion increases with increasing hydrogen/CO ratio. this is true with many CO hydrogenation catalysts. Many of the known catalysts do not work below a Hydrogen:CO ratio of 1.

Another way to see the initial transients is to plot the log(1-CO conv.) versus space-time, as given in figure 8.4. The transients in the figure are marked by an arrow. Also, the points at space time 2.4 show the initial transients. For example

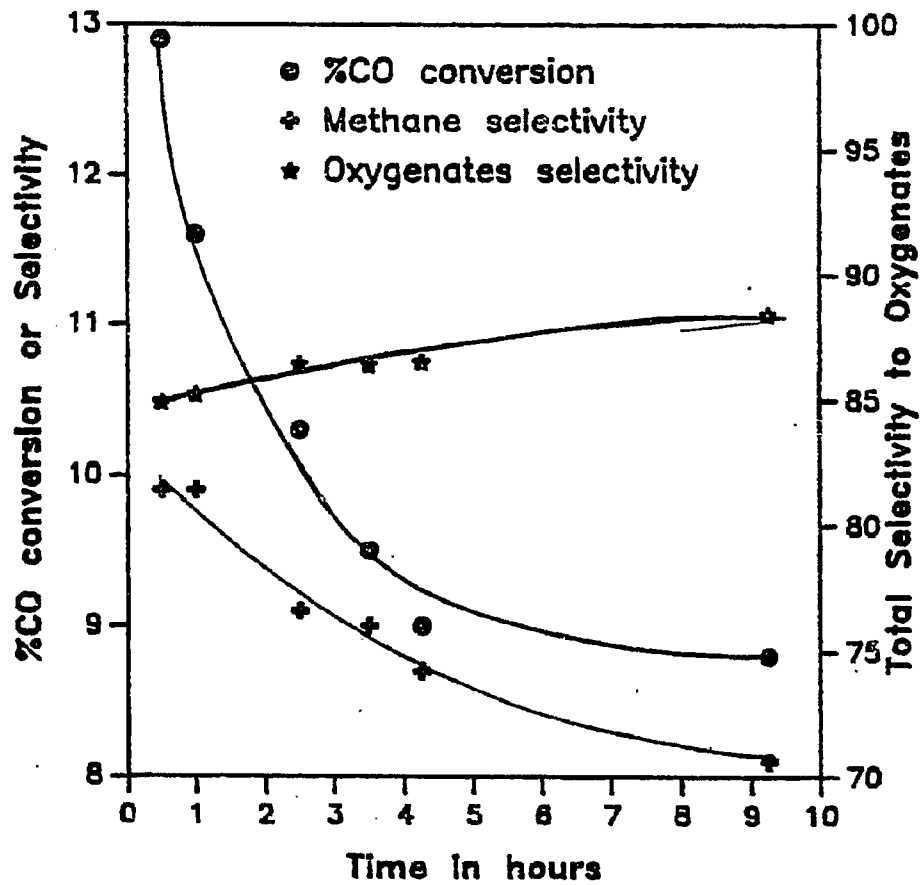


Figure 8.2: Initial transients of CO hydrogenation on 3%Rh 7.5%Mo/Al₂O₃ catalysts at 200°C, 30 atm and hydrogen/CO=2.

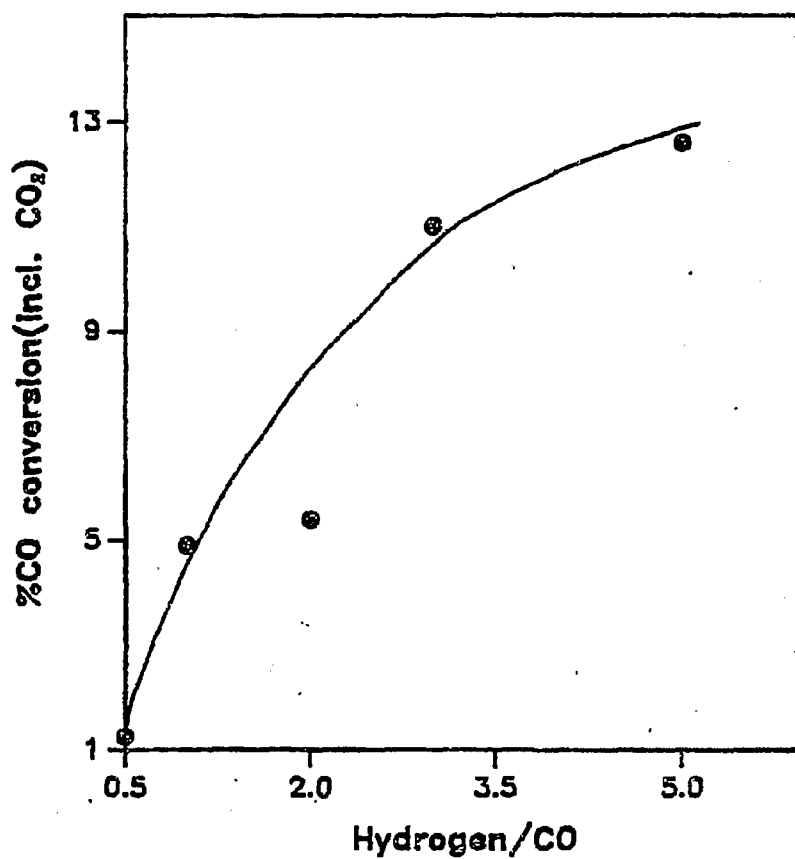


Figure 8.3: Effect of hydrogen/CO ratio on the overall conversion of 3%Rh/7.5%Mo/Al₂O₃ catalysts at 200C, 30 atm and 3000GHSV.

the point at the lowest ordinate or the highest conversion is the point at zero time, and the point move towards the steady state line.

8.3 Transport Limitations

From the calculations in appendix 1, the mass and heat transport limitations for CO hydrogenation on Rh-Na/Al₂O₃ catalysts were shown to be insignificant. Since the process parameters used in the Rh-Na/Al₂O₃ catalysts and the Rh-Mo/Al₂O₃ catalysts are nearly same, the calculations in appendix 1 are valid for the reaction study conducted in this chapter as long as the temperature is lowered to give differential conversions.. Hence the transport limitations are insignificant on CO hydrogenation on Rh-Mo/Al₂O₃ catalysts under the conditions investigated in this chapter.

8.4 Delplot Analysis

The next stage in kinetic analysis of product is to separate products according to their rank, i.e., to separate the primary, secondary and tertiary products. A new method for separation of products according to their rank was developed in chapter 4. In this section this method is applied to the kinetic analysis of carbon monoxide hydrogenation on Rh-Mo/Al₂O₃ catalysts. The basis set has only carbon monoxide since carbon monoxide is the only reactant monitored. From delplot analysis most of the products are kinetic primary products. Sometimes, it is difficult to assign rank to the product because the intercept may be small and finite. In this section first the basic delplot method will be developed, then the extended delplot will be applied to higher rank products. In the last subsection the concept of separation of regimes of product rank will be discussed.

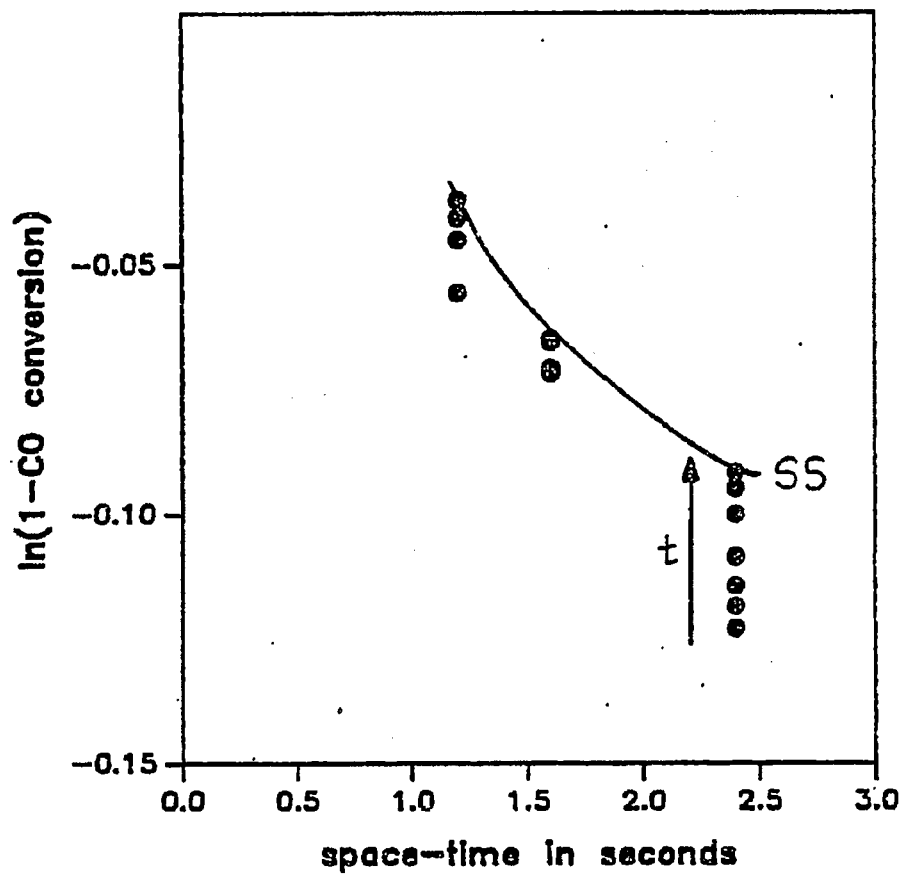


Figure 8.4: Log(1-CO conversion) versus space-time for CO hydrogenation on 3%Rh 7.5%Mo/Al₂O₃ catalysts at 200C, 30atm and hydrogen. CO = 2.

8.4.1 Basic Delplot Analysis

The basic delplot method consists of plotting mole fraction conversion against conversion. A finite intercept denotes a primary product while a zero intercept denotes a secondary product. Figure 8.5 shows the basic delplot for methane. This data was collected for CO hydrogenation on 3%Rh 7.5%Mo/Al₂O₃ catalysts at 30 atm total pressure and 200C reaction temperature. The hydrogen/CO was fixed at 5. The space velocity was varied from 1500 to 6000 hr⁻¹. The basic delplot of methane clearly shows that methane is a primary product. The delplot intercept for methane under the above conditions is 0.1. This is the ratio of the initial rate of formation of methane to the initial rate of consumption of carbon monoxide. Thus there is only one slow step in the methane formation reaction under the above mentioned conditions. The basic delplot of carbon dioxide also shows a finite intercept, this implies that carbon dioxide is a kinetic primary product. This should be compared with the results from the sodium modified catalysts, where carbon dioxide had a small intercept. The carbon dioxide is formed from the water gas shift reaction given by equation (8.1).



The reactant water is formed in methane formation, ethanol formation, ethane formation, and dimethyl ether formation. Carbon dioxide is thus formed sequentially: first water is formed then carbon dioxide is formed by the water gas shift reaction. Thus carbon dioxide can be primary product if the water gas shift reaction is fast on the process time scale. Thus the water gas shift reaction is fast on the process time scale on the molybdena modified rhodium/alumina catalysts but is slow on the process time scale on the sodium modified rhodium/alumina catalysts. The delplot intercept for carbon dioxide is 0.09.

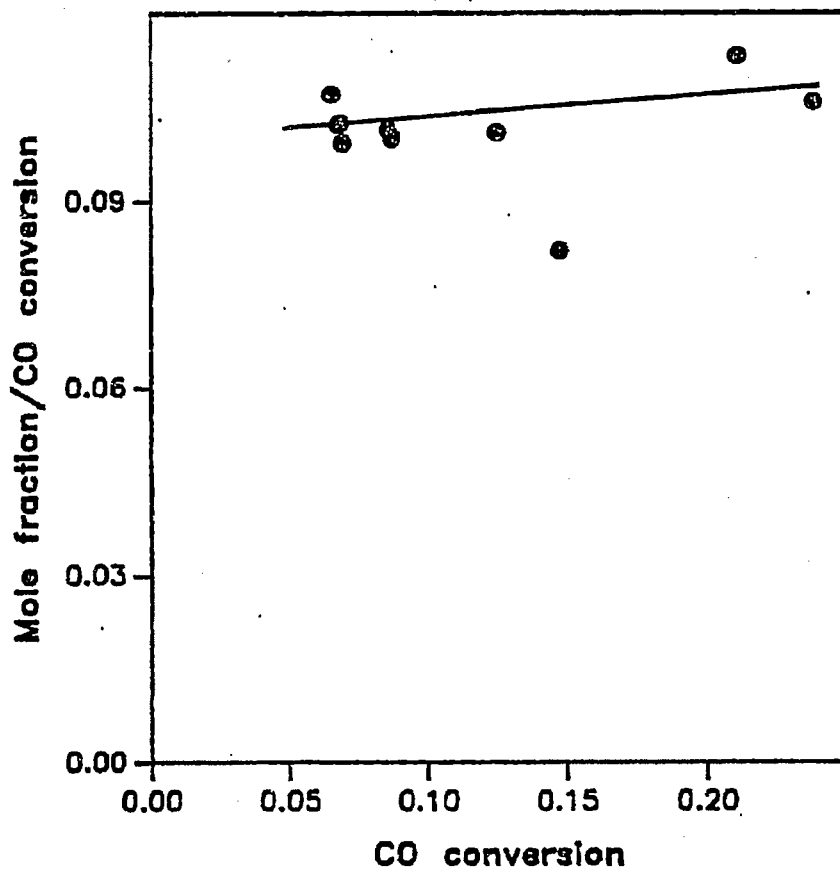


Figure 8.5: Basic delplot of methane formed on carbon monoxide hydrogenation on 3% Rh 7.5% Mo / Al₂O₃ catalysts at 200C, 30 atm. and hydrogen; CO=5

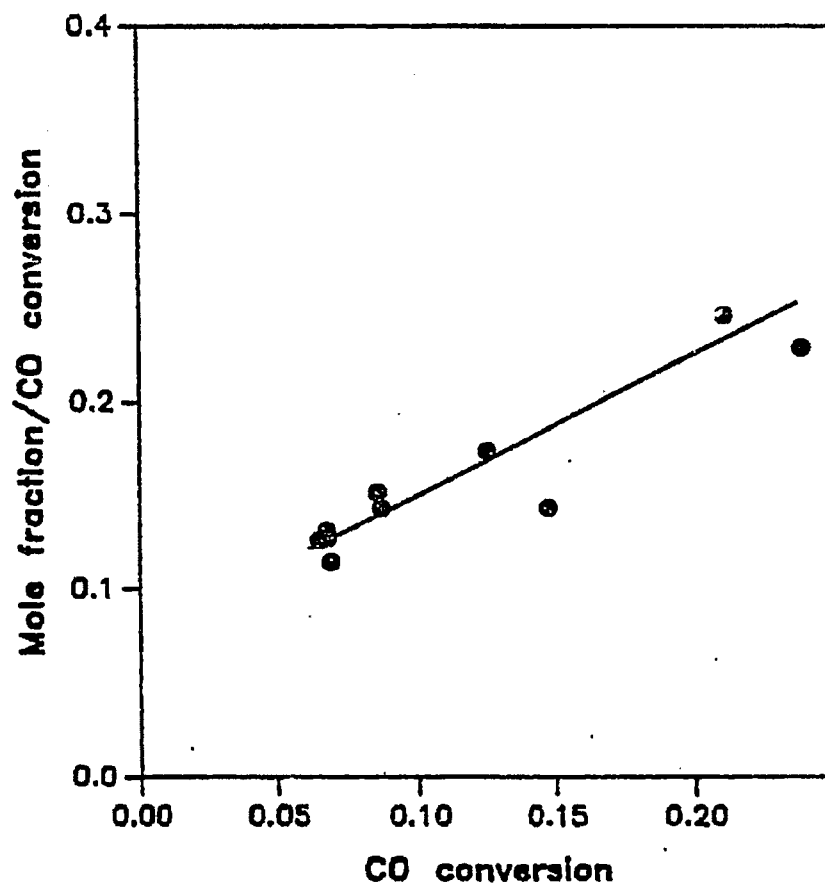


Figure 8.6: Basic delplot of carbon dioxide formed on carbon monoxide hydrogenation on 3% Rh 7.5% Mo / Al₂O₃ catalysts at 200C, 30 atm, and hydrogen/CO=5

Figure 8.7 shows the basic delplot for methanol and dimethyl ether on carbon monoxide hydrogenation with hydrogen/CO of 5. The plot shows finite intercept for both methanol and dimethyl ether, hence both methanol and dimethyl ether are primary products. Thus the formation on ethers is fast on these catalysts because of their higher acidity. In contrast, small amounts of ethers are formed on sodium modified catalysts. The large amount of methanol formed compared to dimethyl ether is reflected in the higher intercept for methanol as compared to dimethyl ether (0.45 versus 0.15). The high hydrogen/CO ratio (5) leads to higher hydrogenation of surface species and less products from recombination. This leads to a high methanol/dimethyl ether ratio. Figure 8.8 shows the basic delplot for ethanol and ethane under the above mentioned conditions. Since ethanol and ethane are formed in small amounts, their intercepts, if any are small, this makes discrimination between finite but low and zero intercepts difficult. However, figure 8.8 clearly shows that ethanol has a finite intercept. The low signal to noise in the analytical data at low conversions for some C2 and higher products prevents the discrimination between zero and small but finite intercept.

The delplot analysis can be checked for internal consistency by checking the sum of product of stoichiometric coefficients and the delplot intercepts. Table 8.4 list the delplot intercepts and the stoichiometric coefficients of each product. For example, the delplot intercept of dimethyl ether is 0.15 and its stoichiometric coefficient is 2. The stoichiometric coefficient here is easily found from the carbon balance.

Thus the sum of stoichiometrically accounted delplot intercepts, given in

$$\sum_P \nu_P^{-1} P_{CO} = 1.00 \quad (8.2)$$

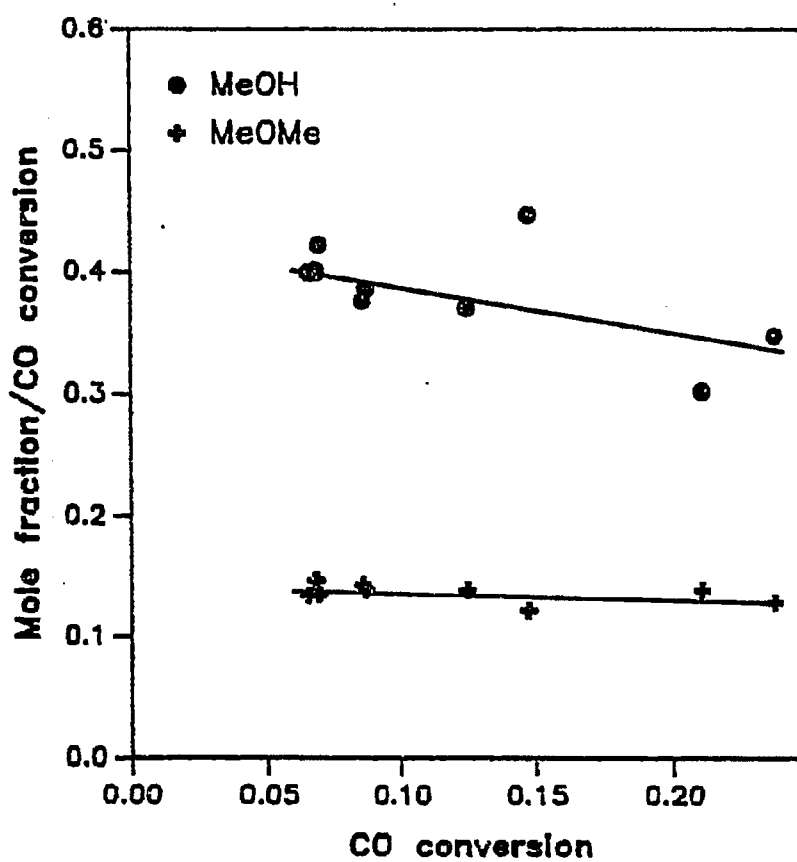


Figure 8.7: Basic delplot of methanol and dimethyl ether formed on carbon monoxide hydrogenation on 3% Rh 7.5% Mo Al_2O_3 catalysts at 200C, 30 atm. and hydrogen/CO=5

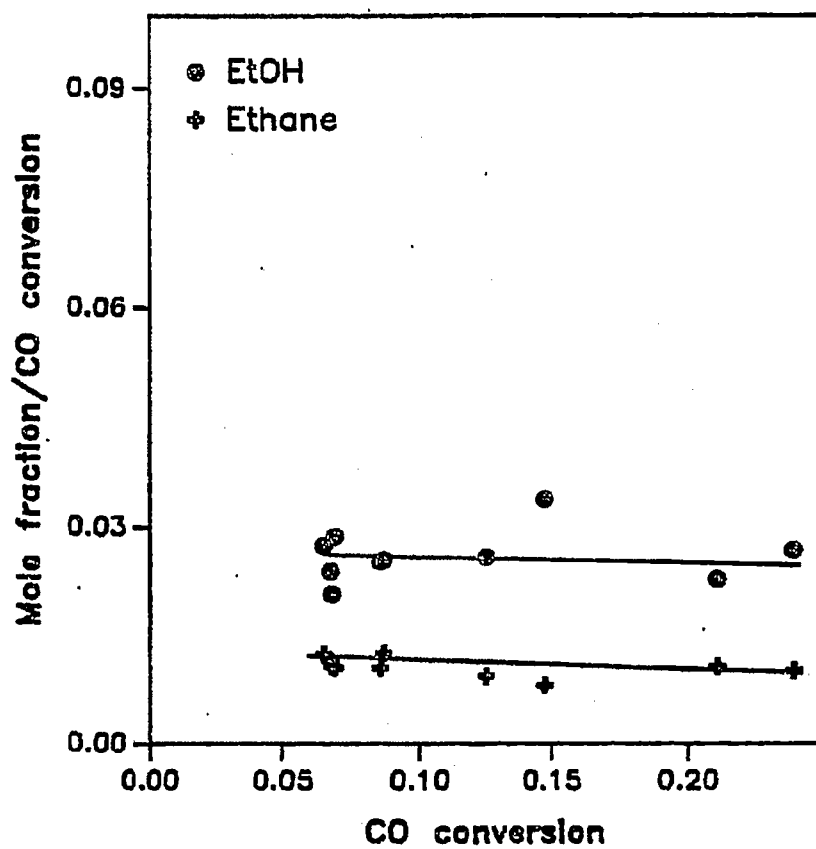


Figure 8.8: Basic delplot of ethanol and ethane formed on carbon monoxide hydrogenation on 3% Rh 7.5% Mo /Al₂O₃ catalysts at 200C, 30 atm, and hydrogen/CO=5

Table 8.4: Delplot intercepts and stoichiometric coefficients of products formed on CO hydrogenation on 3% Rh 7.5% Mo/Al₂O₃ catalysts at 200C. 30 atm and hydrogen/CO=5.

Product(P)	Delplot Int. ($^1P_{CO}$)	Type	Sto. Coeff. (ν_i)
Methane	0.1	Primary	1
CO ₂	0.08	Primary	1
Methanol	0.45	Primary	1
Ethanol	0.025	Primary	2
Dimethyl ether	0.15	Primary	2
Ethane	0.01	Primary	2

equation (8.2) is close to unity within experimental limits. Hence rule 3 of basic delplot analysis given in chapter 4 is satisfied.

8.4.2 Separation of Regimes

In the last section of chapter 4, the concept of separation of regimes was developed and quantified. A primary product is a product that has only one slow step between the reactant and itself, while a secondary product is a product which has two slow steps between reactant and itself. A reaction is slow or fast on the process time scale and not on a relative scale. Now, if the process time scale changes, then a reaction step can change from a slow step to a fast step or vice versa. The process time scale can be changed by looking at two different conversion regions.

However, this phenomenon is not seen in many products because, in a reaction network, one step is often much slower than the remaining steps. Thus to make one of the fast steps as a slow step, we have to use extremely small process time. At these low process time, the conversions are low and this causes analytical problems. However, an example of a product which changes regimes will be shown here.

The basic delplot of MeOEt is shown in figure 8.9. The figure shows two distinct regimes. The first regime is above 1.5% CO conversion where the basic delplot gives a finite intercept. In contrast, the second regime below 1.5% conversions shows a zero basic delplot intercept. Hence MeOEt is a secondary product below 1.5% CO conversion and a primary product above 1.5% conversion. Regime 1 (above 1.5% CO conversion) consists of high conversion or low space time runs, while regime 2 consists of low conversion or high space time runs. The above behavior is qualitatively and quantitatively explained using order of magnitude analysis and singular perturbation analysis in chapter 4.

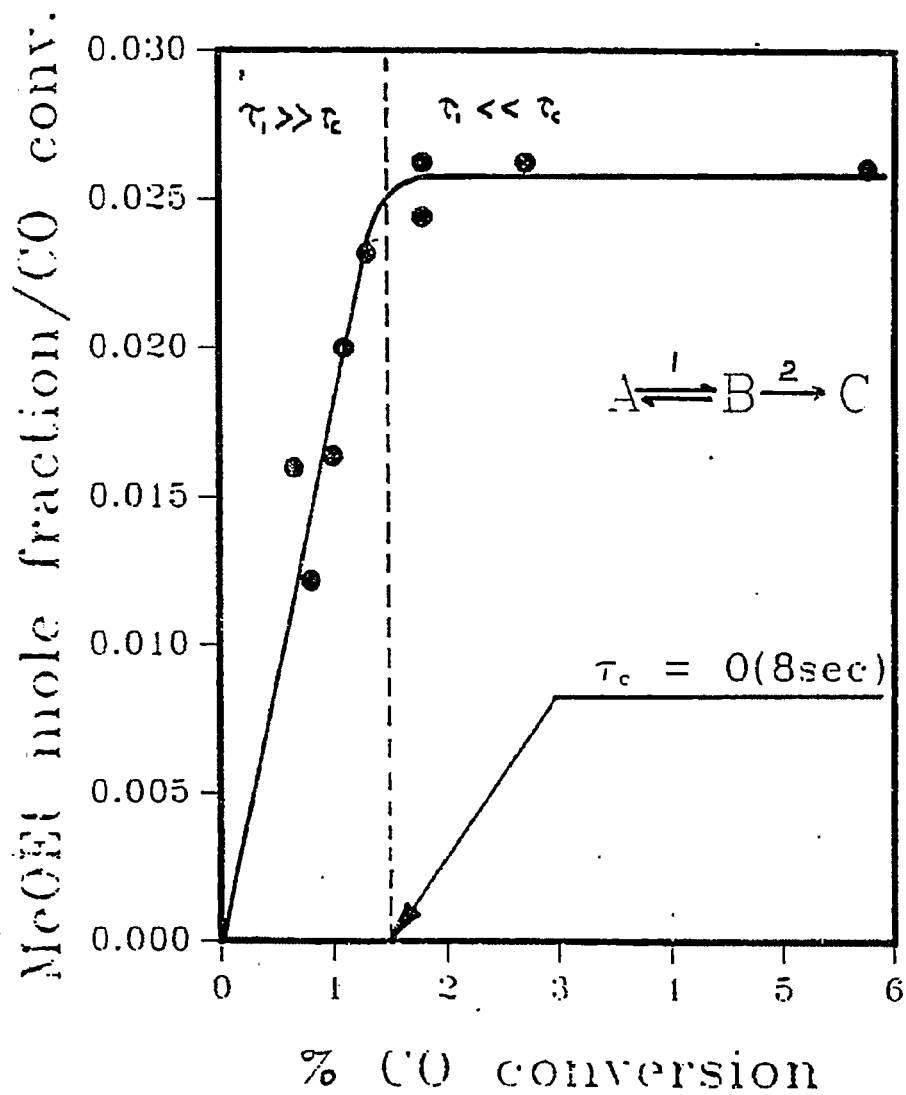


Figure 8.9: Separation of regime of rank of product using delplot analysis: basic delplot of MeOEt formed on CO hydrogenation on 3% Rh 7.5% Mo Al₂O₃ catalysts at 200C and 30atm.

8.4.3 Nature of Reaction Steps

The previous section showed that the delplot intercepts for various products of CO hydrogenation on 3%Rh 7.5%Mo/Al₂O₃ catalyst at 200C, 30atm and hydrogen/CO = 5. Thus here, the network rank of each product is same as the effective rank. Thus

$$\hat{N}(CH_4) = \hat{N}(CO_2) = \hat{N}(MeOH) = \hat{N}(C_2H_6) = \hat{N}(EtOH) = \hat{N}(MeOMe) = 1$$

and

$$\hat{E}(CH_4) = \hat{E}(CO_2) = \hat{E}(MeOH) = \hat{E}(C_2H_6) = \hat{E}(EtOH) = \hat{E}(MeOMe) = 1$$

Section 3.4 showed the use of network rank of different products to identify the number and location of slow steps in a reaction pathway. For a reaction pathway given in figure 3.2, the network rank of products under these conditions corresponds to scheme C1 or H2 in table 3.4. Thus by using simple delplot analysis the various combinations of fast and slow steps can be identified.

In scheme C1, steps 1 and 2 shown in figure 3.2 are fast while steps 3 and 4 are slow. In contrast scheme H2 consists of steps 2, 3 and 4 as fast steps while step 1 as slow. Step 1 consists of two sub-steps, the dissociation of CO and hydrogenation of "active carbon" to CH_x species. Other investigations on Ni single crystals and supported Ru catalysts have shown that the dissociation of CO on the surface is fast as compared to the hydrogenation of the "active carbon" to CH_x species.

8.5 Power Law Fit

A convenient method to study the effect of process parameters on the activity of the catalyst is to fit the overall rate and the rate of primary products as power

law of the reactants. Even though the power law model does not have as much physical significance as the Langmuir-Hinshelwood models, their ease of obtaining power law indices helps in understanding the critical issues in kinetics such as inhibition.

Table 8.5 shows the power law coefficients for various catalyst for overall rate of consumption of CO and for rates of formation of methane, methanol and carbon dioxide. For Rh/Al₂O₃ catalysts the overall rate of consumption of carbon monoxide varies as 0.8 power of partial pressure of hydrogen and as -0.3 power of partial pressure of carbon monoxide. The hydrogenation of carbon monoxide on transition metal surfaces is usually inhibited by carbon monoxide, and this leads to the negative exponent in the partial pressure of carbon monoxide. The physical significance of the negative exponent is that carbon monoxide adsorbs strongly and hence blocks hydrogen activation. In comparison, the exponent for partial pressure for carbon monoxide for Rh-Mo/Al₂O₃ catalysts is -0.03 ± 0.09 , this is significantly higher than the exponent for Rh/Al₂O₃. The percent change in the exponent for partial pressure of hydrogen is small, e.g., the exponent changes from 0.8 to 0.72 on molybdena addition. These exponents agree with the results of Underwood and Bell[10]. Thus the rate of consumption of carbon monoxide is less inhibited on Rh-Mo/Al₂O₃ catalysts than on Rh/Al₂O₃ catalysts. These results point out that the mode of interaction of Mo in Rh-Mo/Al₂O₃ catalysts is not a physical one but a chemical one. Also the role of molybdena addition to Rh/Al₂O₃ catalysts is truly a synergistic effect, because the effect of sum is much greater than the sum of effects.

8.6 Activation Energies

The next stage of kinetic analysis is to find the effect of temperature on the product distribution. As seen in figure 8.1, the selectivity is a function of

Table 8.5: Power law coefficients for Rh-Mo/Al₂O₃ and related systems

$$Rate_{species} = A P_{H_2}^x P_{CO}^y$$

Catalyst	Species	x	y	Ref.
3%Rh/Al ₂ O ₃	CO	0.8	-0.3	-
Rh/SiO ₂	CH ₄	0.7	-0.2	12
	MeOH	1.3	-0.1	12
3%Rh15%Mo/Al ₂ O ₃	CO	0.72±0.05	-0.03±0.09	+
	CH ₄	1.02±0.08	-0.32±0.09	+
	MeOH	1.53±0.01	-0.01±0.11	+
	CO-2	0.38±0.05	-0.04±0.06	+

- - this work

the amount of molybdena added and the temperature. Figure 8.10 shows the semi-log plot of approximate rate versus the reciprocal temperature. There are two assumptions in this plot. The first assumption is of differential conversions. Because the data is taken only for differential conversions, the rate of reaction is proportional to conversion if all the data is compared at the same space time or GHSV. Thus the second assumption is that all the data is normalized to a space velocity of 3000 hr^{-1} as suggested earlier. Also the contribution to the apparent activation energy from the concentration term is neglected, since the exponential term from the apparent rate constant will dominate. Thus the rate constant can be substituted by the rate. The rate can be substituted by conversion for differential conversions and for a single space rate.

Thus the slope of the line in figure 8.10 shows the apparent activation energies. This figure shows data for overall conversion for Rh/ Al_2O_3 and Rh-Mo/ Al_2O_3 catalysts. Also, the data for various product distributions is also shown. It is clear from the figure that the slope of the line for Rh/ Al_2O_3 is nearly same as that for Rh-Mo/ Al_2O_3 indicating that the overall activation energy for CO consumption is same for Rh/ Al_2O_3 and Rh-Mo/ Al_2O_3 . Thus the two order of magnitude increase in the rate of CO hydrogenation on Mo addition cannot be attributed to decrease in the activation energy for the overall reaction.

The activation energies for various product categories is given in table 8.6. The activation energies for various products show interesting trends. The activation energy for various products decreases in the following order. $\text{CH}_4 > \text{C}^2 \text{ oxyg} \approx \text{CO}_2 > \text{total oxyg} > \text{C}^1 \text{oxyg}$. Thus these differences in activation causes changes in the products distribution. Hence the reaction temperature plays an important role in deciding the selectivity of these catalysts. For example, because the activation energy for oxygenates is much lower than the activation energy for hydrocarbons, higher selectivities to oxygenates can be obtained by using lower temperature. Of course, the catalyst should be sufficiently active to be useful at

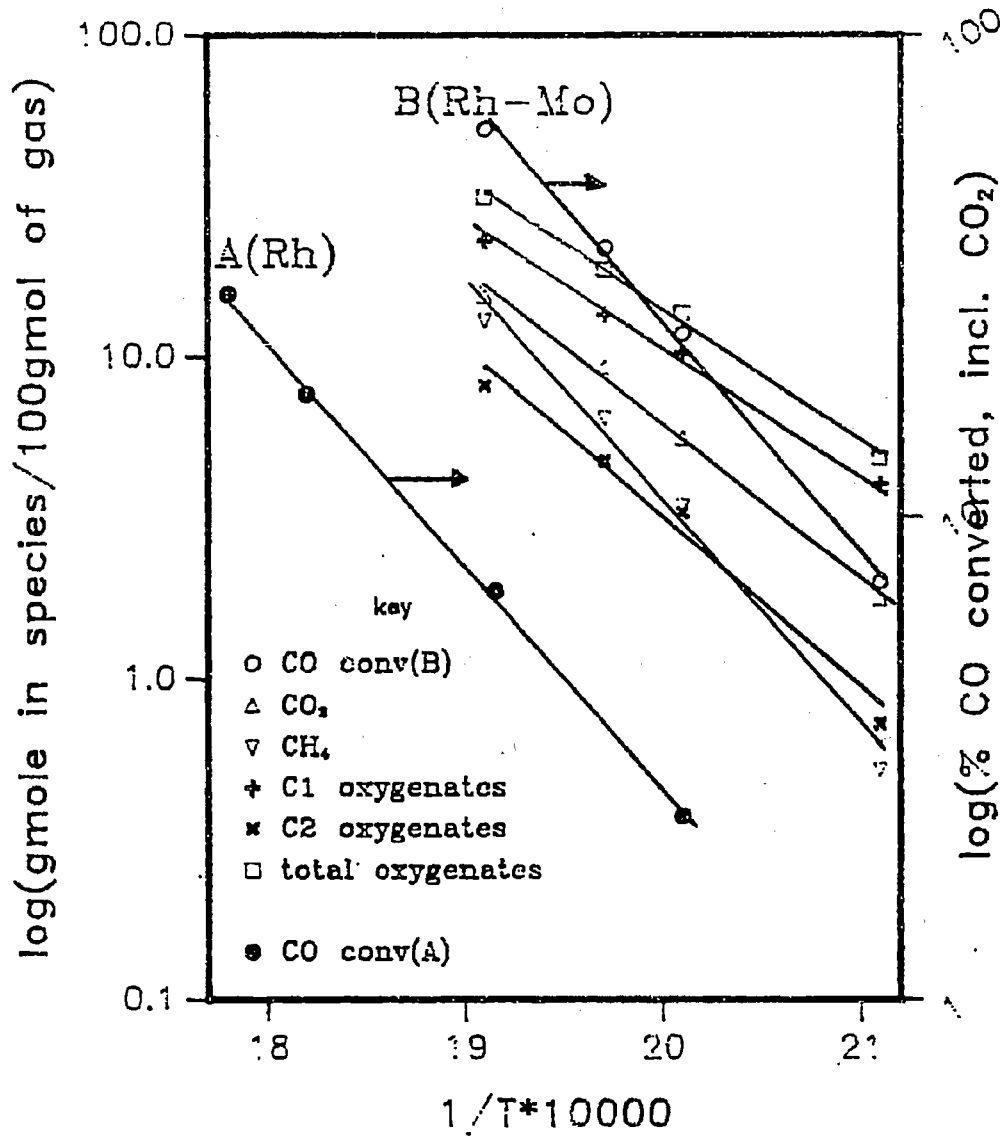


Figure 8.10: Log of overall rate versus inverse temperature for 3%Rh 7.5%Mo /Al₂O₃ catalysts at 30atm and hydrogen/CO=2.

lower temperatures. The data in figure 8.10 was fitted to straight lines and their intercepts evaluated. These intercepts are listed in table 8.6.

Since the y-axis in figure 8.10 is not the rate constant, the intercepts are the pre-exponential factors multiplied by an arbitrary constant b. This constant b takes into account the proportionality between the rate and the conversion for differential conditions and the proportionality constant between the rate of a species and rate constant of the reaction.

A simple predictive calculation is summarized in table 8.7 shows how new and more active catalyst could lead to higher oxygenate selectivity. For example if a catalyst were to be sufficiently active at 140C, the selectivity to oxygenates would be 98.5%. The calculated selectivities were computed using an activation energy for methane of 32.4 Kcal/gmol and activation energy for oxygenates of 18.6 Kcal/gmol. This data shows that differences in the activation energies could be effectively used for selectivity control in CO hydrogenation reactions. Thus the activation energies points us towards the direction in which further improvements can be achieved.

Table 8.7: Use of activation energies for selectivity control

Temp(C)	% Selectivity Calculated	% Selectivity Observed
250	65	65
225	78	73
220	88	86
180	94	
160	97	
140	98.5	

Table 8.6: Activation energies

Catalysts	Species	$\ln(A \cdot b)$	E_{act} Kcal/gmol
3%Rh/Al ₂ O ₃	CO	22.5±0.1	21.3±0.3
3%Rh 7.5%Mo/Al ₂ O ₃	CO	25.0±0.1	21.6±0.9
	CO ₂	23.9±0.1	21.9±0.7
	CH ₄	33.9±0.2	32.4±2.6
	C1 oxygenates	19.7±0.5	17.2±0.7
	C2 oxygenates	25.6±0.2	24.3±2.4
	total oxygenates	21.3±0.1	18.6±0.9

b - arbitrary constant

8.7 Ethylene Hydrogenation

The IR results in chapter 9 indicate that there is no weakening of CO bond on addition of Mo to Rh/Al₂O₃ catalysts. Thus there is no evidence that addition of Mo affects the activation of carbon monoxide. Hence the activation of hydrogen is investigated. Ethylene hydrogenation was chosen as a test reaction because of its simplicity. To simulate the gas phase environment at reaction conditions ethylene hydrogenation was run in the presence and absence of gas phase CO.

Ethylene hydrogenation was run at room temperature and at 9750hr⁻¹ GHSV. The catalysts was reduced under hydrogen under the same temperature-time schedule as in the CO hydrogenation runs. The gas feed for ethylene hydrogenation consisted of 30% hydrogen, 3% ethylene and the rest helium. The reactant feed is deliberately lean in ethylene to prevent poisoning of the catalysts

by coke formation on the surface[11]. The reaction was run at atmospheric pressure.

Ethylene hydrogenation was first run on calcined Al_2O_3 . $\text{Mo}/\text{Al}_2\text{O}_3$. $\text{Rh}/\text{Al}_2\text{O}_3$ and $\text{Rh-Mo}/\text{Al}_2\text{O}_3$. None of the catalysts are active for ethylene hydrogenation at room temperature in calcined state. However, in the reduced state the catalysts behave differently. It is well known that transition metals are active for ethylene hydrogenation[11]. Presence of carbon monoxide in the gas phase can have a profound effect on ethylene hydrogenation activity. $\text{Rh}/\text{Al}_2\text{O}_3$ is reported to be a good ethylene hydrogenation catalyst; this is also seen in our results i.e. ethylene undergoes complete conversion. However in presence of carbon monoxide there is no conversion of ethylene. Carbon monoxide in gas phase acts as an ON/OFF switch for conversion of ethylene at 30C. There is no activity for ethylene hydrogenation owing to Al_2O_3 at 30C. $\text{Rh-Mo}/\text{Al}_2\text{O}_3$ acts like $\text{Rh}/\text{Al}_2\text{O}_3$ in the absence of carbon monoxide and like $\text{Mo}/\text{Al}_2\text{O}_3$ in the presence of carbon monoxide. A summary of results is given in table 8.8.

$\text{Mo}/\text{Al}_2\text{O}_3$ catalysts has some activity for ethylene hydrogenation in partially reduced state. This activity is orders of magnitude less than the ethylene hydrogenation activity of reduced $\text{Rh}/\text{Al}_2\text{O}_3$. $\text{Rh-Mo}/\text{Al}_2\text{O}_3$ is an active for ethylene hydrogenation at room temperature in the absence of gas phase CO. There is complete ethylene conversion to ethane under the conditions specified in table 8.8. $\text{Mo}/\text{Al}_2\text{O}_3$ unlike $\text{Rh}/\text{Al}_2\text{O}_3$. has some residual hydrogenation activity for ethylene hydrogenation in the presence of gas phase CO. This is because molybdenum exists in partially reduced form and hence is not completely inhibited by gas phase CO. In comparison, $\text{Rh-Mo}/\text{Al}_2\text{O}_3$ behaves like $\text{Mo}/\text{Al}_2\text{O}_3$ catalysts in the presence of CO. Thus for ethylene hydrogenation $\text{Rh-Mo}/\text{Al}_2\text{O}_3$ behaves like $\text{Rh}/\text{Al}_2\text{O}_3$ in the absence of gas phase CO and behaves like $\text{Mo}/\text{Al}_2\text{O}_3$ in the presence of gas phase CO.

Table 8.8: Summary of ethylene hydrogenation results

Catalysts(reduced)	pCO(atm)	Ethylene conversion %
3%Rh/Al ₂ O ₃	0.00	>99.99%
	0.08	<0.01%
7.5%Mo/Al ₂ O ₃	0.00	≈40.0%
	0.08	≈5.30*%
3%Rh7.5%Mo/Al ₂ O ₃	0.00	>99.99%
	0.08	≈5.50*%

* - deactivated in 4 hours

8.8 Conclusions

In this section, the reactivity of molybdena modified rhodium alumina catalysts for CO hydrogenation is discussed. Addition of molybdena to Rh/Al₂O₃ catalysts was found to increase rates of CO hydrogenation from 10 to 100-fold. The Mo/Al₂O₃ catalysts were inactive in the same process parameter space. Thus, the addition of molybdena to Rh/Al₂O₃ is truly a synergistic effect. The selectivity to oxygenates is also found to increase on molybdena addition. There are subtle yet important differences in the product distribution. The observed absence of aldehydes, acids and esters on the Mo-Rh/Al₂O₃ catalysts indicate the higher hydrogenation activity of these catalysts. Also, the large amounts of ethers formed is a manifestation of the higher acidity of these catalysts. The water gas shift reaction is accelerated and this leads to large amounts of carbon dioxide formed. Because of the fast water gas shift reaction very small amounts of water is formed. Delplot analysis of the products formed suggests that all products except ethane, ethanol and methyl ethyl ether (sometimes) are primary products. Delplot analysis also indicates that carbon dioxide is a primary product, which implies that the water gas shift reaction is a fast process. A power law fit for the overall rate shows that the rate of carbon monoxide hydrogenation on the molybdena modified rhodium/alumina catalysts is less inhibited by gas phase carbon monoxide than for the rhodium/alumina catalysts. This again reflects the higher hydrogenation activity of these modified catalysts, and less inhibition by carbon monoxide. The activation energies for the overall rate of consumption of CO is same. The activation energy for formation of various products vary as

$$C^1H_4 > C^2 \text{ oxyg} \approx C^1O_2 > \text{total oxyg} > C^1 \text{ oxyg}$$

This differences in activation energies leads to the changes in selectivity with temperature.

The ethylene hydrogenation results clearly showed that the hydrogenation activity of Rh-Mo/Al₂O₃ in the absence of CO in the gas phase stems from the rhodium component and the hydrogenation activity of Rh-Mo/Al₂O₃ in the presence of CO stems from the partially reduced molybdena component.

REFERENCES

1. P.C. Ellgen and M.M. Bhasin U.S. Patent 4,096,164; June 20, 1978; assigned to Union Carbide Corporation.
2. Y.Y. Huang, U.S. Patent 4,328,129; May 4, 1982; assigned to Ethyl Corporation.
3. S.J. Jackson, UK Patent Appl. 2,151,616A; July 24, 1985; assigned to Imperial Chemical Industries.
4. S.D. Jackson, B.J. Brandreth and D. Winstanley, Appl. Catal. 1986, 27, 325.
5. H.C. Foley and M.P. O'Toole, U.S. Patent 4,684,618; August 4, 1987; assigned to American Cyanamid.
6. H.C. Foley and M.P. O'Toole, U.S. Patent 4,687,784; August 18, 1987; assigned to American Cyanamid.
7. B.J. Kip, Ph.D. thesis. Eindhoven University of Technology, The Netherlands, 1987.
8. B. Walther, M. Scheer, H.G. Buttcher, A. Trunschke, H. Ewald, D. Gutschick, H. Miessner, M. Skupin and G. Vorbeck, accepted. Inorg. Chem. Acta.
9. F.G.A. Van Den Berg, Ph.D. Thesis. University of Leiden, 1983. The Netherlands.
10. R.P. Underwood and A.T. Bell. Appl. Catal. 1986, 21, 157.
11. G.C. Bond. "Catalysis by Metals". Academic Press, 1962. New York.

CHAPTER 9

CHARACTERIZATION OF MOLYBDENA MODIFIED RHODIUM/ALUMINA CATALYSTS

As shown in chapter 8, the incorporation of large amounts of Mo in Rh Al_2O_3 catalyst leads to greatly enhanced CO hydrogenation activity. The selectivity to oxygenates is increased significantly and the water gas shift reaction is also accelerated. The work done in this chapter was aimed at elucidating the structure of these catalysts to probe the reason for their enhanced activity.

This chapter deals with characterization of physical and chemical state of Mo and Rh in Rh-Mo/ Al_2O_3 using a battery of spectroscopic techniques. Specifically, issues such as changes in oxidation state of Mo and Rh, changes in dispersion of molybdena and rhodium, changes in bonding of CO on addition of molybdena and the spatial distribution of species on the surface are addressed.

Each section discusses the results of the individual characterization technique. The discussions section combines the results of all the techniques and discusses the relevance of the results for explaining the higher activity obtained on molybdena addition.

9.1 X-Ray Fluorescence Spectroscopy

Even though a no-excess solution impregnation method is used for catalysts preparation, the Mo and Rh loading in the series of catalysts was measured using

x-ray fluorescence spectroscopy. The selection of calibration standards and other details are given in chapter 4.

The Rh loading was lower than expected. However the relative Rh loading was within 10% error. The difference in the Mo loading between 3%Rh x%Mo/Al₂O₃ and x%Mo/Al₂O₃ was again within 10%. The results are summarized in table 9.1.

Table 9.1: Elemental ratio in Rh-Mo/Al₂O₃ and Mo/Al₂O₃ catalysts measured by x-ray fluorescence spectroscopy

Catalyst	Rh ratio	Mo ratio
3%RhAl ₂ O ₃	1.00	
3%Rh2.8%Mo/Al ₂ O ₃	1.05	1.00
3%Rh2.8%Mo/Al ₂ O ₃ (+)	1.90	1.33
7.5%Mo/Al ₂ O ₃		3.10
3%Rh7.5%Mo/Al ₂ O ₃	1.25	2.72
15%Mo/Al ₂ O ₃		5.61
3%Rh15%Mo/Al ₂ O ₃	1.23	5.27

(+) Prepared from carbonyl clusters by Prof. Henry C. Foley

9.2 CO Chemisorption

CO chemisorption was done to measure the dispersion of rhodium. Normally, dispersion is measured with hydrogen chemisorption or x-ray line broadening or TEM. In the case of Rh-Mo/Al₂O₃ molybdenum is expected to be in a partially reduced molybdena. This will be shown later. This partially reduced molybdena forms non-stoichiometric compounds with hydrogen known as molybdenum

bronzes. Hence hydrogen chemisorption cannot be used to measure rhodium dispersion in Rh-Mo- Al_2O_3 catalysts. In contrast, as will be shown in the section on IR, carbon monoxide does not adsorb on partially reduced molybdena. However, CO can adsorb in many forms such as linear, gem-dicarbonyl and bridged, hence the stoichiometry of adsorption can change. But CO chemisorption gives trends in dispersion. Furthermore, IR can be used in conjunction with CO chemisorption studies to find the stoichiometry of CO adsorption.

CO adsorption was done in a flow apparatus described in detail in chapter 3. The reduction was carried out in stages similar to the reduction procedure used in reaction studies. Figure 9.1 shows the amount of CO chemisorbed in microgram of CO/ gm of catalysts versus the amount of molybdena added to rhodium/alumina. The point on the y-axis is for 3%Rh 0%Mo/ Al_2O_3 . Hydrogen chemisorption on 3%Rh/ Al_2O_3 is used to find the dispersion of rhodium, which is 60%. The hydrogen chemisorption was done in a static mode. The amount of CO chemisorbed decreases monotonously with the amount of molybdena added to rhodium/alumina. The decrease in CO chemisorption is substantial, e.g., the CO chemisorption for 3%Rh 15%Mo/ Al_2O_3 is 20-25% of the CO chemisorption of 3%Rh/ Al_2O_3 .

Also, on the same plot, the overall rate of carbon monoxide consumption based on each rhodium atom present in the sample at 225C is plotted. This is also called as turnover frequency based on the total number of rhodium atoms. This turnover frequency increases with the amount of molybdena added. Thus even though the number of CO adsorption sites decrease, the rate of CO consumption increases. Furthermore, more drastic results are obtained if the comparison is done on the turnover frequency based on each CO adsorption site (assuming a stoichiometric coefficient of 1). CO chemisorption was $112\mu\text{moles/gm}$ for Rh/ Al_2O_3 and $28\mu\text{moles/gm}$ for 3%Rh 15%Mo/ Al_2O_3 . However the overall activity increased 37.5-fold. Thus the overall activity per CO site was increased by 150-fold. In any

case there is a 10-100 fold increase in the rate of CO hydrogenation on molybdena addition.

Three factors could account for the decrease in CO chemisorption.

- 1: an increase in the particle size of rhodium, caused by the addition of molybdena.
- 2: a fraction of rhodium may be in an oxidic form which cannot adsorb CO and this fraction may increase with amount of molybdena added.
- 3: Molybdena cover or blocks part of rhodium surface and reduces the amount of carbon monoxide adsorbed by simply blocking adsorption sites.

The next section on x-ray diffraction studies will rule out 1. X-ray photoelectron spectroscopy and IR will rule out 2.

9.3 X-Ray Diffraction

In this section, the different phases and their particle sizes are investigated in Rh-Mo/Al₂O₃ catalysts. XRD was done on fresh calcined, used and passivated catalysts. The powder diffractometer and the experimental set-up used is described in chapter 3. First XRD patterns were collected for calcined Rh-Mo/Al₂O₃ with different loading of molybdenum. None of the catalysts showed diffraction patterns corresponding to Rh metal and Rh₂O₃. A mixed oxide of rhodium and molybdena is reported [1]. However the samples which included calcined, passivated and used 3% Rh 2.8% Mo/Al₂O₃, 3% Rh 7.5% Mo/Al₂O₃ and 3% Rh 15% Mo/Al₂O₃ catalyst did not show any presence of the mixed oxide of rhodium oxide and molybdena [1] with up to 200sec data collection time for each increment of 0.02 degree in two-theta. This mixed oxide is expected only in the calcined catalysts, since both the rhodium phase and the molybdenum phase in the calcined catalysts are in oxide form. The absence of XRD patterns of Rh and rhodium oxide indicate that the

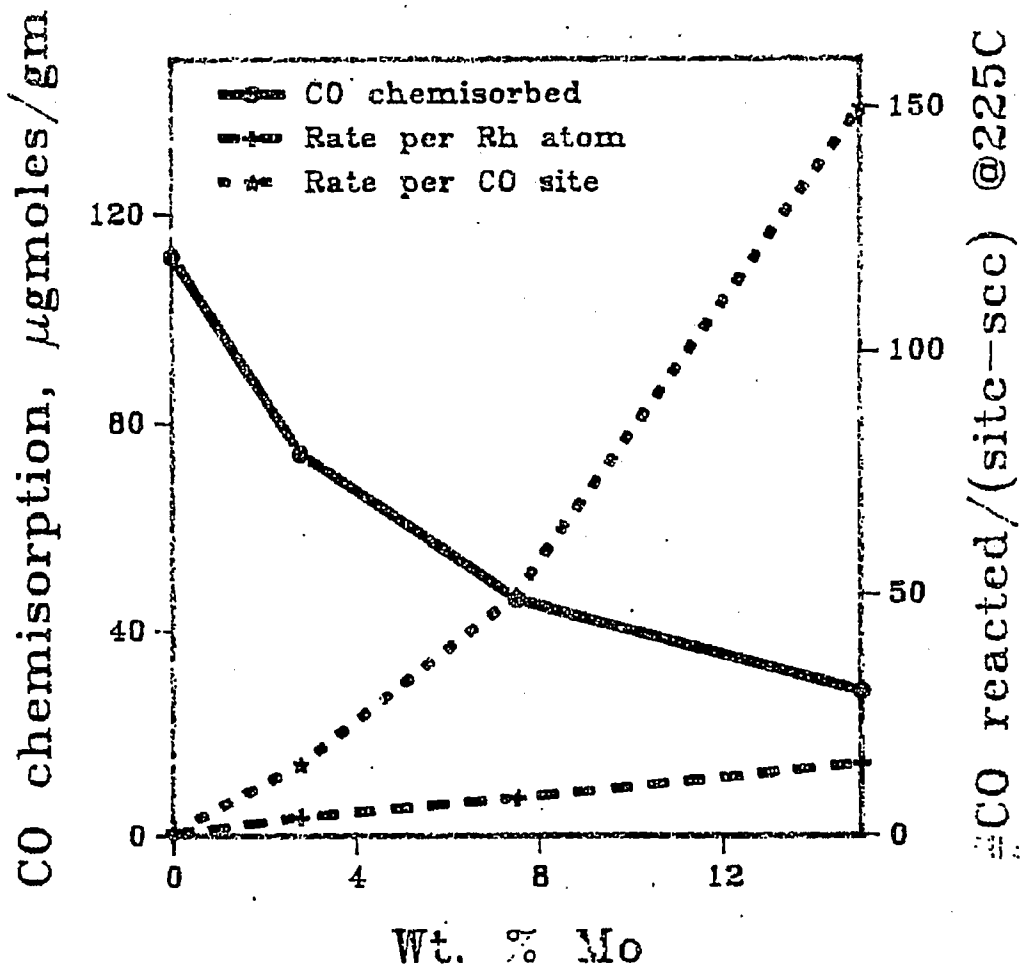


Figure 9.1: Effect of molybdena addition on (A) CO chemisorption. (B) overall rate of CO consumption at 225C, 30atm, 3000GHSV based on each rhodium atom in the catalysts (C) overall rate of CO consumption at 225C, 30atm, 3000GHSV based on each CO adsorption site.

REPRODUCED FROM BEST
AVAILABLE COPY

particle size of rhodium is less than 30 Å. Thus the scheme 2 outlined in the previous section to account for the decrease in CO chemisorption cannot explain the XRD data.

There is no detectable pattern of any molybdenum oxide in any of the Mo/Al₂O₃ and Rh-Mo/Al₂O₃ catalysts after various treatments. Also all catalysts except 15% Mo/Al₂O₃ do not show any detectable pattern of aluminum molybdate. A weak and broad pattern corresponding to Al₂(MoO₄)₃ is detected for 15% Mo/Al₂O₃ catalysts. It is interesting to note that no Al₂(MoO₄)₃ diffraction pattern is not observed with 3%Rh 15%Mo/Al₂O₃ catalysts. Thus the presence of rhodium prevents the formation of aluminum molybdate.

Figure 9.2 shows the x-ray diffraction pattern for used 3%Rh 2.8%Mo/Al₂O₃ catalysts. The results from this diffraction pattern is tabulated in table 9.2. The sharp peaks C, E and H have an intensity ratio of C:E:H = 100:90:50 and these peaks correspond to aluminum metal from the sample holder. The rest of the broad and diffuse peaks arise from the support[2]. As noted earlier, there is no detectable x-ray diffraction pattern of rhodium metal, rhodium oxide, molybdena and MoRh₂O₆ in of the catalysts samples investigated.

Figure 9.3 shows the x-ray diffraction pattern of (A) 3%Rh 2.8%Mo/Al₂O₃, (B) 3%Rh 7.5%Mo/Al₂O₃ and (C) 3%Rh 15%Mo/Al₂O₃ catalysts. From the figure it is clear that the XRD pattern of the three catalysts is same and there are no additional features in any one of them. However, as shown in figure 9.4 (A), the diffraction pattern of 15%Mo Al₂O₃ shows a broad diffraction pattern corresponding to Al₂(MoO₄)₃. For comparison, same regions of the diffraction pattern of 3%Rh 15%Mo Al₂O₃ and 7.5%Mo Al₂O₃ are also shown. The aluminum molybdate is formed and detected only at high loading of molybdenum. XRD pattern of 7.5%Mo Al₂O₃ collected for long times (> 4 times the data collection time for 15%Mo Al₂O₃) did not show any detectable pattern of aluminum molybdate.

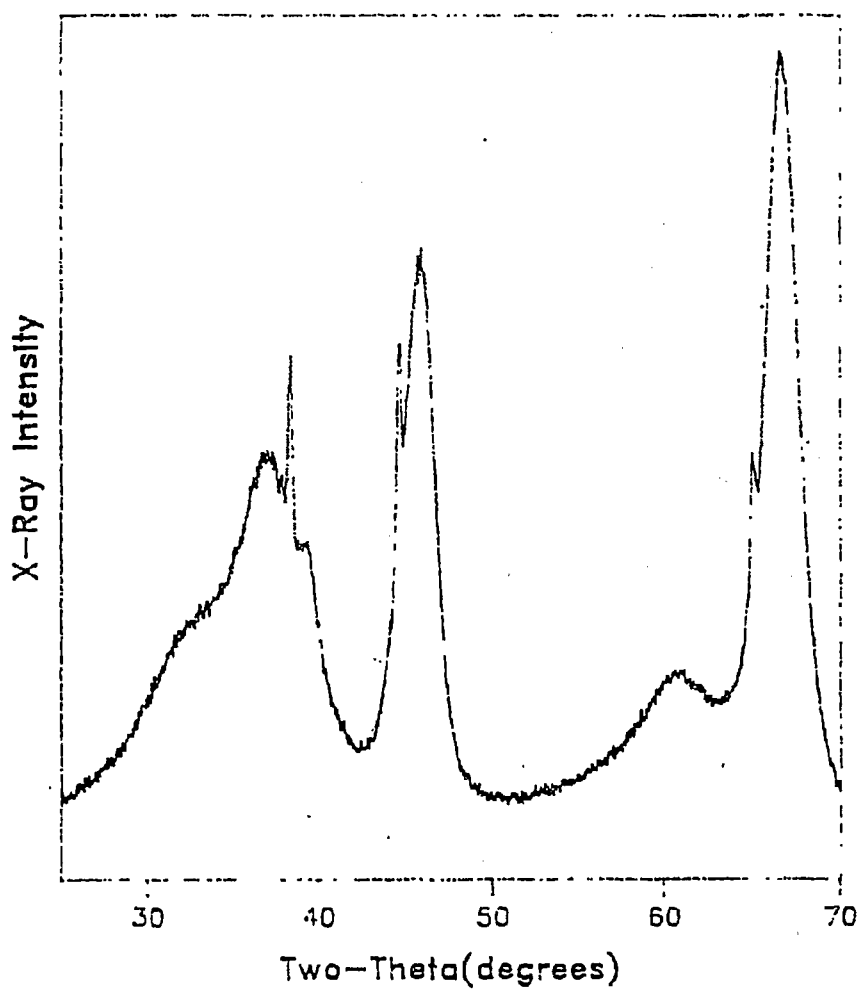


Figure 9.2: X-Ray diffraction pattern of used 3%Rh 2.8%Mo Al₂O₃ catalysts

REPRODUCED FROM BEST
AVAILABLE COPY

Table 9.2: Analysis of peaks in the x-ray diffraction pattern of used 3%Rh
2.8%Mo/Al₂O₃ catalysts

Peak	2 θ , deg.	d(\AA)	Comments
A	33.65	2.663	diffuse-overlapped
B	37.13	2.421	diffuse-overlapped
C	38.37	2.345	sharp
D	39.27	2.294	shoulder peak
E	44.55	2.033	diffuse-intense
F	45.78	1.9819	sharp
G	60.89	1.5213	diffuse
H	65.06	1.4335	sharp shoulder
I	66.03	1.4335	diffuse-intense

Hence the absence of aluminum molybdate in 7.5%Mo/Al₂O₃ is not due to detection limits. To check the presence of aluminum molybdate, it was synthesized by air calcining a stoichiometric mixture of aluminum nitrate and ammonium molybdate at 700C. Figure 9.5 shows the XRD pattern of aluminum nitrate, ammonium molybdate and aluminum molybdate. Note the absence of aluminum nitrate and ammonium molybdate in the synthesized aluminum molybdate.

Also, for comparison, the synthesized aluminum molybdate and 15%Mo/Al₂O₃ catalysts are shown in figure 9.6. A silicon standard was used to find the instrument line broadening. The procedure for calculating average particle size is given elsewhere³. The average aluminum molybdate particle size measured with x-ray line broadening is 90Å.

9.4 Transmission Electron Microscopy and Energy Dispersive X-Ray Analysis

In the previous section, the absence of any crystallite above 30Å was ruled out based on evidence from XRD studies. In this section, TEM/EDX results are reported, which corroborate the XRD evidence. Some more evidence will be shown to rule out scheme 1 outline in section 1 of this chapter.

9.4.1 Bright Field Images

There are no visible particles in the bright field image of calcined and used 3%Rh Al₂O₃, used 3%Rh 7.5%Mo, Al₂O₃ and calcined 3%Rh 15%Mo/Al₂O₃. To check the instrument, particles of size $\approx 150\text{\AA}$ were detected on the catalysts after agglomeration due to oxidation/reduction treatment outlined in chapters 6 and 7. The contrast between the particle and other components in the catalysts is very low. This low contrast arises due to many reasons. First and foremost, the alumina consists of semi-crystalline microcrystallites. These randomly oriented

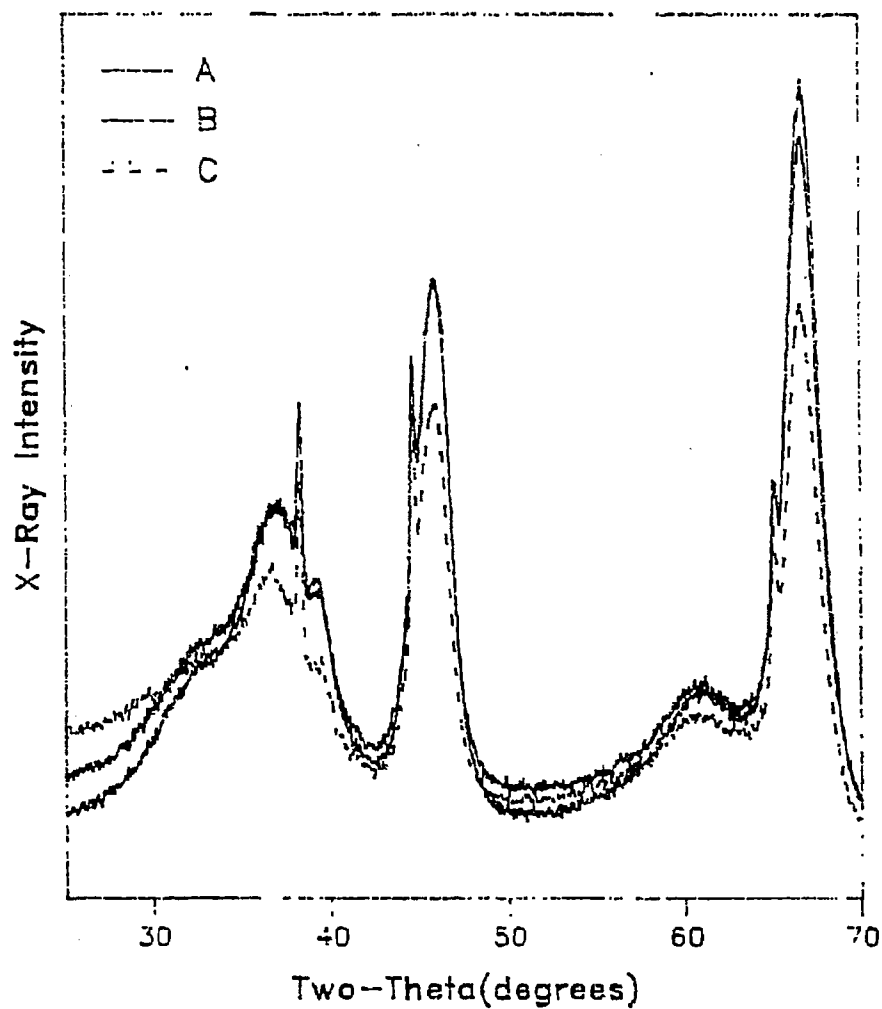


Figure 9.3: X-Ray diffraction pattern of fresh (A) 3%Rh 2.8%Mo, Al₂O₃ (B) 3%Rh 7.5% Mo a and (C) 3%Rh 15%Mo, Al₂O₃ catalysts

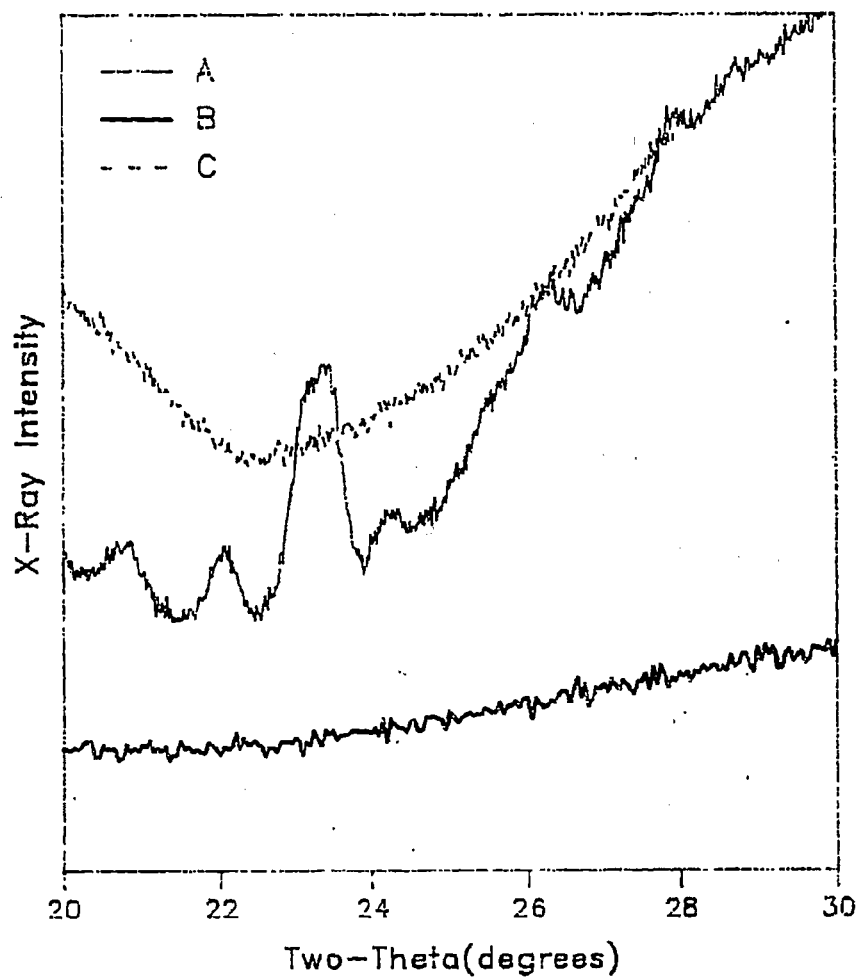


Figure 9.4: X-Ray diffraction pattern of fresh (A) 15%Mo, Al₂O₃ . (B) 3%Rh 15%Mo, Al₂O₃ and (C) 7.5% Mo, Al₂O₃ catalysts

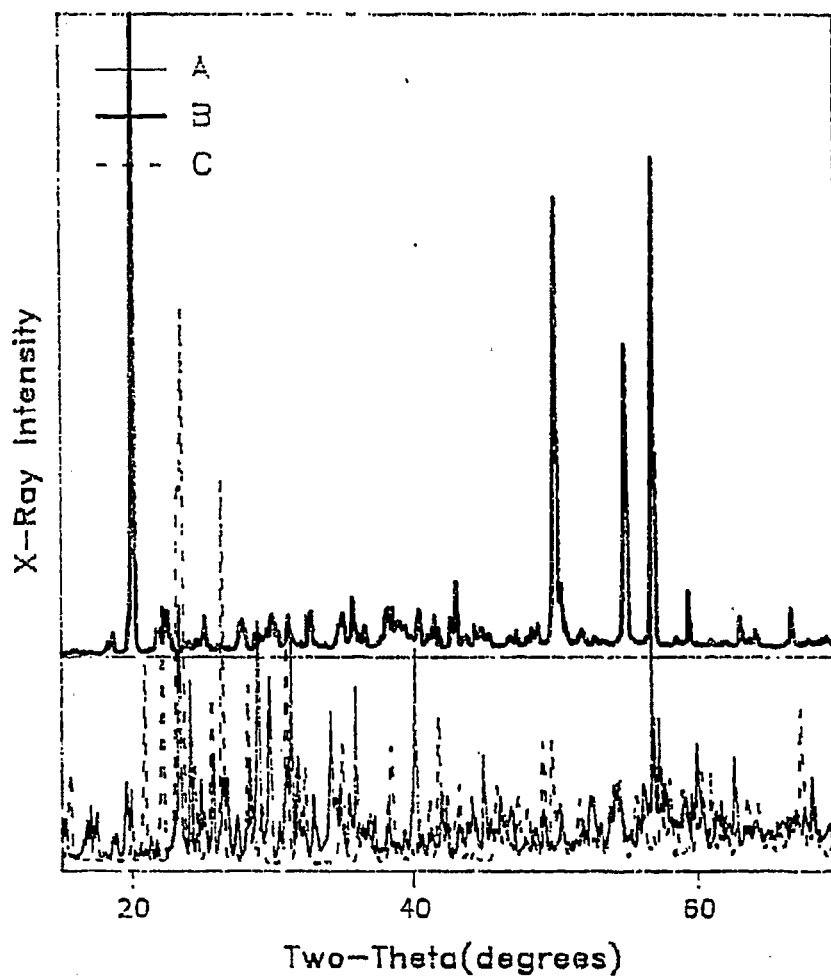


Figure 9.5: X-Ray diffraction pattern of (A) ammonium molybdate (B) aluminum nitrate and (C) synthesized aluminum molybdate

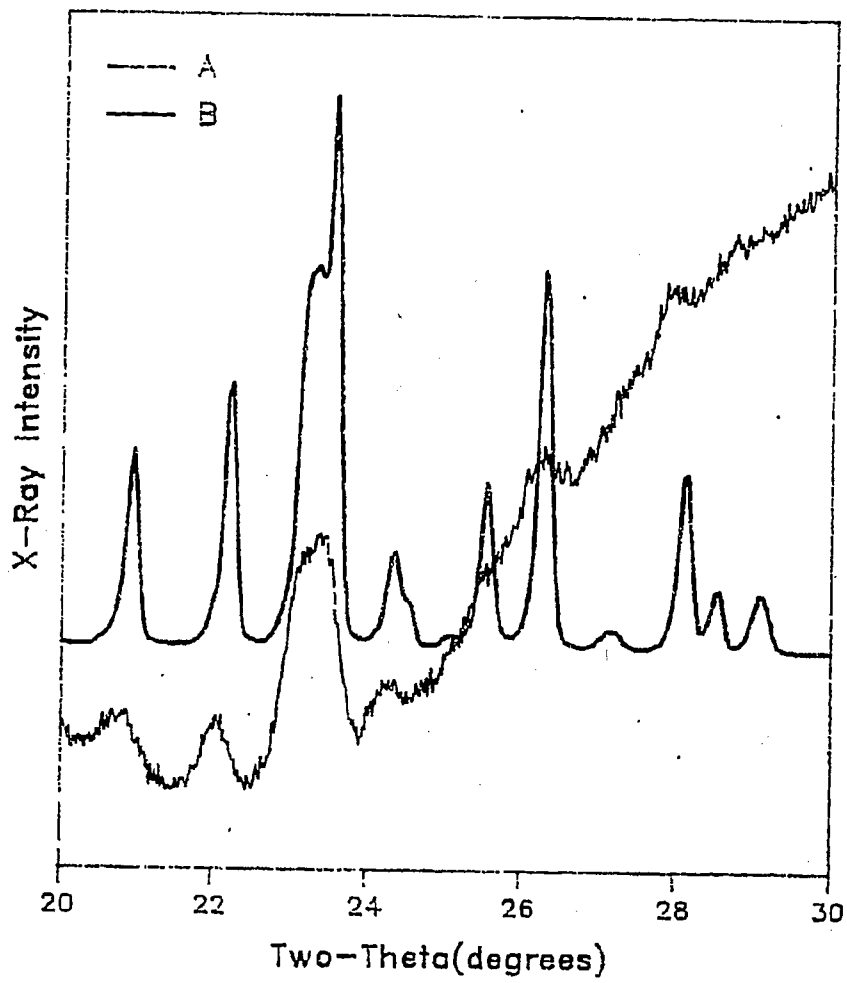


Figure 9.6: X-Ray diffraction pattern of (A) fresh 15%Mo, Al₂O₃ catalysts and (B) synthesized aluminum molybdate

microcrystallites diffract the electron beam in different direction, causing the contrast to decrease. Furthermore, the alumina used is a porous alumina, hence in a typical electron microscope sample ($10000 - 100000 \text{ \AA}$), there are 200-2000 alumina-vacuum interfaces. These interfaces cause large amount of scattering of the electron beam. Because of this large scattering and the relatively low Z of Rh and Mo, thus the presence of large particles of rhodium in this sample can be ruled out. Recall that the XRD of this sample did not show any detectable diffraction pattern of rhodium or rhodium oxide.

The bright field images of used 3%Rh 15%Mo/ Al_2O_3 also do not show any detectable contrast between any particles and support, thus confirming the presence of small particles of rhodium. The highest obtainable magnification on the electron microscope used was 400kX. With a 2.5 magnification while developing and printing gives an effective magnification of 1000kX. On this scale a 1mm particle corresponds to 10 \AA . Thus the absence of particles in the image is due to poor contrast. This is consistent with hydrogen chemisorption on Rh/ Al_2O_3 .

9.4.2 Energy Dispersive X-Ray Analysis

The bright field images of 3%Rh/ Al_2O_3 , used 3%Rh 7.5% Mo/ Al_2O_3 and calcined 3%Rh 15%Mo/ Al_2O_3 discussed earlier do not show any presence of particles. To make sure that there is rhodium and molybdenum in the area of the bright field image, a subsequent energy dispersive x-ray spectrum is taken. The EDX results show the presence of Rh and Mo in the region from which images are taken for Rh-Mo/ Al_2O_3 catalysts.

9.5 In-situ Infrared Spectroscopy

Low pressure in-situ IR spectroscopy was used to investigate the changes in the bonding of CO on addition of Mo to Rh/ Al_2O_3 catalysts. As discussed in chap-

ter 2, the predominant adsorbed species seen in an infrared spectra on Rh/Al₂O₃ are the gem-dicarbonyl, the linear and the bridged species. The amounts of these species depend on the gas phase environment. This was illustrated in chapter 7. Table 9.3 on page 330 shows the different species observed and their observed frequencies. For example, the gem-dicarbonyl species is atomically dispersed and has an oxidation state of 1, and the gem-dicarbonyl species is affected by the presence of molybdenum. The details of these shift will be discussed later. In contrast, the linear and the bridged species which are observed on metal crystallite and are associated with rhodium of oxidation state zero, do not shift on molybdena addition. Thus there is no detectable change in the vibrational frequency or the bonding of CO in the linear and the bridged species.

The gem-dicarbonyl shifts to higher wave numbers and the shift is compared in table 9.4. These results agree with the recently reported results of Hecker et al. [4] on Rh-Mo/SiO₂. The vibrational spectra of a gem-dicarbonyl species has two relevant stretching force constants, if the coupling between metal vibrations and the adsorbate stretches and also the coupling between the adsorbate stretching and adsorbate bending force fields is neglected [5]. The F & G matrix theory, details of which are given elsewhere [6] is used to find the C-O stretching force constant $k(\text{CO})$ and the coupling constant between the two CO ligands on the gem-dicarbonyl species. Thus the CO bond is strengthened on molybdena addition however this shift is small compared to observed shifts. Furthermore as shown in chapters 2 and 7, the gem-dicarbonyl species are formed under oxidizing gas phase environments and are also shown by other investigators to be of no significance to the catalytic activity.

The IR results of fresh and used molybdena modified Rh/Al₂O₃ catalysts are compared in table 9.5. The linear and bridged species are much more stable on the used catalysts as compared to the fresh catalysts. However at 150°C, all the species are converted to the gem-dicarbonyl species. This higher stability

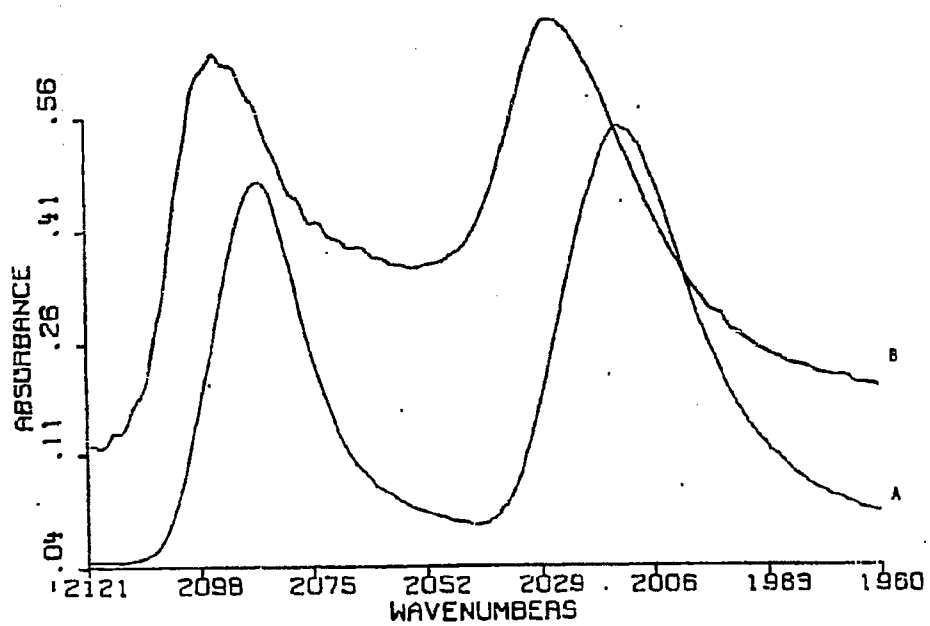


Figure 9.7: Infrared spectra of CO adsorbed as gem-dicarbonyl species on (A) $\text{Rh}/\text{Al}_2\text{O}_3$ and (B) $\text{Rh-Mo}/\text{Al}_2\text{O}_3$ catalysts

Table 9.3: Summary of changes in the IR Spectrum of adsorbed CO on molybdena addition

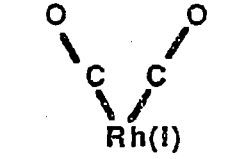
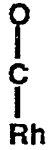
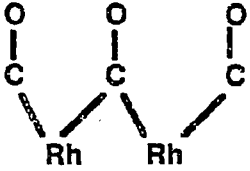
Frequency Range(cm^{-1})	Site distribution	Oxidation state	Structure	Change with Mo
2080-2090 2010-2018	Atomic	1	 <p>Rh(I) g-dicarbonyl</p>	Yes
2042-2076	Crystallite	0	 <p>linear</p>	No
1845-1875	Crystallite	0	 <p>bridged</p>	No

Table 9.4: Results of F & G matrix calculation of the IR results

Catalysts	Experimental Data		Calculation Results	
	antisymmetric	symmetric	k(CO)	k(CO, CO')
	stretch, cm^{-1}	stretch, cm^{-1}	Nm^{-1}	Nm^{-1}
Rh/ Al_2O_3	2012	2084	1694.3	59.6
Rh-Mo/ Al_2O_3	2027	2093	1714.1	54.9

of the linear and bridged carbonyl species on used catalysts is attributed to the deposited carbon on the metal crystallite. This deposited carbon prevents the complete break-up of the metal crystallite by oxidative addition of the surface -OH groups. Also, 7.5%Mo/ Al_2O_3 shows a weak adsorbed species at 2110cm^{-1} at room temperature. This weak band disappears on heating to 100°C . Thus, no CO is adsorbed on Mo/ Al_2O_3 catalysts at temperatures higher than 100°C . These results are in agreement with other investigations[7,8].

9.6 X-Ray Photoelectron Spectroscopy

The next stage in the characterization of Rh-Mo/ Al_2O_3 catalysts is to investigate the chemical state of various elements. Specifically, the oxidation state of Rh and Mo in Rh/ Al_2O_3 , Mo/ Al_2O_3 and Rh-Mo/ Al_2O_3 catalysts after various catalysts treatments and with different Mo loadings is investigated. Also, the physical state of Mo is also investigated. The XPS sampling depth is 10-30Å.

9.6.1 Binding Energies

The binding energies of the different elements referenced to Al(2p) are listed in table 9.6. Rhodium is present in the -3 state after air calcination.

Table 9.5: Effect of various treatments on the IR spectra of fresh 3%Rh/Al₂O₃, fresh 3%Rh 7.5%Mo/Al₂O₃, used 3%Rh 7.5% Mo/Al₂O₃ and 7.5%Mo/Al₂O₃ catalysts

Catal.	3%Rh/Al ₂ O ₃	3%Rh 7.5%Mo/Al ₂ O ₃	7.5%Mo/Al ₂ O ₃	
treat.	fresh	fresh	used	
1	all three species present	g-dicarbonyl(S) linear(W)	linear and bridged only	adsorbed species ≈ 2110 cm ⁻¹
2	only g-dicarbonyl	only g-diarbonyl	g-dicarbonyl(S) linear(W)	above band desorbs
3	linear only	g-diarbonyl(S)	linear g-dicarbonyl	

Key to catalysts treatments:

1. Catalysts reduced, and cooled to room temperature, followed by CO adsorption and outgassing at room temperature
2. Heating the above catalysts to 150C, followed by CO adsorption and outgassing.
3. Cooled the catalysts to 50C, and spectra taken under hydrogen.

but after reduction in hydrogen at 500°C, it is completely converted to metallic state. The oxidation state of Rh is not affected by subsequent treatments such as CO adsorption and reaction. Molybdenum exists in the +6 state after air calcination. The binding energy of Mo(3d_{5/2}) in 3%Rh2.8%Mo/Al₂O₃ is 1 eV higher than that of Mo+6 in MoO₃. This has been explained as a result of the interaction between Mo+6 and the support, where there is donation of electron density from molybdenum to oxygen or the oxygen binding Al and Mo is more electronegative than the oxygen in the bulk MoO₃. On reduction in hydrogen at 500°C molybdenum is reduced from the +6 state to a mixture of +6, +5 and to +4 states given in figures 9.8 and 9.9. However, substantial amount of molybdenum exists in +5 oxidation state.

This confirms with the data obtained from ESR experiments, which will be discussed later. The binding energy and the shape of the Mo peak do not change on subsequent CO adsorption and reaction. The reduction of Mo is increased with increase in Mo loading. Surprisingly, the extent of reduction of Mo is not affected by the presence of Rh, see figures 9.8 and 9.9. In contrast, with Ni and Mo the reduction of Mo is enhanced by presence of Ni. These results are consistent with previous investigations [9-12].

9.6.2 Relative Photoelectronic Response

Figure 9.10 shows the relative photoelectronic response of Mo (defined as Intensity of Mo peak/Intensity of Al) for Rh-Mo/Al₂O₃ and Mo/Al₂O₃. The variation of the relative photoelectronic response for each series of catalysts, i.e., Mo/Al₂O₃ and Rh-Mo/Al₂O₃ is linear with respect to Mo loading. This implies that the state of aggregation of molybdena is same in each series of catalysts at different Mo loading. However, the Mo(3d) photoelectronic response is higher on Mo/Al₂O₃ than on Rh-Mo/Al₂O₃. Furthermore, the photoelectronic response is not very sensitive to catalysts treatments such as reduction, CO adsorption and

Table 9.6: Binding energies of various elements referenced to Al(2p) peak for Rh/Al₂O₃, Mo/Al₂O₃ and Rh-Mo/Al₂O₃ after different catalysts treatments

Catalysts	Treatment	Rh(3d _{5/2}), eV	Mo(3d _{5/2}), eV
3%Rh/Al ₂ O ₃	air calcined	310.5	
	reduced	307.9	
	CO chemisorbed	308.1	
	reaction	307.8	
3%Rh 2.8%Mo/Al ₂ O ₃	air calcined	310.5	232.7
	reduced	307.6	233.8
3%Rh 2.8%Mo/Al ₂ O ₃ (3Rh28MoC)	air calcined	309.6	233.5
	reduced	307.3	233.0
7.5%Mo/Al ₂ O ₃	air calcined		233.3
	reduced		233.0
3%Rh 7.5%Mo/Al ₂ O ₃	air calcined	310.4	233.5
	reduced	307.4	232.9
	CO chemisorbed	307.7	232.9
15%Mo/Al ₂ O ₃	air calcined		233.5
	reduced		232.5
	CO chemisorbed		232.7
3%Rh 15%Mo/Al ₂ O ₃	air calcined	310.4	233.3
	reduced	307.9	232.7
	CO chemisorbed	307.7	232.6
	reaction	307.5	232.8
Rh foil		307.3	
MoO ₃			233.5
MoO ₂			232.5

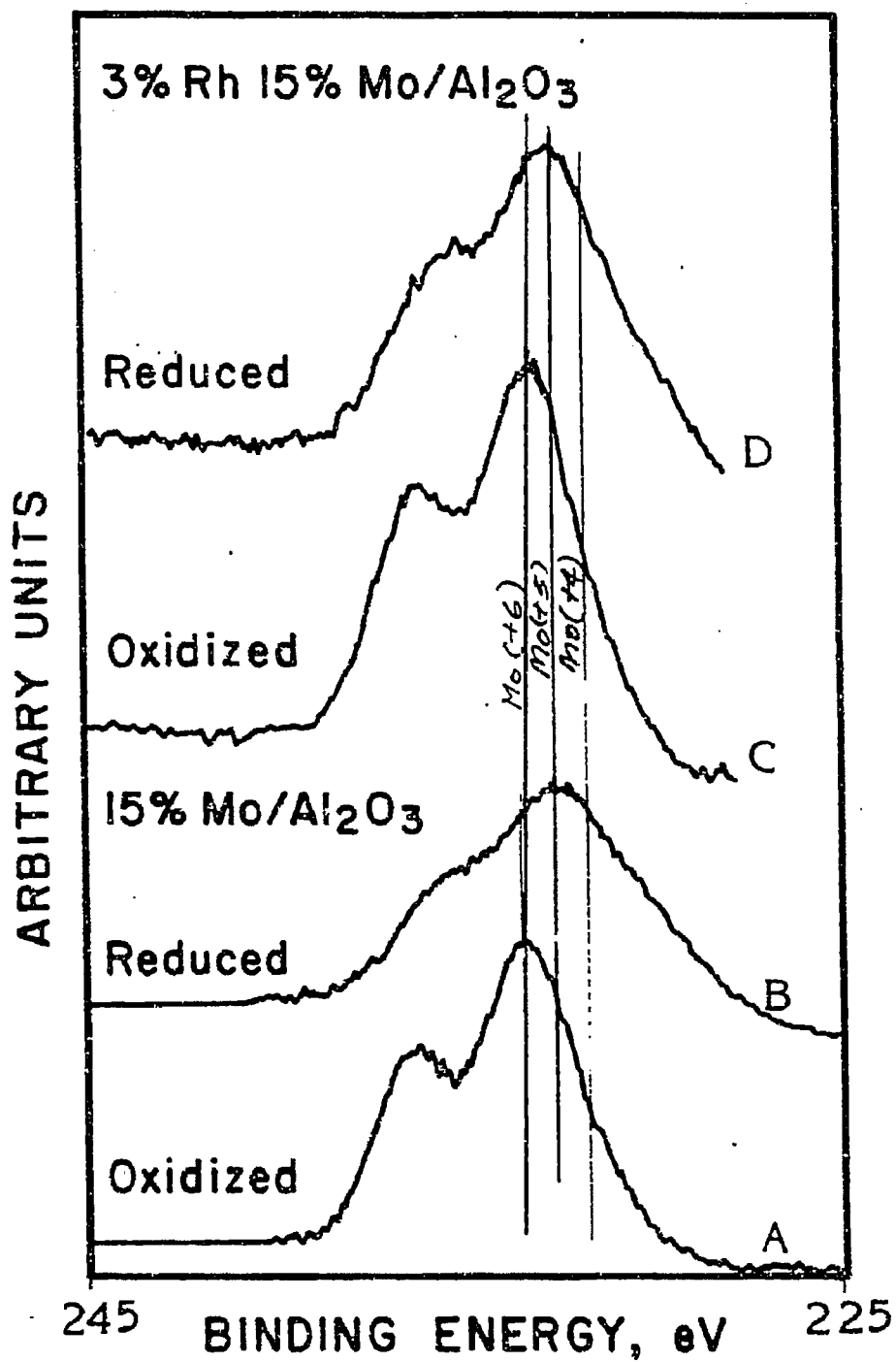


Figure 9.8: X-Ray photoelectron spectra of Mo 3d region of (A) calcined 15% Mo/Al₂O₃, (B) reduced 15% Mo/Al₂O₃, (C) calcined 3% Rh 15% Mo/Al₂O₃ and (D) reduced 3% Rh 15% Mo/Al₂O₃.

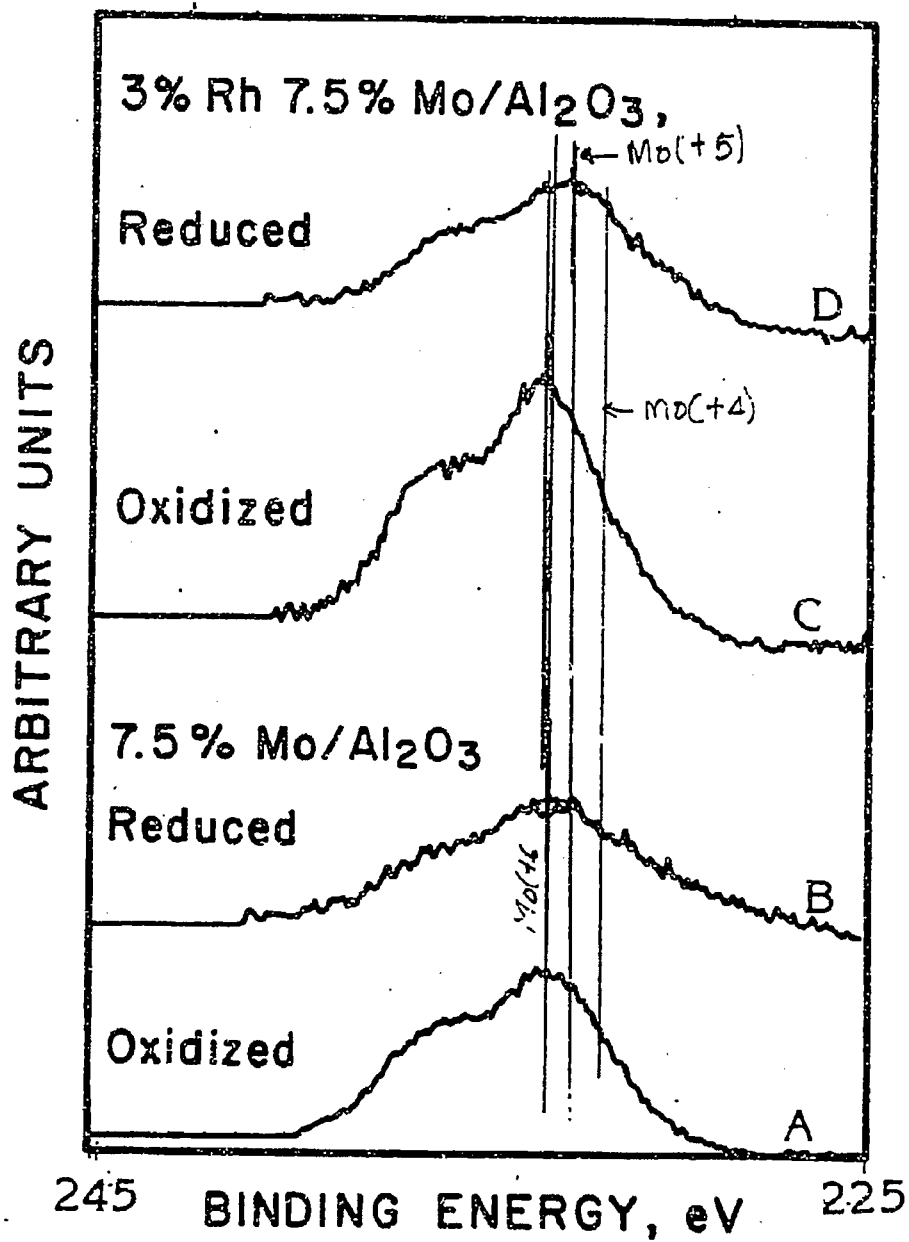


Figure 9.9: X-Ray photoelectron spectra of Mo 3d region of (A) calcined 7.5% Mo Al₂O₃, (B) reduced 7.5% Mo Al₂O₃, (C) calcined 3% Rh 7.5% Mo Al₂O₃ and (D) reduced 3% Rh 7.5% Mo Al₂O₃.

reaction. Thus the state of aggregation of molybdena is not affected by the above treatments. The lower photoelectronic response of Mo in Mo/Al₂O₃ than in Rh-Mo/Al₂O₃ may be due to rhodium blocking molybdenum phase or formation of mixed oxide.

9.6.3 Estimation of Particle Size

Grinding the catalyst does not change the relative photoelectronic response appreciably, hence there is no surface segregation. The absence of surface segregation allows us to use the model of Kerkhof and Moulijn[13] to estimate crystallite size explained in figure 9.11.

According to Kerkhof and Moulijn[13]

$$\frac{I_m}{I_s} = \left(\frac{m}{s}\right) \left(\frac{D(\epsilon_m)}{D(\epsilon_s)}\right) \left(\frac{\sigma_m}{\sigma_s}\right) \left(\frac{\beta_1}{2}\right) \left(\frac{1 - e^{-\beta_2}}{1 - e^{-\beta_1}}\right) \left(\frac{1 - e^{-\alpha_1}}{\alpha_1}\right) \quad (9.1)$$

where

I_m = Intensity of modifier peak

I_s = Intensity of support peak

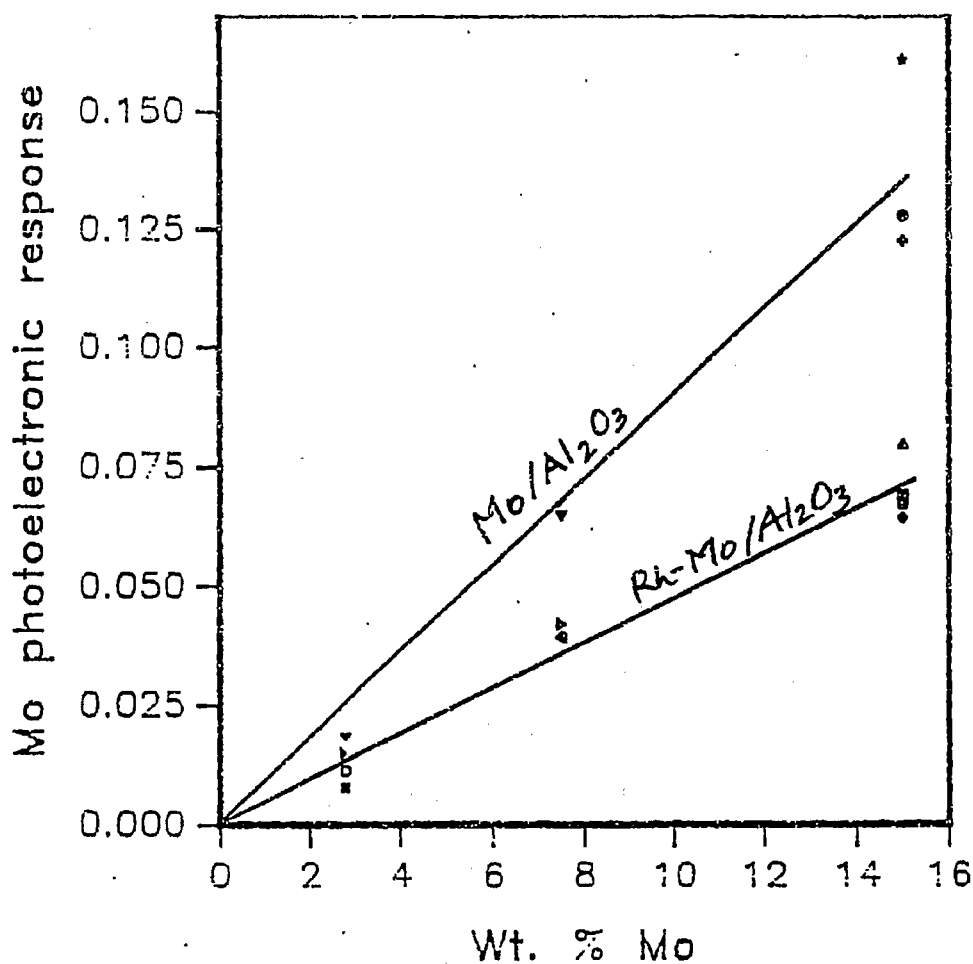
m = density of the modifier atoms in the bulk

s = density of the support atoms in the bulk

$D(\epsilon)$ = detector efficiency, where ϵ is the kinetic energy of ejected photoelectron

σ_m, σ_s = Absorption cross-section for ejected photoelectron from modifier and support respectively

$$\beta_1 = \frac{t}{\lambda_{ps}} \quad (9.2)$$



Key

- | | |
|-------------------------------------------------------------|-------------------------------------------------------------|
| ● 15%Mo/Al ₂ O ₃ --Oxidised | ● 3%Rh15%Mo/Al ₂ O ₃ --Reaction |
| ⊕ 15%Mo/Al ₂ O ₃ --Reduced | ✓ 7.5%Mo/Al ₂ O ₃ --Oxidised |
| ⊛ 15%Mo/Al ₂ O ₃ --CO chemisorbed | ▼ 7.5%Mo/Al ₂ O ₃ --Reduced |
| ○ 3%Rh2.8%Mo/Al ₂ O ₃ --Oxidised | ▶ 3%Rh7.5%Mo/Al ₂ O ₃ --Oxidised |
| ⊠ 3%Rh2.8%Mo/Al ₂ O ₃ --Reduced | ◀ 3%Rh7.5%Mo/Al ₂ O ₃ --Reduced |
| ▲ 3%Rh15%Mo/Al ₂ O ₃ --Oxidised | △ 3%Rh7.5%Mo/Al ₂ O ₃ --COchemisorbed |
| ◊ 3%Rh15%Mo/Al ₂ O ₃ --Reduced | ▽ 3%Rh2.8%Mo/Al ₂ O ₃ --Oxidised(+) |
| ⊞ 3%Rh15%Mo/Al ₂ O ₃ --CO chemisorbed | ⋄ 3%Rh2.8%Mo/Al ₂ O ₃ --Reduced(+) |

Figure 9.10: Mo photoelectronic response for Mo/Al₂O₃ and Rh-Mo/Al₂O₃ catalysts after different treatments

REPRODUCED FROM BEST
AVAILABLE COPY

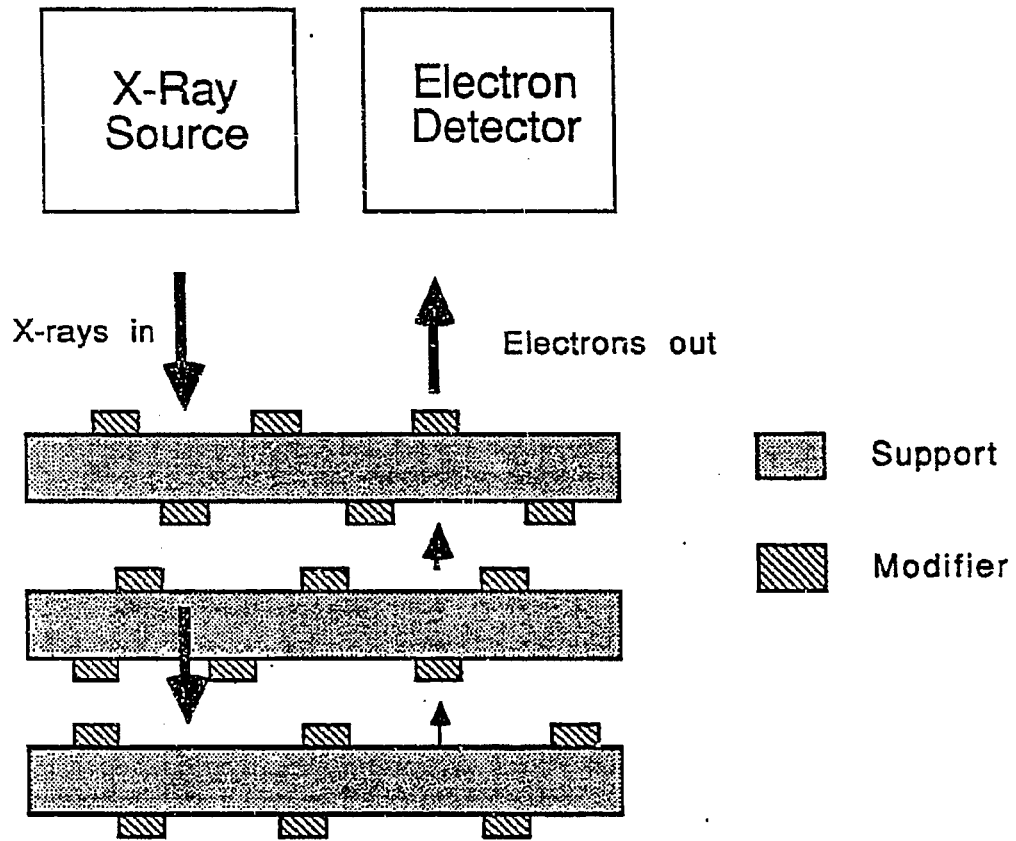


Figure 9.11: Schematic diagram of Kerkhof and Moulijn¹³ model for estimation of particle size from XPS photoelectronic response

where t = thickness of support wall

$$t = \frac{2}{\rho \times S_0} \quad (9.3)$$

where ρ = density of the support

S_0 = surface area of the support

λ_{ss} = inelastic mean free path of ejected photoelectron from support traveling through support

$$\beta_2 = \frac{c}{\lambda_{ms}} \quad (9.4)$$

where λ_{ms} = inelastic mean free path of ejected photoelectron from modifier through the modifier.

c = thickness of modifier crystallite on the support

and

$$\alpha_1 = \frac{c}{\lambda_{mm}} \quad (9.5)$$

where λ_{mm} = inelastic mean free path of the ejected photoelectron from the modifier through the modifier

Since β_1 and β_2 are functions of t only, and all λ_{ij} should be same for Mo Al_2O_3 and Rh-Mo/ Al_2O_3 . The only parameter which changes is 'c'.

In a monolayer catalyst the sixth term on the right hand side of equation (9.1) is unity. It is well known that Mo-oxide forms a monolayer on Al_2O_3 . The lower photoelectronic response of Mo in Mo-Rh/ Al_2O_3 cannot be due to blocking of Mo-oxide by Rh crystallites. This is because Rh dispersion is low and it covers a very small amount of the support surface area. The decrease in photoelectronic

response of Mo cannot be due to mixed compound formation because (i) No detectable mixed oxide phase is found in X-Ray Diffraction studies in calcined and used catalyst and (ii) After reduction Mo exists in $+6$ and $+5$ state and Rh exists in metallic state, and under these oxidation states of Rh and Mo no mixed compound is possible. Hence the decrease in photoelectronic response is due to aggregation of Mo-oxide in the presence of Rh.

Hence using equation (9.1) for $\text{Mo}/\text{Al}_2\text{O}_3$ and $\text{Mo-Rh}/\text{Al}_2\text{O}_3$

$$\frac{\left(\frac{I_{\text{Mo}}}{I_{\text{Al}}}\right)_{\text{Mo-Rh}/\text{Al}_2\text{O}_3}}{\left(\frac{I_{\text{Mo}}}{I_{\text{Al}}}\right)_{\text{Mo}/\text{Al}_2\text{O}_3}} = \frac{(1 - e^{-\alpha})}{\alpha} \quad (9.6)$$

The ratio of relative photoelectronic response should be independent of all the equipment parameters.

From figure 9.11 and equation (9.6) we get $\alpha \approx 0.93$

Since $\lambda_{pp} \approx 20 \text{ \AA}$, hence $c \approx 20 \text{ \AA}$.

Hence the particle size of Mo-oxide crystallite in $\text{Mo-Rh}/\text{Al}_2\text{O}_3$ is $\approx 20 \text{ \AA}$.

9.6.4 Effect of pH of the Solution on Molybdena Aggregation

In the previous section the aggregation of molybdena was observed. This aggregation might be a true aggregation or an artifact of method of preparation. In the preparation of Rh-Mo Al_2O_3 catalysts, the catalysts was given one more acid treatment than with $\text{Mo Al}_2\text{O}_3$. This extra acidic solution is contacted when the Rh-nitrate solution with a pH of 1-2 is used for impregnation. Mo is also impregnated at pH of 1-2 [14,15]. The theory of impregnation of ions from aqueous solutions on oxide surfaces was discussed in chapter 2. Since pZPC (pH corresponding to the point of zero charge) for Al_2O_3 is 8-9, the surface is

positively charged at a pH of 1-2. The predominant Mo species at pH of 1-2 and at concentrations corresponding to no excess solution impregnation for 7.5wt% Mo is $\text{Mo}_{19}\text{O}_{59}^{4-}$ [16]. However as evidenced by the linear photoelectronic response of $\text{Mo}/\text{Al}_2\text{O}_3$, hence Mo is dispersed during the calcination in $\text{Mo}/\text{Al}_2\text{O}_3$.

To check the effect of pH a batch of 7.5% $\text{Mo}/\text{Al}_2\text{O}_3$ catalysts is taken and its pore volume was measured. Then, a solution with a pH of 1 was prepared, simulating the conditions for impregnating rhodium salts. Then, the exact pore volume of the solution was added to the catalysts. The catalysts was then calcined in air. The photoelectronic response for the original catalysts and the pH treated catalysts did not differ by more than 10%. This should be compared with a 50% decrease in the photoelectronic response of $\text{Mo}/\text{Al}_2\text{O}_3$ when Rh was added to $\text{Mo}/\text{Al}_2\text{O}_3$. Hence the aggregation of molybdena is a true effect and not an artifact of method of preparation.

9.7 Electron Spin Resonance Spectroscopy

Electron Spin Resonance Spectroscopy was performed specifically to qualitatively investigate the chemical state of molybdenum. ESR was performed both at room temperature and at liquid nitrogen temperature. ESR spectra were collected for calcined and CO-dosed Al_2O_3 , $\text{Mo}/\text{Al}_2\text{O}_3$, $\text{Rh}/\text{Al}_2\text{O}_3$ and $\text{Rh-Mo}/\text{Al}_2\text{O}_3$. Figure 9.12 shows the ESR spectra of Al_2O_3 and 3% $\text{Rh}/\text{Al}_2\text{O}_3$ in the reduced state. Here again, both samples were calcined, reduced under flowing hydrogen, followed by CO adsorption at room temperature. There are no strong peaks in both alumina and $\text{Rh}/\text{Al}_2\text{O}_3$. The CATAPAL alumina used is made from aluminum isopropoxide and is one of the most pure form of industrial alumina available. Thus there is no evidence of any ESR-active species in the sample. This is consistent with the XPS results, because Rh exists either as Rh-metal crystallite or as isolated gem-dicarbonyl species. In Rh-metal crystallite, the oxidation state

of Rh is zero. Rh(0) is a d^9 state with unpaired electron, however, because it forms a metal crystallite the electrons are paired. In contrast, the gem-dicarbonyl species Al-O-Rh(I)(CO)₂ has rhodium in oxidation state of 1, which is d^8 . The gem-dicarbonyl species has all electrons paired, hence no ESR-active centers are expected. Also, spectra collected at liquid nitrogen temperature did not show any ESR-active centers.

ESR spectra of calcined 7.5%Mo/Al₂O₃ and 3%Rh 7.5%Mo/Al₂O₃ at liquid nitrogen temperature did not show any ESR-active center in both samples. The spike in the spectra is due to an external standard, DPPH. Molybdenum in calcined Mo/Al₂O₃ is expected to be in Mo(+6) state. Mo(+6) is a d^0 state and has no unpaired electron, hence is ESR-inactive. Hence Mo is an ESR inactive center in calcined 3%Rh 7.5%Mo/Al₂O₃ catalysts. This is consistent with the XPS results, because XPS shows that Mo exists predominantly in +6 oxidation state in calcined 7.5%Mo/Al₂O₃ and 3%Rh 7.5%Mo/Al₂O₃ catalysts.

Figure 9.13 shows the ESR spectra of 15%Mo/Al₂O₃ after various sample treatments. Spectra C is for calcined 15%Mo/Al₂O₃ at liquid nitrogen temperature. There is a small amount of ESR-active center which shows up at the same g value as Mo(+5) centers. Small amount of Mo(+5) in calcined Mo/Al₂O₃ has been observed by Rao et al.[9], especially when the catalysts is evacuated. ESR spectra of CO-dosed 15%Mo/Al₂O₃ is shown in spectra B. The g-value of the ESR-active center in 15%Mo/Al₂O₃, presumed to be Mo(+5) is same as the g-value for 7.5%Mo/Al₂O₃, i.e. 1.9611. This is consistent with the results reported by Kevan et al. [17,18]. Here again, there is no fine structure around the ESR peak. This may be due to either zero field or due to heterogeneity in the sample. ESR spectra was also collected at liquid nitrogen, with the aim of elucidating the fine structure around these peaks. However as seen in spectra A, there is no fine structure even at liquid nitrogen temperature.



Figure 9.12: Electron spin resonance spectra of (A) reduced and CO-dosed Al_2O_3 at room temperature and (B) reduced and CO-dosed ^{357}Rh Al_2O_3 at room temperature



Figure 9.13: Electron spin resonance spectra of (A) reduced and CO-dosed ^{157}Mo Al_2O_3 at liquid nitrogen temperature, (B) reduced and CO-dosed ^{157}Mo a at room temperature and (C) calcined ^{157}Mo Al_2O_3 at liquid nitrogen temperature

Figure 9.14 shows the ESR spectra of 3%Rh 15%Mo/Al₂O₃ catalysts. The absence of any ESR-active center in spectra C for calcined 3%Rh 15%Mo/Al₂O₃ is indicative of rhodium being in (+3) state (d⁶) and Mo being in +6 oxidation state (d⁰). Comparison of this spectra with spectra C of figure 9.13 shows that small amounts of (+5) state observed in Mo/Al₂O₃ is not seen here. Spectra B and C are ESR spectra for reduced and CO-dosed 3%Rh 15%Mo/Al₂O₃ catalysts at room temperature and liquid nitrogen temperature respectively. Here again, Mo(+5) is seen without any fine structure.

In conclusion, the ESR experiments supplement and corroborate the XPS results to show that Mo exists in +6(d⁰) oxidation state after calcination. Also, rhodium exists in +3(d⁶) oxidation state after calcination and in metallic particles or in the form of isolated Rh(I) species after reduction. Reduction of molybdenum containing samples show the presence of Mo(+5). The g-value for Mo(+5) is same in all catalysts. No fine structure is observed around the Mo(+5) peaks. There are no ESR-active centers in calcined and CO-dosed Al₂O₃ and 3%Rh/Al₂O₃ catalysts.

9.8 Ion-Scattering Spectroscopy

The evidence for aggregation of molybdena was shown in the XPS results. However the sampling depth of XPS experiment ranges from 10 to 30 Å from the surface [19]. Hence XPS results does not give any information about top layer aggregation. ISS experiments were done because ISS is sensitive to the top one or two layers. Dr. Dennis Swartzfager ran the ISS experiments at the duPont Experimental Station.

The aggregation of molybdena was studied using ion scattering spectroscopy. In low energy ion-scattering spectroscopy experiments, the sample is bombarded with a beam of ions. A very small fraction of these ions undergo elastic scattering.



Figure 9.14: Electron spin resonance spectra of (A) reduced and CO-dosed $37\text{Rh } 157\text{Mo } \text{Al}_2\text{O}_3$ at room temperature, (B) reduced and CO-dosed $37\text{Rh } 157\text{Mo } \text{Al}_2\text{O}_3$ at liquid nitrogen temperature and (C) calcined $37\text{Rh } 157\text{Mo } \text{Al}_2\text{O}_3$ at liquid nitrogen temperature

The intensity of the scattered beam is measured as a function of angle of scattering. The peak position is a function of the nature of the element while the intensity is related to atomic density on the surfaces. Ion scattering is a surface sensitive tool and gives surface densities of elements in the top 1 to 2 atomic layers. The intensity of the peak is proportional to the number of atoms per unit surface area.

As discussed in chapter 2, it is not possible to separate Mo and Rh peaks with $^4\text{He}^-$ ion source. Figure 9.15 shows the ion scattering spectra of calcined 15%Mo/Al₂O₃, 3%Rh/Al₂O₃ and 3%15%/Al₂O₃ respectively. A typical ISS spectra consists of intensity versus the energy of the outgoing ions. The first peak corresponds to the oxygen on the topmost layer of the catalysts. The second peak corresponds to aluminum. Also, there is a blocking effect due to the larger size of the oxygen anion. The third peak corresponds to rhodium and molybdenum atoms or ions on the surface. Since the atomic number of molybdenum and rhodium are very close (42 and 45), these peaks corresponding to these two elements cannot be separated using helium ions. Use of higher atomic number ions increases the resolution, however the fraction of ions back-scattered decreases substantially.

Figure 9.16 shows the ISS spectra of neon sputtered (A) 3%Rh/Al₂O₃, (B) 15% Mo/Al₂O₃ and (C) 3%Rh 15%Mo/Al₂O₃ catalyst. The average approximate sputter length was 150 Å. As explained in chapter 2, a single unique sputter length cannot be ascribed for sputtering on powdered samples. Table 9.7 shows the intensity ratios of various elements ratioed with respect to aluminum peak. From table 9.7 it is evident that the $(I_{Mo} - I_{Rh}) / I_{Al}$ is smaller for 3%Rh 15%Mo Al₂O₃ than 15%MoAl₂O₃. This implies that either Mo is aggregated in the presence of Rh, or it is being covered up by Rh crystallites. If the state of aggregation of molybdena is same in Mo Al₂O₃ and Rh-Mo Al₂O₃ catalysts, then the blocking of molybdena by rhodium will decrease the contribution of molybdena to the ISS signal intensity. However because molybdena forms a monolayer on Mo, Al₂O₃

catalysts, this decrease in intensity of molybdena by caused by rhodium covering molybdena would be insignificant. Hence the decrease in intensity of the composite peak of Mo and Rh is due to aggregation of molybdena. This confirms and corroborates the XPS results.

Table 9.7: ISS intensity ratios of various elements for 3%Rh/Al₂O₃ . 15%Mo/Al₂O₃ and 3%Rh 15%Mo/Al₂O₃ catalysts

Catalysts	treatment	I _O /I _{Al}	(I _{Mo} - I _{Rh})/I _{Al}
15%Mo/Al ₂ O ₃	calcined	0.74	0.89
3%Rh/Al ₂ O ₃	calcined	0.37	0.15
3%Rh15%Mo/Al ₂ O ₃	calcined	0.63	0.84
15%Mo/Al ₂ O ₃	Neon sputtered	0.47	0.47
3%Rh/Al ₂ O ₃	Neon sputtered	0.32	0.06
3%Rh15%Mo/Al ₂ O ₃	Neon sputtered	0.51	0.04

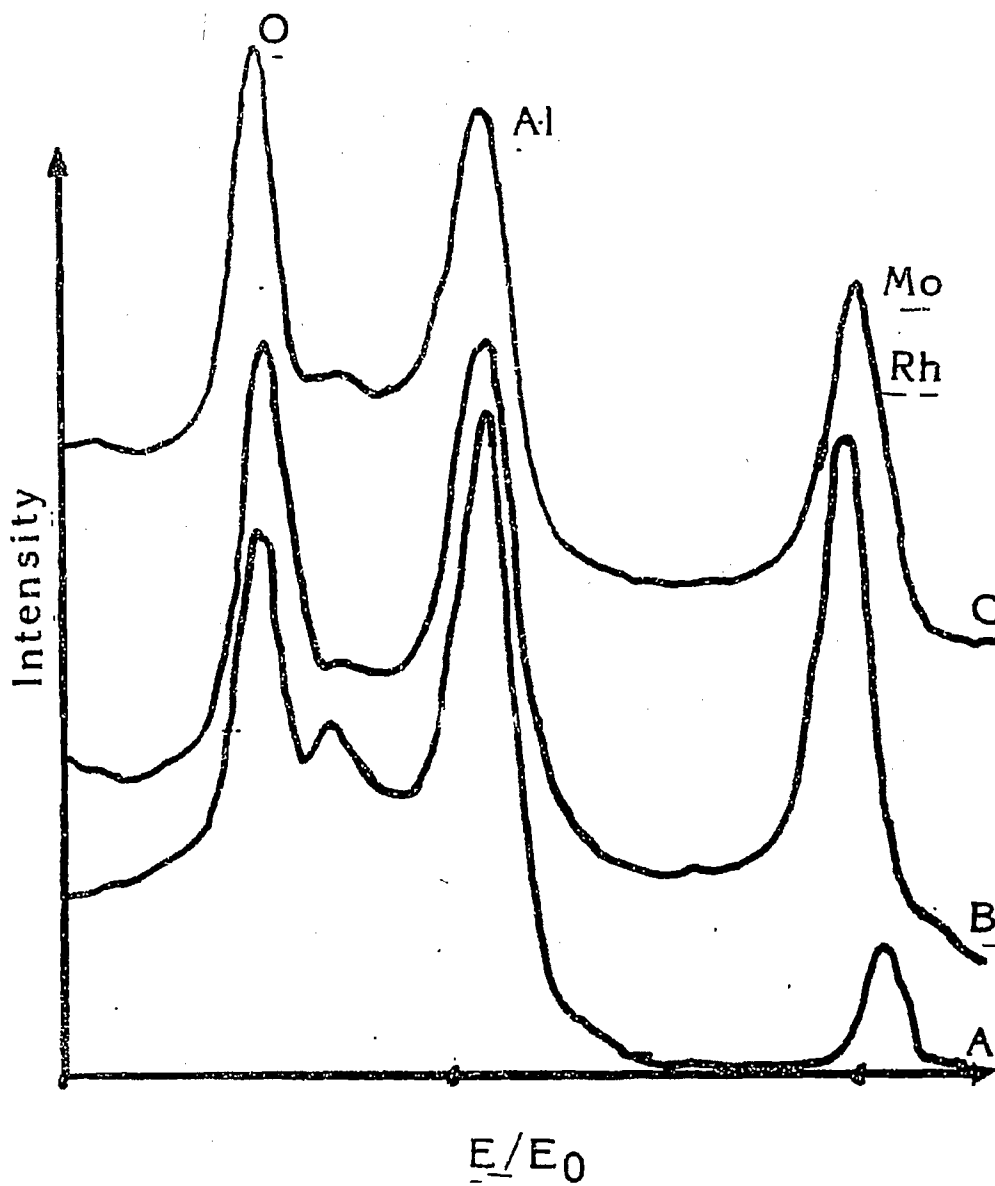


Figure 9.15: Ion-Scattering spectra of calcined (A) 3% Rh Al_2O_3 ; (B) 15% Mo Al_2O_3 and (C) 3% Rh 15% Mo Al_2O_3 catalysts

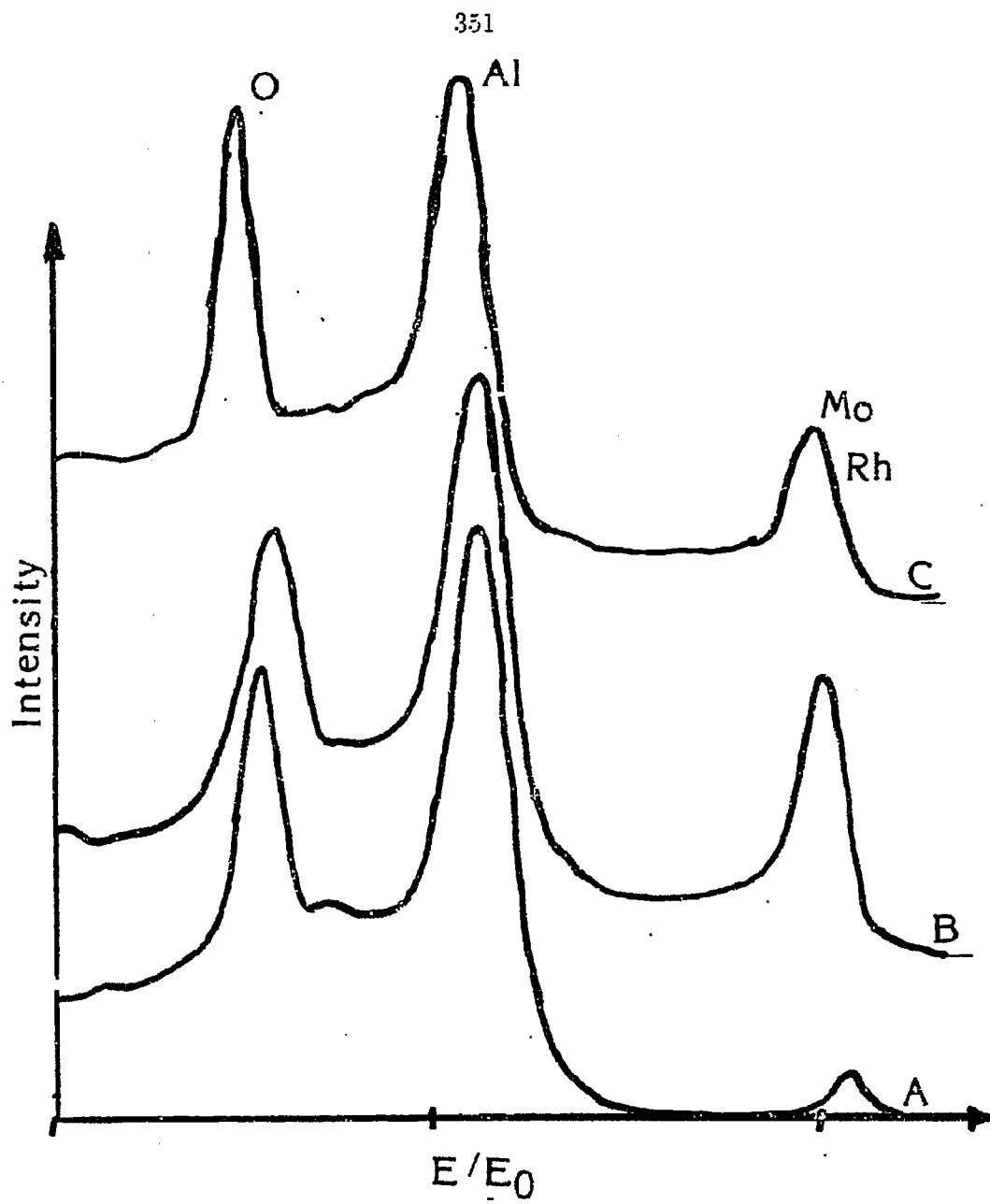
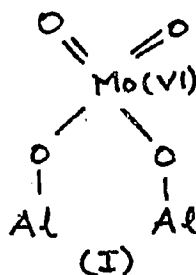


Figure 9.16: Ion-Scattering spectra of sputtered (A) 3% Rh Al₂O₃ (B) 15% Mo Al₂O₃ and 3% Rh 15% Mo Al₂O₃ catalysts

The topmost layer of alumina surface contains hydroxyl groups, oxygen anions and aluminum cations. While the molybdenum on the surface of calcined catalysts exists predominantly as species(I).



The surface density of oxygen atoms is higher in molybdenum containing samples because molybdenum exists predominantly as species(I) and oxygen atoms have higher radius. Hence I_O/I_{Al} in ISS provides a good measure of Molybdenum dispersion on the first two layers. The higher I_O/I_{Al} in Mo/Al_2O_3 compared to $Rh-Mo/Al_2O_3$ further proves that molybdenum in $Rh-Mo$ catalysts is aggregated.

9.9 Solid-State Nuclear Magnetic Resonance Spectroscopy

9.9.1 Chemical Shifts

Solid-State NMR spectroscopy is used to investigate the nature of carbonyls and their spatial distribution in $Rh-Mo/Al_2O_3$ catalysts. The sample preparation method is outlined in chapter 4. Both single-pulse and cross-polarization techniques were used. The spectral width used was 14kHz. The pulse delay was 5 sec and the number of scans were 63000. The contact time for the cross-polarization experiments was 8ms.

Figure 9.17 shows a typical NMR spectra of CO adsorbed on Rh/Al_2O_3 . In contrast, no detectable NMR signal was observed for $Rh-Mo/Al_2O_3$ catalysts for twice the amount of scan time. The adsorption of $^{13}C'O$ on these samples was

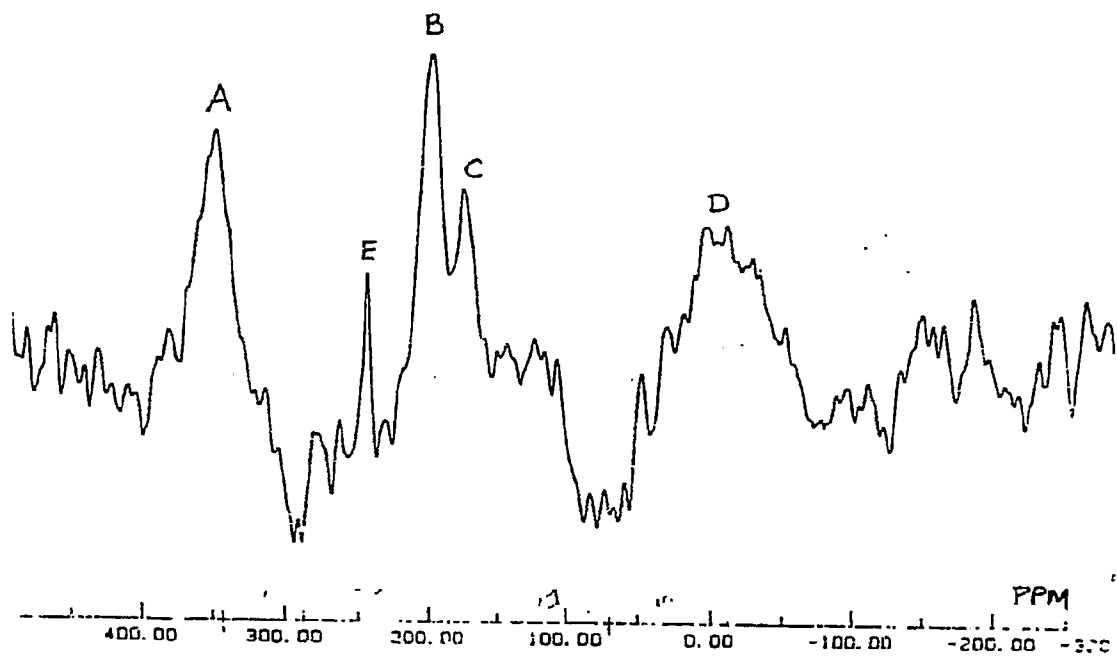


Figure 9.17: ^{13}C NMR spectra of ^{13}CO adsorbed on reduced 3% Rh/Al₂O₃ at room temperature with magic angle spinning, cross-polarization and high power decoupling

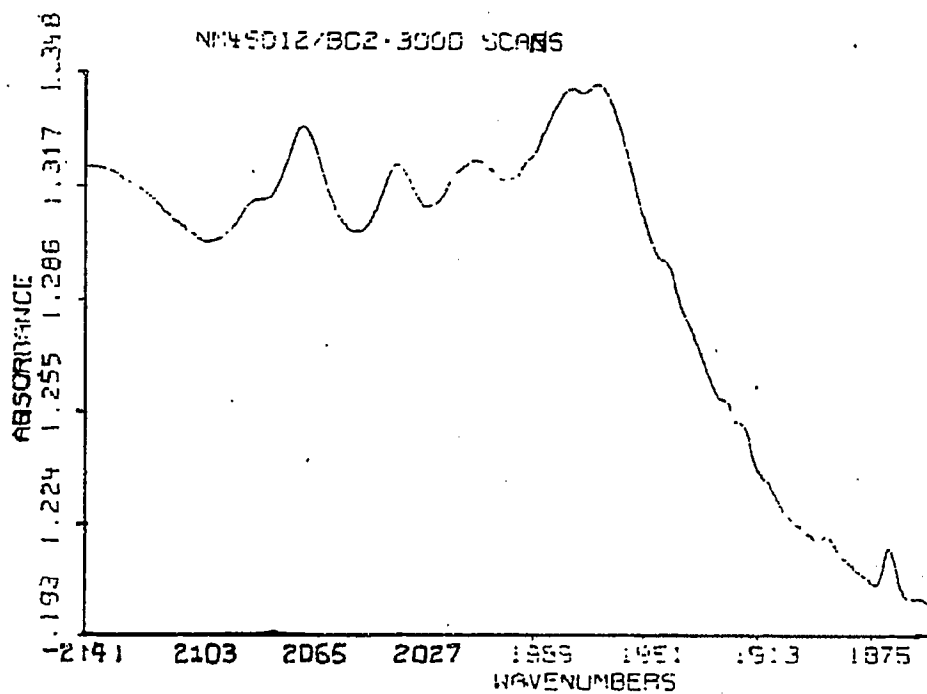


Figure 9.18: IR spectra of $^{13}\text{C}^{18}\text{O}$ adsorbed on $37\text{Rh } 7.5\%\text{Mo } \text{Al}_2\text{O}_3$ at room temperature after the NMR experiment

cross-checked using IR spectroscopy. The sample after the NMR experiment was taken into the glove box under nitrogen. The $^{13}\text{C}O$ dosed sample was then mixed with degussa alumina for ease of pressing wafers. This mixture was then pressed in the form of a self supporting IR transparent wafer. An infrared spectra of this wafer is given in figure 9.17. The IR spectra shows the adsorbed $^{13}\text{C}O$ on Rh-Mo/ Al_2O_3 catalysts. The absence of a detectable NMR signal is then attributed to the presence of Mo+5 paramagnetic centers in the sample.

9.9.2 Calculations

As reported earlier, on reduction molybdena in Rh-Mo/ Al_2O_3 is partially reduced to Mo(+5). Mo (+6) has no unpaired electron while Mo(+5) has one unpaired electron. This paramagnetic species causes an intense fluctuating magnetic field at the NMR-active nuclei. This leads to rapid relaxation of NMR-active nuclei. The theory of relaxation of NMR-active nuclei by fixed paramagnetic species in space was is given elsewhere[20-23]. As long as one ^{13}C nucleus is relaxed on the metal crystallite, all the rest of the ^{13}C nuclei can be relaxed by the phenomenon of spin diffusion. Since all the adsorbed $^{13}\text{C}O$ molecules on a metal crystallite are connected through the conduction electrons, the relaxation of one ^{13}C nucleus relaxes all the other ^{13}C nuclei.

The results indicate that $^{13}\text{C}O$ adsorbed on Rh in Rh-Mo/ Al_2O_3 does not give any NMR signal. This attributed to the fast relaxation by paramagnetic species. The peak width of a NMR signal is inversely proportional to the spin-lattice relaxation time, T_1 . if the spin lattice relaxation time is much smaller than spin-spin relaxation time T_2 . In the absence of an observable peak an estimate of the lower bound on the peak width can be made. This can be converted to upper bound on T_1 , which in turn leads to upper bound on the minimum separation distance between Mo(+5) and ^{13}C nuclei by the following expression. The spectral

width used gives the range of zeeman frequencies excited and hence gives a lower bound on the peak width.

The electron spin-lattice relaxation time is typically 10^{-7} to 10^{-8} sec at 300K [23,24].

$$\frac{1}{T_1} = \frac{3\hbar^2\gamma_S^2}{10\tau r^6 H_0^2} \quad (9.7)$$

where

γ_S is the gyromagnetic ratio of the unpaired electron

r is the minimum separation distance between the NMR-active center and the paramagnetic center

H_0 is the magnetic field strength

The above order of magnitude analysis gives a separation distance of 0(5 Å). This close proximity of Mo(+5) and CO adsorption sites means that diffusion of chemical intermediates from one The minimum width of the detectable peak is ≈ 1000 ppm. This can be converted to frequency units and is 25×10^3 Hz. This gives rise to an upper bound on the spin-lattice relaxation time and is

$$T_1 > 4 \times 10^{-5} \text{ sec}$$

This upper bound of T_1 is then used to find the order of magnitude separation between the paramagnetic center and the NMR-active center.

Figure 9.19 shows the model used for relaxation of NMR-active nucleus by fixed paramagnetic centers. Since the expression for T_1 given in equation (9.7) averages over $\frac{1}{r^6}$. Thus the contribution from the lowest r is predominant. This r^6 dependence arises from dipolar coupling between the nuclear spin Hamiltonian

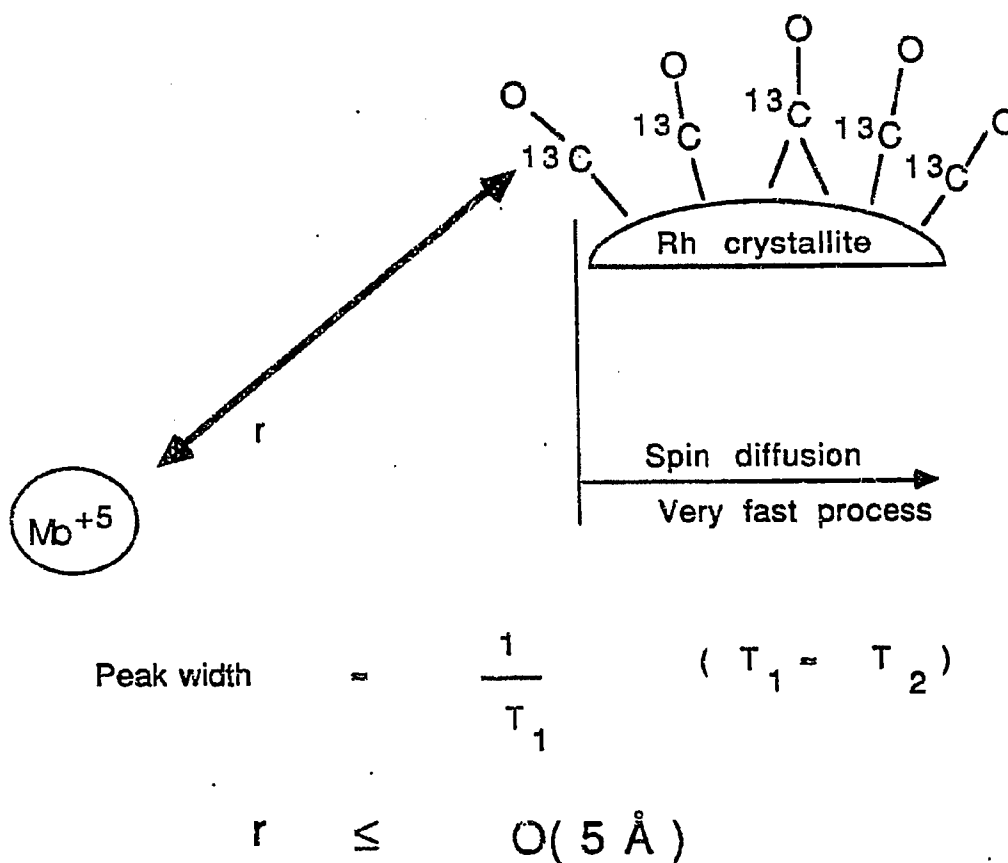


Figure 9.19: Model for relaxation of NMR-active nucleus by fixed paramagnetic species in space

and the electron spin Hamiltonian. A brief summary of this theory is given in chapter 2. Secondly when an NMR-active nucleus is adsorbed on a metal crystallite, there is an overlap between the electrons of the adsorbate and the metal crystallite conduction electrons. Thus all the electrons on the NMR-active centers on the adsorbates are connected through the spin lattice relaxation time. Thus if the nearest NMR-active nuclei is relaxed, then the rest of the nuclei on the same metal crystallite are also relaxed. This relaxation of nuclear spins through the metal conduction electrons occurs through a well-known process of Spin-Diffusion. Details of the theory of spin-diffusion are given elsewhere[23]. Thus it is important to recognize that the order of magnitude of the distance obtained from equation (9.7) is the ensemble average of the minimum distance between the paramagnetic center and the NMR-active center.

9.10 Discussions

From XRD results, the average rhodium crystallite size was less than 30\AA in Rh/ Al_2O_3 and Rh-Mo/ Al_2O_3 catalysts. Thus even though the amount of CO chemisorbed decreases rapidly with the amount of molybdena added, no concomitant increase in the rhodium particle size is observed. Also, the TEM results are consistent with XRD results since the particle size is below the detectable limit in Rh/a and Rh-Mo/ Al_2O_3 .

The chemical state or the oxidation state of rhodium is zero under reaction conditions. The IR results show the presence of the linear and bridged species and gem-dicarbonyl species. The linear and bridges species are formed on the metal crystallite, where the oxidation state of rhodium is zero. In contrast, the gem-dicarbonyl species is attached to an isolated rhodium atom with an oxidation state of one. As shown in chapter 7, and in many other investigations, the gem-dicarbonyl species is formed under oxidizing environments and plays no significant

direct role in the catalytic conversion of CO to hydrocarbons and oxygenates. Also, because the binding energy of Rh(0) is very close to the binding energy of Rh(I), it is difficult to differentiate between Rh(0) and Rh(I) from the XPS spectra. However as shown by the IR and XPS results, under reaction conditions rhodium exists in metallic state and there is no change in the chemical state of rhodium with addition of molybdena. This is consistent with results reported by Jackson et al.[25] on Rh/MoO₃.

After reduction under hydrogen at 500C for 1hour, molybdenum exists in +5 and +4 oxidation state, however most of the molybdenum exists in +5 oxidation state. This is consistent with the results of other investigators[9-12]. This is also consistent with the ESR spectroscopy results in which Mo(+5) is obtained. The catalytic species may be Mo(+5) or Mo(+4). Hall et al. [26] have reported that Mo(+4) is the hydrogenation site for many structure-insensitive reactions.

Mo/Al₂O₃ forms a monolayer on alumina surface. The effect of rhodium on the physical state of the molybdena is drastic. The presence of rhodium aggregates rhodium and this aggregation takes during the calcination stage. Thus the molybdena is in an aggregated form in the presence of rhodium. After reduction, rhodium oxide particles are reduced to rhodium crystallite and the molybdena is reduced from +6 state to a mixture of +5 and +4 state. Furthermore, the aggregation is not due an artifact of the method of preparation. This was checked by contacting the Mo/Al₂O₃ catalysts with an acidic solution of pH=1. This aggregation may be caused due a formation of mixed oxide of molybdena and rhodium oxide. MoRh₂O₆, mixed oxide is well-known and is formed by mixing MoO₃ and Rh₂O₃ at 600C. Prins et al.[27] have found shift in the TPR spectrum of Rh/Al₂O₃ and Rh-Mo/Al₂O₃ and have attributed this to formation of mixed oxide. Thus the quantitative XPS results reported in earlier section are consistent with the results of Prins et al.[27].

After reduction since the rhodium oxide is converted to metallic state and the molybdena is converted to sub-oxide. At this point the mixed oxide separates into Rh metal and partially reduced MoO_3 . In contrast the molybdena in $\text{Mo}/\text{Al}_2\text{O}_3$ does not aggregate on calcination because of the absence of rhodium. The state of aggregation of molybdenum is not affected by catalysts treatments such as reduction, CO chemisorption and reaction because the Mo photoelectronic response does not change appreciably on these treatments. The ISS results corroborate the XPS results. The particle size of Mo in Rh-Mo/ Al_2O_3 can be calculated using Kerkhof and Moulijn model and is $\approx 20\text{\AA}$. This is consistent with the XRD results because the particle size calculated from quantitative XPS analysis is less than the minimum particle size detectable by XRD. Figure 9.20 shows a schematic of the presence of mixed oxides and aggregation of molybdena after various treatments.

Researchers from Union Carbide were the first to observe the dramatic effect of addition of small quantities of poorly reducible oxides such as those of Mn, Mo, W, Fe on the activity and selectivity of Rh/ SiO_2 catalysts[28,29]. Based on their observations[30] that the promoter ions exist in close proximity to the Rh crystallites, they postulated that the promoter forms a mixed oxide with Rh and this would decrease the rate of CO dissociation, thereby decreasing the carbon build-up on the catalysts, which would result in higher activity of the catalysts. This explanation was later proved to be incorrect[31-33]. The XRD, IR and XPS results shown in this chapter do not support the above hypothesis.

Several investigators have used the differences in the acidity-basicity of the support and the modifier to explain different product distribution. Basic supports such as magnesia were reported to favor oxygenates formation [34,35], but no clear correlation between basicity of the support and its activity or selectivity when Rh was supported on it could be found[36]. Recall that the reaction studies of different modifiers listed in chapter 5 do not support this hypothesis.

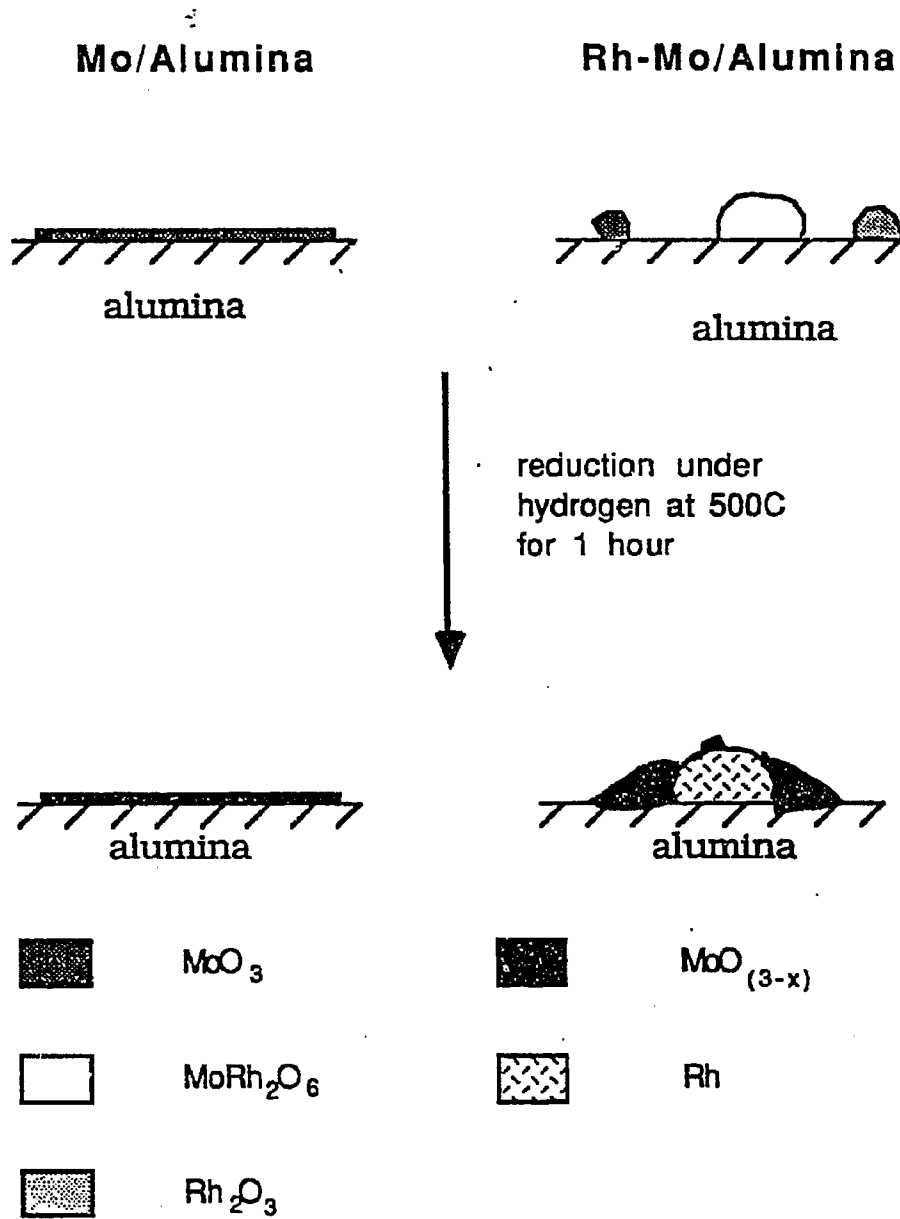


Figure 9.20: Schematic diagram of the phases in $\text{Mo}/\text{Al}_2\text{O}_3$ and $\text{Rh-Mo}/\text{Al}_2\text{O}_3$ in calcined and reduced state

The oxidation state of Rh is speculated to play a major role in determining the activity and the selectivity [31,37-39]. The most comprehensive mechanism so far, was put forward by Sachtler and coworkers [37,38], to account for the wide range of product distributions observed for supported catalysts in CO hydrogenation. They deduced this from several pieces of experimental information. According to their "dual-site" model, dissociative chemisorption of CO and hydrogen, the formation of CH_2 groups, and chain propagation occur on the ensemble of Rh atoms. Termination of chains by H abstraction or addition resulting in the formation of hydrocarbons also take place on the same ensemble sites. Termination of chains by CO insertion, resulting first in acyl groups which can then be hydrogenated to aldehydes or primary alcohols, is thought to occur on different kind of sites, most probably on Rh- ions. A large amount of experimental evidence was collected to support this mechanism in recent years [40,41]. According to this mechanism, formation of methanol occurs by the direct hydrogenation of molecularly chemisorbed CO, again, most probably on the Rh- centers, and for the formation of C2 and higher oxygenates, both kind of sites, viz., Rh ensembles which dissociate CO and Rh- sites which help CO insertion into the adsorbed CH_2 species are needed. Some experimental data [34,42,43] contradict the necessity of Rh- centers for the formation of C2-oxygenates, and show that the selectivity to methanol formation is related to the presence of Rh ions [43]. Although the presence of small amounts of extremely catalytically active Rh(-1) under reaction conditions cannot be ruled out. The evidence from IR studies shows that the gem-dicarbonyl species associated with Rh(-1) does not exist at temperatures greater than 160°C. Yates et al. [44] have shown using isotope exchange experiments that the gem-dicarbonyl species unlike the linear and the bridged species exchanges very slowly, and hence it is unreactive. Thus even when the gem-dicarbonyl is present, it not reactive.

To explain the significant increase in the activity of silica supported Rh catalysts on the addition of Mn or Mo, Sachtler et al.[45] proposed that the true function of the promoter oxide is to decrease the heat of CO chemisorption and stabilization of Rh ions. This could increase the surface concentration of hydrogen which results in increased activity. But strong, experimental evidence[32,46,47] shows that when Mn, Ti or Zr promoter oxide are present on Rh/SiO₂, the IR stretching bands corresponding to bridge bonded CO shift considerable lower frequencies which indicate a lowering of CO bond strength and increased heat of CO chemisorption, contrary to the assumption of Sachtler et al.[45].

The idea of activation of CO by bonding through both ends has been in existence for a long time[48] and it has become popular in the explanation of the metal-support effect enhancing the CO hydrogenation rates over TiO₂ supported group VIII metal catalysts[49-51]. To explain the effect of promoters on Rh catalysts also, this is gaining popularity recently [30,32,38,52], and the in-situ FTIR evidence [32,33,47] for the tilted CO chemisorption mode with its carbon bonded to Rh atoms and the oxygen to the promoter ions overwhelmingly supports this idea. The criticism of this theory stems from the experimental observation that the addition of alkali ions to Rh catalysts decreases the activity for CO hydrogenation, at the same time the IR bands corresponding to the bridge bonded CO on alkali promoted Rh catalysts are also shifted to lower frequencies[53], thereby indicating a strengthening of the Rh-CO bond and weakening of C-O bond. But, it is possible that the effects of this weakening of C-O bond might be different in the two systems during the catalytic reaction and some times the shift can be attributed to dipolar coupling. In contrast, the IR spectra reported here do not show any evidence of weakening of CO bond of adsorbed carbon monoxide. The C-O bond in the gem-dicarbonyl species is slightly strengthened. This may be due to the physical interaction between the oxygen of the molybdena interacting with the carbon atom of the carbonyl ligand of the gem-dicarbonyl species. Thus

the two order of magnitude increase in the rate of CO hydrogenation cannot be explained by weakening of CO bond.

Explaining the very significant changes in the selectivity brought about by Mo is even more complicated. According to the present belief[45], hydrocarbons are formed by CO dissociation on ensembles of Rh atoms and hydrogenation of the surface carbon; methanol is formed on Rh ions; and the other oxygenates (C2- oxygenates) are formed via a dual site mechanism wherein alkyl groups are formed on metallic Rh, migrate to Rh ions on which CO insertion takes place prior to subsequent hydrogenation to form various classes of oxygenated compounds. Thus, the product distribution is simply dependent on the relative concentration of Rh metal and Rh ions on the surface. There are some indications in the current literature that the Rh is in an oxidation state between 0 and 1, and this rhodium site is active for both hydrocarbon and oxygenate formation[54]. Ponec et al.[43] recently showed that C2 oxygenates can form on catalysts that do not contain any Rh- ions, making the Sachtler's explanation doubtful. They also showed that methanol formation is directly related to the amount of Rh+ ions.

Ichikawa et al.[55] classified the promoters into two groups. The first group consists of highly oxophilic elements such as Mn, Ti or Zr that are present as sub-oxides and form an incomplete overlayer on metal; they interact with the O atom of the adsorbed CO on the same metal, thus weakening the C-O bond favoring CO dissociation and hence the formation of alkyl groups. The second group, Zn, Mg and Fe, impede CO dissociation by blocking the "Freundlich" sites on the Rh surface forcing the adsorption of CO in linear position resulting in the suppression of methane formation, promotion of methanol formation and acceleration of migratory insertion of adsorbed CO.

Kiennemann et al. [56] and Kuznetov et al. [57] have proposed that hydrogen assists greatly in the CO bond breaking. This adsorbed CO forms formyl species. However this theory has been long ruled out in FT synthesis.

Dissociation of hydrogen on non-stoichiometric molybdena with transfer to the CO chemisorbed on Rh is one possible reason for enhanced activity. Borg et al. [58], to explain the synergistic effect of Pt-Mo supported Y zeolites in CO hydrogenation, proposed that Mo atoms act as dissociative adsorption sites for CO and carbidic Mo species are hydrogenated by hydrogen dissociated on Pt atoms. However the last explanation can be ruled out because, in the Rh-Mo/Al₂O₃ catalysts investigated in this chapter Mo exists in +5 oxidation state and from IR results there is no CO adsorption on Mo/Al₂O₃ catalysts above 120C.

Thus there are two possible reasons for the increase in the rates of CO hydrogenation on Rh-Mo/Al₂O₃ catalysts. First, the increase in rate can be attributed to the special sites at the interface, where CO is bonded at both ends. This leads to very low frequency CO vibrations and enhanced CO dissociation. The second possible reason is due to the reverse spillover. In this mechanism, the hydrogen is activated and stored in partially reduced molybdena, this hydrogen can also be activated by rhodium and be stored by partially reduced molybdena. Partially reduced molybdena is well-known to form bronzes, i.e., non stoichiometric compounds of hydrogen and molybdenum oxides. Both the hypothesis can explain the increase in the rate of CO hydrogenation on Mo addition. However, each of the hypothesis should be consistent with the detailed characterization and reaction data at various loading of Mo. For example, if the interfacial sites are the active sites. Then in the first approximation, the rate of CO hydrogenation is proportional to the number of interfacial sites in a given amount of catalysts. Various models of decoration of molybdena on Rh crystallite give rise to different variation of number of interfacial sites.

Figure 9.21 shows the various models and the variation in the number of interfacial site versus the surface of the rhodium crystallite covered. The first scheme is called the "radial cover-up" scheme. In this scheme the molybdena particles cover up the particle radially. As more molybdenum is added, the surface of the particle cover-up. This type of distribution of phases is present when the partially reduced oxide wets the support surface better than the metal crystallite surface. In this case the interfacial sites decrease monotonously as more molybdenum is added. If the rate of CO hydrogenation is directly proportional to the number of interfacial sites, then the rate would decrease from 2.8%Mo, to 7.5%Mo to 15%Mo. However experimental evidence shows that the rate of CO hydrogenation increases as molybdena is added till 15%.

The second scheme shown in figure 9.21 is called the "Constant Nucleation Site". In this scheme, there are a fixed number of nucleation sites for molybdena or partially reduced molybdena on supported rhodium metal particle. In this scheme at low molybdena coverage the number of interfacial sites would increase with the amount of molybdena added, since the particle size of the molybdena increases and the number of the interfacial sites increase with the particle size. However at high molybdena coverage, aggregation or agglomeration between the particles takes place which leads to decrease in the number of interfacial sites. Thus there is a maximum in the number of the interfacial sites versus the fraction of rhodium surface blocked by partially reduced molybdena. This maximum occurs when approximately 50% of the rhodium surface is blocked by the partially reduced molybdena. Thus in this scheme the number of interfacial sites go through a maximum at about 50% in the rhodium surface blockage. Recall from the CO chemisorption data shown in earlier sections, the CO chemisorption of 3%Rh/15%Mo/Al₂O₃ is one-fifth of the CO chemisorption of 3%Rh/Al₂O₃. The IR results show that the same stoichiometry is valid for Rh/Al₂O₃ and Rh-Mo/Al₂O₃. The XPS results show that all the Rh is in metallic state and hence has the

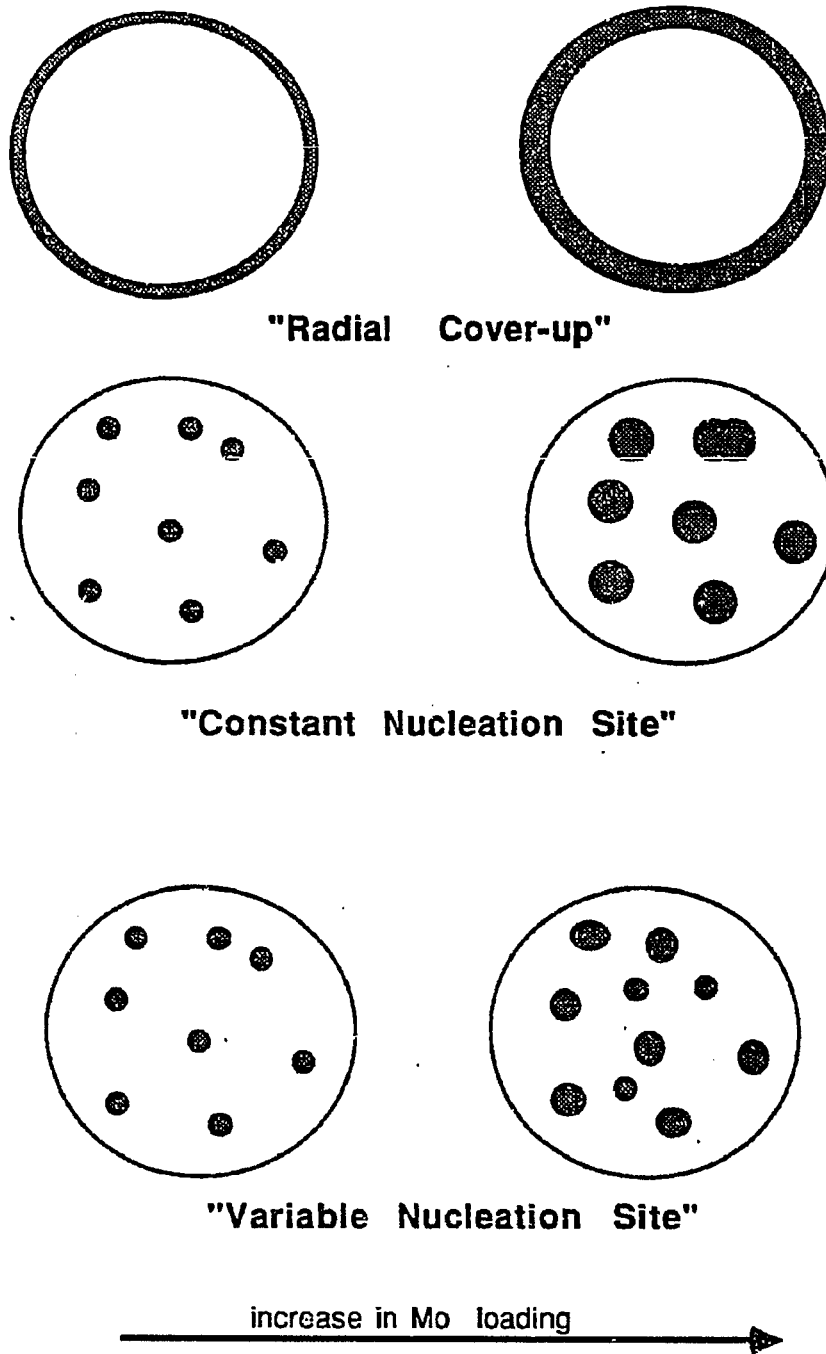


Figure 9.21: Different distribution of an oxide on a metal particle and the variation in the number of interfacial sites

potential of adsorbing CO. Thus 80% of the rhodium surface is blocked on 3%Rh 15%Mo/Al₂O₃ catalysts. Thus the interfacial site mechanism would predict that the rate of CO hydrogenation would reach a maximum when 50% of the rhodium surface is covered. However, the rate of CO hydrogenation increases with the amount of molybdena added. Hence this scheme of interfacial sites can be ruled out.

If the assumption of constant number of nucleation sites of the second scheme is relaxed, i.e., if the number of nucleation sites increase with the amount of Mo added, then the maximum in the interfacial sites versus the fraction rhodium surface blocked shifts to the higher percentage. However this scheme is not probable because of the large energy required to produce increasing number of isolated nucleation sites. Although, the "radially outward growing" scheme shown in figure 9.21 can also explain the data, this scheme is not considered feasible. The key assumption in the above arguments are (i) the particle size of rhodium does not change on addition of molybdena and (ii) the reaction rate of each interfacial site is constant within the Mo loading range investigated.

Recall from chapter 8 that the activation energies for the overall rate of CO consumption does not change appreciably on Mo addition to Rh/Al₂O₃. Therefore, the two order of magnitude increase in the rate of CO hydrogenation cannot be attributed to decrease in CO hydrogenation. The power law fit of the overall rate of CO consumption show that the overall rate of CO consumption is less inhibited by the presence of gas phase CO on Rh-Mo/Al₂O₃ than on the Rh/Al₂O₃. Thus somehow the rate of hydrogenation of CO on Rh-Mo/Al₂O₃ is less inhibited by CO in the gas phase. This shows the good hydrogenation activity of this catalysts. This is further corroborated by the near absence of acetaldehyde from the product distribution. Ethanol unlike acetaldehyde is the predominant C₂ oxygenate. Thus the hydrogenation activity was tested using reactions such as ethylene hydrogenation. However these test reactions are usually performed not

only under conditions that do not represent the CO hydrogenation conditions but also the gas phase environments under these test reaction conditions are different. For example, under CO hydrogenation conditions at high pressure, the partial pressure of CO in the gas phase is high, this leads to virtual blockage of the metal surface by adsorbed CO. This is manifested in the negative exponents for partial pressure of CO in the overall rates of consumption of reactants. Hence it was decided to perform ethylene hydrogenation in the presence and absence of CO in the gas phase.

The ethylene hydrogenation results clearly demonstrate the catastrophic decrease in hydrogenation capability of Rh/Al₂O₃ in the presence of gas phase CO. The ethylene hydrogenation results also show that Rh-Mo/Al₂O₃ behaves like Rh/Al₂O₃ in the absence of gas phase CO while it behaves like Mo/Al₂O₃ in the presence of gas phase CO. Thus under the reaction conditions where the partial pressure of CO in the gas phase is high, the hydrogen activation takes place on the partially reduced molybdena. The ethylene hydrogenation experiments do not rule out the presence of high hydrogen storage ability of partially reduced molybdena. This is not surprising in view of the well-known hydrogen activation and storage capability of molybdenum bronzes, i.e., non-stoichiometric compounds of hydrogen and molybdenum oxides.

However the IR results and the reaction studies on Mo/Al₂O₃ show that CO activation can only take place on Rh metal. Thus in this case there is dual-site mechanism, the first site is the Rh metal where the CO is activated, while the second site is partially reduced molybdena on which hydrogen activation takes place or hydrogen storage takes place. It is important to recognize that the conclusion hold true only for the set of catalysts investigated. This model is consistent with all the schemes listed in figure 9.21. since the larger the amount of molybdena added the higher the hydrogen activation center. It is not clear if the reaction still takes place at the interface. Clearly, the activation barrier for diffusion of CO on

the surfaces is very high, and hence the reaction proceeds through CO activation on rhodium surface. hydrogen diffusion from the partially reduced molybdena followed by reaction. This model is consistent with the observed CO hydrogenation kinetics, since in Rh-Mo/Al₂O₃ catalysts, the hydrogen activation on Rh surface is not limited. Thus the overall rate of consumption does not show strong negative exponent for partial pressure of CO.

A dual-site mechanism is useful when the separation between the two sites is less the diffusion length of intermediates on the surface or the two sites are located close to one another. This is checked by Solid-State NMR spectroscopy. The relaxation calculations clearly show that the minimum of the average distance between the Mo(-5) and the C-13 nuclei on adsorbed CO on Rh particle is of the order of 5Å. Here again the results are consistent with the dual-site mechanism.

However each of the schemes are consistent with a dual-site mechanism where CO is activated by Rh and the hydrogen is activated by partially reduced molybdena. From a catalysts development viewpoint, the dual-site mechanism provide a new tool to design and balance the two sites for optimum activity and selectivity. The near absence fo the inhibition of CO on the overall rate of CO hydrogenation shows that the catalysts is not limited by CO activation centers. If more molybdena is added, the CO chemisorption would decrease further and at some stage, the CO activation center would limit the rate. However for the catalysts investigated, the CO activation centers were not the limiting centers. This implies that there is more rhodium atoms than the minimum needed without affecting the performance of the catalysts.

The higher selectivity of this catalysts is a direct result of the higher activity which leads to lower operating temperature. Recall from chapter 8, that the activation energy for oxygenates is much lower than the activation energy for hydrocarbons. This leads to higher activities at lower operating temperature.

9.11 Conclusions

The Rh-Mo/Al₂O₃ and the Mo/Al₂O₃ catalysts system were characterized with the aim of explaining the unusually high activity of Rh-Mo/Al₂O₃ for CO hydrogenation. The rhodium and the molybdena in both the catalysts system are well-dispersed with a particle size of < 30 Å. The rhodium surface is partially blocked by molybdena or partially reduced molybdena. Rhodium is in metallic state and molybdenum is in the +5 and +4 state under reaction conditions. The addition of rhodium to Mo/Al₂O₃ decreases the dispersion of molybdena due to formation of mixed oxide.

The CO bond is not weakened on Mo addition. The hydrogenation activity of Rh-Mo/Al₂O₃ catalysts stems from the rhodium component in the absence of gas phase CO and from Mo-component in the presence of gas phase CO. The reaction kinetics, the test reaction data and the characterization results are consistent with a dual-site mechanism where CO is activated at the metal center, i.e., at rhodium metal crystallite and hydrogen is activated at the partially reduced molybdena. This second site, the partially reduced molybdena is less inhibited by gas phase CO and is in close proximity with the metal crystallite.

REFERENCES

1. "Powder Diffraction File", International Center for Diffraction Data, Swarthmore, Pennsylvania, 1987.
2. J.P. Badaud, J.P. Fournier and J. Omaly. C.R. Acad. Sci. Ser. C 1977. 284, 921.
3. J.L. Lemaitre, P.G. Menon and F. Delannay, in "Characterization of Heterogeneous Catalysts", ed. F. Delannay, Marcel Dekker, 1984, New York.
4. M.D. Wardinsky and W.C. Hecker, J. Phys. Chem. 1988. 92. 2602.
5. P.S. Braterman, "Metal Carbonyl Spectra", Academic Press, 1975, New York.
6. L.A. Woodward, "Introduction to the Theory of Molecular Vibrations and Vibrational Spectroscopy", Oxford University Press, Oxford, 1972.
7. F. Solymosi and M. Pazstor, J. Phys. Chem. 1985, 89, 4789.
8. P. Basu, D. Panayotov and J.T. Yates, Jr., J. Phys. Chem. 1987, 91, 3133.
9. N. Jagganathan, A. Srinivasan and C.N.R. Rao. J. Catal. 1981. 60. 418.
10. Y. Holl.R. Touroude, G. Maire, A. Muller, P.A. Engelhard and J. Grosman-gin. J. Catal. 1987. 104. 202.
11. D.S. Zingg, L.E. Makovsky, R.E. Tisher, F.R. Brown and D.M. Hercules. J. Phys. Chem. 1980. 84. 2898.
12. N.K. Nag, J. Phys. Chem. 1987. 91. 2324.
13. F.P.J.M. Kerkhof and J.A. Moulijn, J. Phys. Chem. 1979. 83, 1612.
14. P.C. Heimenz. "Principles of Colloid and Surface Chemistry", Marcel Dekker, 1976, New York.

15. C.P. Huang, Y.S. Hseih, S.W. Park, M. Ozden Corapcioglu, A.R. Bowers and H.A. Elliot, in "Metal Speciation: Separation and Recovery", ed. J.W. Patterson and R. Passino, Lewis Publishers, 1987, Chelsea, Michigan.
16. C.F. Baes and R.E. Messmer, "The Hydrolysis of Cations", John Wiley, New York.
17. R.Y. Zhan, M. Narayana and L. Kevan, *J. Chem. Soc. Farad. Trans. 1*, 1985, 81, 2083.
18. M. Narayana, R.Y. Zhan and L. Kevan, *J. Phys. Chem.* 1985, 89, 636.
19. E. Taglauer and W. Heiland, *Appl. Phys.* 1976, 9, 261.
20. N. Bloembergen, *Physica*, 15, 386, 1949.
21. P.G. deGennes, *Phys. Chem. Solids*, 3, 345, 1958.
22. A. Abragam, J. Combrisson and I. Solomon, *C.R. Acad. Sci.* 246, 1035, 1958.
23. B.C. Gerstein and C.R. Dybowski, "Transient Techniques in the NMR of Solids", Academic Press, 1985, New York.
24. T.M. Duncan, J.T. Yates Jr., and R.W. Vaughan, *J. Chem. Phys.* 1980, 73, 975.
25. S.D. Jackson, B.J. Brandreth and D. Winstanley, *Appl. Catal.* 1986, 27, 325.
26. E.A. Lombardo, M. Jacono and W.K. Hall, *J. Catal.* 1980, 64, 150.
27. B.J. Kip, E.G.F. Hermans, J.H.M.C. Van Wolput, N.M.A. Hermans, J. Van Grondelle and R. Prins, in press, *Appl. Catal.*
28. P.C. Ellgen, W.J. Bartley, M.M. Bhasin and T.P. Wilson, *Advan. Chem. Ser.* 1979, 178, 147.
29. P.C. Ellgen and M.M. Bhasin, US patent, 4014913, 1977, and US patent, 4098164, 1978.
30. T.P. Wilson, P.H. Kasai and P.C. Ellgen, *J. Catal.* 1981, 69, 193.
31. F.G.A. Van der Berg, Ph.D. thesis, State University of Leiden, The Netherlands, 1983.

32. M. Ichikawa, T. Fukushima and K. Shikakura, Proc. 8th Intl. Congr. Catal. Berlin. Dechema, Frankfurt, 1984. Vol. II, 69.
33. W.M.H. Sachtler and M. Ichikawa, Div. Petr. Chem., ACS, 1986, 281.
34. J.R. Katzer, A.W. Sleight, P. Gajardo, J.B. Michel, E.F. Gleason and S.F. McMillan, Faraday Disc. of the Chemical Society, 72, 121, 1981.
35. (a) M. Ichikawa, J. Catal. 1979, 56, 127. (b) M. Ichikawa, Bull. Chem. Soc. Japan, 1978, 51, 2268. (c) M. Ichikawa, Bull. Chem. Soc. Japan, 1978, 51, 2273.
36. R.P. Underwood and A.T. Bell, Appl. Catal. 1986, 21, 157.
37. E.K. Poels and V. Ponec, Catalysis. Vol. 6, A Specialist Periodical Report, The Royal Society of Chemistry, London, 1983, 196.
38. W.M.H. Sachtler, Proc. of the 8th Intl. Congr. Catal., Berlin, Dechema, Frankfurt, 1984, Vol. I, 151.
39. (a) P.R. Watson and G.A. Somorjai, J. Catal. 1980, 66, 257. (b) P.R. Watson and G.A. Somorjai, J. Catal. 1981, 72, 347. (c) P.R. Watson and G.A. Somorjai, J. Catal. 1982, 74, 282.
40. M. Ichikawa and T. Fukushima, JCS Chem. Commun. 1985, 321.
41. E.K. Poels, P.J. Mangus, J.V. Welzen and V. Ponec, Proc. 8th Intl. Congr. Catal. Berlin. Dechema. Frankfurt. 1984. Vol. II, 59.
42. J. R. Monnier and G. Apai, Div. Petr. Chem. ACS. 1986. 31, 239.
43. G. van der Lee, B. Schuller, H. Post, T.L.F. Favre and V. Ponec, J. Catal. 1986, 98, 522.
44. D. Payanotov, P. Basu and J.T. Yates Jr., submitted to J. Phys. Chem.
45. F.G.A. van den Berg, J.H. E. Glezer and W.M.H. Sachtler, J. Catal. 1985, 93, 340.
46. T. Fukushima, H. Arakawa and M. Ichikawa, JCS Chem. Commun. 1985, 729.
47. M. Ichikawa and T. Fukushima, J. Phys. Chem. 1985, 89, 1584.
48. E.L. Muetterties and J. Stein, Chem. Rev. 1979, 79, 479.

49. M.A. Vannice and C. Sudhakar, *J. Phys. Chem.* 1984, 88, 2429.
50. R. Burch and A.R. Flambard, *J. Catal.* 1982, 78, 389.
51. M. Levin, A.T. Bell, M. Salmeron and G.A. Somorjai, *Div. Petr. Chem., ACS.* 1986, 317.
52. W.M.H. Sachtler, D.F. Schriver, W.B. Hollenberg and A.F. Lang, *J. Catal.* 1985, 92, 429.
53. J.E. Crowell and G.A. Somorjai, *Appl. Surf. Sci.* 1984, 19, 73.
54. M. Kawai, M. Uda and M. Ichikawa, *J. Phys. Chem.* 1985, 89, 1654.
55. M. Ichikawa, A.J. Lang, D.F. Shriver and W.M.H. Sachtler, *JACS.* 1985, 107, 7216.
56. A. Kiennemann, J.P. Hindermann, R. Breault and H. Idrinn, *Div. Petr. Chem., ACS.* 1986, 46.
57. V.L. Kuznetsov, A. V. Romanenko, I.L. Mudrakovski, V.M. Matikhim, V.A. Shmachkav and Y.I. Yermakov, *Proc. 8th Intl. Congr. Catal. Berlin. Dechema. Frankfurt.* 1984, Vol. V, 3.
58. F. Borg, P. Gallezot, J. Massardier and V. Perrichou, *C1 Mol. Chem.* 1986, 1, 397.

CHAPTER 10

OVERALL CONCLUSIONS AND RECOMMENDATIONS

10.1 Overall Conclusions

The effect and the role of modifiers in supported rhodium catalysts for synthesis of oxygenated products from CO hydrogenation is investigated in this dissertation.

The effect of using various rhodium salts as precursors in a no-excess impregnation on the performance of Rh/Al₂O₃ catalysts was minor. The catalysts derived from acetate precursor were less active and less selective than the catalysts prepared from chloride and nitrate salts. The activity of various supported rhodium catalysts varied as

TiO₂ > Al₂O₃ > La₂O₃ > MgO > SiO₂ > Florisil(silica-magnesia)

and the selectivity to oxygenates varied as

Florisil ~ MgO > La₂O₃ > SiO₂ > Al₂O₃ ~ TiO₂

However, the selectivity is a strong function of conversion. Addition of Ti and Mn to Rh/Al₂O₃ did not substantially change the overall activity or the selectivity to oxygenates. Addition of Sn completely poisoned the formation of oxygenates. In contrast, addition of Mo to Rh/Al₂O₃ increased the overall activity and the selectivity to oxygenates. Similar effects were observed on addition of Mo to Rh/TiO₂ and Rh/SiO₂ catalysts.

The activity of Rh-Na/Al₂O₃ decreases exponentially with the sodium content. The rate of formation of hydrocarbon is decreased much more than the rate of formation of oxygenate formation. This leads to increase in selectivity to oxygenates. Air treatment of Rh-Na/Al₂O₃ causes agglomeration of rhodium particles and decreases the selectivity to oxygenates.

The XPS, and TPR results show that rhodium is present in a metallic state after reduction and under reaction conditions. The physical and chemical state of Na in Na/Al₂O₃ and Rh-Na/Al₂O₃ is the same after various treatments such as reduction under hydrogen at 500C, CO adsorption and reaction. The TPR, XRD and hydrogen chemisorption results show that rhodium is well dispersed in Rh/Al₂O₃ and Rh-Na/Al₂O₃ catalysts with some rhodium surface covered with sodium oxide. IR results show that addition of sodium to Rh/Al₂O₃ hinders the formation of gem-dicarbonyl species associated with Rh(I). This is due to the blocking or removal of surface -OH groups. The IR and XPS results on silylated surfaces also show the decrease in formation of gem-dicarbonyl species. The utility of high pressure IR was seriously hampered by strong interference from gas phase carbon monoxide.

A new method for kinetic pathway analysis, the delplot method, is developed and used. This method consists of plotting $(\text{mole fraction}(y)/(\text{conversion}(x)))^r$ versus x . For a series of first order reactions, a finite intercept of the above plot denotes a product of rank r , while a zero intercept denotes a product of rank $> r$. This method is used to sort products according to their rank. In a complex reaction pathway such as in the Fisher-Tropsch synthesis network, this method can not only be used to find the number of reaction steps but also be used to find the location of slow steps in the reaction pathway. The delplot method is also used to identify reaction steps and separate regimes of conversion where the product rank changes. Many new concepts such as the network rank and the effective rank are developed. The quantitative foundations of this method for any given kinetics

and higher rank products is developed. The theoretical basis for separation of regimes using order of magnitude analysis and singular perturbation analysis was developed. Many variations of the delplot method such as the product-based delplot and the fractional-rank delplot were also developed.

The addition of large amounts of molybdena to Rh/Al₂O₃ increases the rate of CO hydrogenation greater than 10-fold. The water gas shift reaction is accelerated and the selectivity to oxygenates is also increased. The Mo/Al₂O₃ catalysts showed very low activity and no selectivity to oxygenates under similar conditions. On Rh-Mo/Al₂O₃ catalysts methanol production is significantly increased and in addition large amounts of ethers are formed as a result of the higher acidity of the catalysts. Unlike Rh/Al₂O₃, on Rh-Mo/Al₂O₃ almost no aldehydes are formed and no acids are formed. Even though the C₂+ oxygenate selectivity as a fraction of the total oxygenates decreases on addition of Mo, the total amount of C₂+ oxygenates formed at a given conversion increases due to high selectivity to all oxygenates.

The overall activation energy for CO consumption is the same on Rh/Al₂O₃ and Rh-Mo/Al₂O₃. The activation energies of various products are different and this leads to changes in the selectivity with temperature. From kinetic studies it was shown that the overall rate of CO consumption on Rh-Mo/Al₂O₃ was less inhibited by presence of CO in the gas phase as it was for Rh/Al₂O₃. Ethylene hydrogenation results strongly suggest that the hydrogenation activity of Rh-Mo/Al₂O₃ in the absence of CO arises from the Rh-component and in the presence of CO arises from the molybdena-component. On Rh/Al₂O₃ the ethylene hydrogenation activity was poisoned immediately but on Mo/Al₂O₃ the activity was poisoned slowly by added CO.

The delplot analysis shows that at 200°C, 30atm and hydrogen/CO=5, almost all the products are primary products indicating that the water gas shift reaction

and ether formation reactions are fast on the process time scale. Because most of the products are primary products, the effective rank of these products is same as the network rank of these products. Thus by using the permutation of network rank of the products the slow step in the entire reaction network except for methanol formation was identified to be formation of CH_x precursor on the catalysts surface.

The CO chemisorption, TEM and XRD results show that molybdena blocks part of the rhodium crystallites. Rhodium exists in a metallic state after reduction, and molybdena exists as partially reduced molybdena with Mo in Mo(V) and less amount of Mo(IV) oxidation states after reduction. Subsequent treatments such as CO chemisorption and syngas reaction at 200C do not affect the chemical state of Mo and Rh. The ESR spectroscopy results show the presence of Mo(V). From XPS and ISS, molybdena was observed in a more aggregated form in Rh-Mo/Al₂O₃ than was the case for Mo/Al₂O₃ catalysts. This aggregation takes place during the calcination stage and is probably due to formation of mixed oxide MoRh₂O₆. The particle size of molybdena in Rh-Mo/Al₂O₃ is $\approx 20\text{\AA}$. Also the average shortest distance between the Mo(V) and the adsorbed CO estimated from solid-state NMR spectroscopy and the theory of nuclear relaxation is of the order of 5\AA .

The reaction studies, kinetics, characterization results and test reaction studies indicate that the synergistic effect of addition of Mo to Rh/Al₂O₃ on the overall activity and selectivity to oxygenates is due to a second hydrogenation site. This second hydrogenation site is partially reduced molybdena, which can activate hydrogen. This site is less poisoned by carbon monoxide than the rhodium metal crystallite and is in close proximity to the metal particle. Thus a dual-site mechanism can be envisioned, with CO being activated by rhodium and hydrogen either activated or stored by the partially reduced molybdena.

10.2 Recommendations for Future Work

The delplot analysis needs further development to incorporate the effect of transport limitations and thermodynamic constraints. Also, error propagation analysis, fractional rank delplot, recursive relationships for effective product rank for fractional order kinetics need further investigation. The rank of the product is same as the distance between the product node and the reaction node in reaction chemical graph theory. Because of the strong similarity between reaction chemical graph theory and delplot analysis, a more detailed look at the use of chemical graph theory in delplot analysis is warranted.

In this dissertation, the investigation was primarily focussed on the rhodium based catalysts and the activation of CO. In contrast, very little is known about activation of hydrogen in these systems. Hence structure-sensitive test reactions such as ethane hydrogenolysis could provide very useful information on the nature and the type of ensembles in Rh/Al₂O₃ and Rh-Mo/Al₂O₃ catalysts. Investigation of the role of carbon dioxide as a feed can provide interesting leads into the working of these catalysts as has already been done for methanol synthesis catalysts. Because of the recently reported breakthroughs in sulfided catalysts for oxygenate synthesis, the reactivity of sulfided Rh-Mo/Al₂O₃ catalysts also needs further investigation.

The nature and the distribution of oxide layers needs further investigation. Specifically, the problem consists of finding a probe molecule which can discriminate between the molybdenum oxide phase and alumina without adsorbing or disturbing the rhodium phase. Preliminary results in this laboratory have indicated that carbon dioxide is a good probe for discriminating between these oxide phases. The high pressure IR in conjunction with techniques to remove the strong gas phase CO peak could be of use to monitor surface species under reaction condition. The strong gas phase CO can be narrowed by the use of two-beam technique

to quench the rotational bands. The first beam is the IR beam and the second beam is a wide-range microwave source. The dynamic information obtained from relaxation in NMR-spectroscopy of the oxide probe has the potential of providing useful information of the spatial distribution of various components on the surface.

Sodium modified Rh/Al₂O₃ catalysts are not as promising as Rh-Mo/Al₂O₃ catalysts, because sodium lowers activity. Here again the major issue is how does sodium oxide distribute itself on Rh/Al₂O₃ catalysts. Substantial portion of the sodium is expected to bind to the bare alumina surface, however small amounts of sodium changes the activity of the catalysts. This small amount of sodium may not be detectable by spectroscopic techniques. Hence techniques which enhance the signal from modifiers near the metal crystallite should be investigated. Foremost among them is the use of probe molecules such as carbon dioxide to study oxides.

APPENDIX A

CALCULATIONS OF POSSIBLE TRANSPORT LIMITATIONS

This analysis shown in this appendix is based on local heat and mass transfer effects on the small particles. Many anomalous effects on small particles such as bypassing and agglomeration is still being developed.

A.1 Mass Transfer

A.1.1 Axial Dispersion

To find the effect of axial dispersion we use the Mears criterion. Mears[1] has shown that the axial dispersion effects are insignificant if

$$\frac{L}{d_p} > \frac{20n}{Pe_a} \ln\left(\frac{C_0}{C}\right) \quad (\text{A.1})$$

where

L = catalysts bed length

d_p = particle diameter

n = reaction order

Pe_a = Peclet number based on the effective diffusivity in the axial direction

C_0 = concentration of reactant in the feed stream

C = concentration of reactant in the exit stream

The support particles used were 60mesh-100 mesh. so lets use a conservative estimate of 0.025cm as the particle diameter. Froment and Bischoff[2] show that Pe_a lies between 1 and 2. Also, for calculations use the maximum conversion of 25%. $C/C_0 = 0.75$. Thus equation (A.1) reduces to

$$\frac{L}{d_p} > 6 \quad (\text{A.2})$$

But a typical amount of catalyst used is 0.6-1gm. and with a apparent density of 1gm/cc, the bed length is 2cm. Thus

$$\frac{L}{d_p} = 110 \gg 6$$

Hence the axial dispersion effects are insignificant under the conditions used.

A.1.2 Intraparticle Mass Transfer

The Weisz-Prater criterion will be first used to rule out intraparticle mass transfer effects[3]. The Weisz-Prater criterion rules out intraparticle mass transfer if

$$\Phi = \frac{(r_v)_{obs} d_p^2}{4D_e C_s^2} \gg 1 \quad (\text{A.3})$$

where

Φ = Weisz-Prater modulus

$(r_v)_{obs}$ = observed rate of consumption of a reactant

D_e = effective diffusivity

C_s^2 = molar concentration of fluid reactant on the solid surface

A typical $(r_r)_{obs}$ is $\approx 5 \times 10^{-4}$ gmole/lit-sec. The diffusivity of a gas can be estimated, however here we use the data reported in table 1.1 of reference [4].

$$D_{CO-H_2}P = 0.651 \text{ cm}^2 - \text{atm}/\text{sec at } 273K$$

Correcting it to temp of 498K and a pressure of 45 atm, we get

$$D_{CO-H_2} = 0.0356 \text{ cm}^2/\text{sec}$$

An approximate tortuosity factor τ and a void fraction will be used. A good estimate for τ is 4, and for θ is 0.6. Using this the effective diffusivity D_e is

$$D_e = \frac{D\theta}{\tau} \approx 0.005 \text{ cm}^2/\text{sec}$$

Also $C_{CO} = 0.5$ gmol/lit at 200C and at a partial pressure 10 atm.

Thus substituting the above variables in the Weisz-Prater criterion, we get

$$\frac{(r_r)_{obs}d_p^2}{4D_eC_{CO}} \approx 10^{-6} \ll 1$$

Thus there is no significant intraparticle concentration gradients. Since the Weisz-Prater modulus is much smaller than unity, the rough estimate of the variables is justified. The Weisz-Prater criterion has many exceptions, so to make sure we use the Thiele modulus method. The Thiele modulus is given by

$$\phi = \frac{d_p}{6} \sqrt{\frac{k_v}{D_e}} \quad (A.4)$$

The reaction can be considered to be nearly first order in hydrogen. Thus a conservative estimate of rate can be calculated from the overall rate and the hydrogen concentration. At a hydrogen partial pressure of 20atm, and temperature of 500K, the concentration of hydrogen is 0.5 gmol/liter. Using this concentration

of hydrogen and an approximate rate of 0.5×10^{-3} gmol/lit-sec, the first order rate constant can be calculated to be 1×10^{-3} sec⁻¹. Thus the Thiele modulus is given by

$$\phi = 2 \times 10^{-3} \ll 1$$

Since the Thiele modulus is much less than 1, we would expect the effectiveness factor given by equation (A.5) to be nearly unity.

$$\eta = \frac{1}{\phi} \left(\frac{3\phi \coth(3\phi) - 1}{3\phi} \right) \approx 1 \quad (\text{A.5})$$

Thus there is no significant intraparticle mass transfer resistance.

A.1.3 Fluid to Particle Mass Transfer

To estimate the fluid to particle mass transfer, we first have to estimate the viscosity of the gaseous mixture. The critical properties of CO and hydrogen are tabulated in table A.1.

The gas phase viscosity of CO and hydrogen at 1 atm can be found from a nomograph given in Perry's Handbook[4]. They are $\mu_{CO}(\text{at } 500K, 1\text{atm}) = 0.026\text{cP}$, and $\mu_{H_2}(500K, 1\text{atm}) = 0.015\text{cP}$. The viscosity at 30 atm and 500K is measured from the generalized reduced viscosities chart[5]. However, because the reduced temperature in both cases is much greater than one, the effect of given pressure increase(1 atm to 30atm) on the viscosity is negligible(within 10%). The mixture viscosity is calculated by using a simple molar mixing rule, for e.g., for a 1:2 CO:hydrogen gas the viscosity is 0.018 cP. The gas phase Reynolds number is given by

$$Re = \frac{d u \rho}{\mu} = 0.831$$

where

Table A.1: Properties of CO and hydrogen used in estimation of transport limitations

Property	Carbon Monoxide	Hydrogen
P_c	34.5	12.8
T_c	132.9	33.2
$P_r(30\text{atm})$	0.87	3.9
$T_r(500\text{K})$	3.76	15
P_{atm}	0.03	0.08
ω	0.049	-0.22

d = reactor diameter

u = superficial gas velocity

ρ = gas density

μ = gas viscosity

[Using a suitable correlation [6]

$$\epsilon_{jD} = \frac{\epsilon k_G P}{G_m} \frac{\mu}{\rho D_e}{}^{2/3} = \frac{0.357}{Re^{0.36}} \quad (\text{A.6})$$

where

ϵ = void fraction

k_G = gas side mass transfer coefficient

G_m = the mass velocity

Substituting the above parameters in equation (A.6), we get

$$k_G P = 0.00024 \text{ gmol/cm}^2 \text{ sec}$$

The maximum rate of mass transfer can be calculated by using the above gas side mass transfer coefficient and the equation (A.7).

$$r_{\text{mass transfer}} = k_G P a y_{CO} \quad (\text{A.7})$$

where

a = surface area per unit volume = $6/d_p$

y_{CO} = mole fraction of CO in feed

Thus the maximum rate of mass transfer at 45 atm total pressure and y_{CO} of 1/3 is

$$r_{\text{masstransfer}} \sim 0.02 \text{ gmol/cc} - \text{sec}$$

Recall that $r_{\text{observed}} = 10^{-6} \text{ gmol/cc} - \text{sec}$, thus

$$r_{\text{mass transfer}} \gg r_{\text{reaction}}$$

Hence there is no significant effect of fluid to particle mass transfer.

A.2 Heat Transfer

Before finding the effect on heat transfer processes on the overall rate, we need to estimate the thermal conductivity and the specific heat at the reaction conditions.

The thermal conductivity of hydrogen is found from fig 3-60 of Perry's Handbook, and is 63.57×10^{-5} cal/sec-cm-K at 500K and at 1 atm. Similarly, the thermal conductivity of CO is taken from the generalized reduced thermal conductivity chart in Reid, Prausnitz and Sherwood[5], and is 45.36×10^{-5} cal/sec-cm-K at 500K and 30atm. The corrections for thermal conductivity for hydrogen is negligible at 30atm because the reduced temperature is much larger than unity.

The psuedo-critical properties are needed to estimate specific heat of the mixture. The pseudo-critical properties are estimated by the method of Lee and Kesler[5], and are given below. $T_{cm} = 61.8K$, $P_{cm} = 21.6atm$. Thus the reduced temperature and pressure for 30atm and 500K for a 2:1 hydrogen:CO mixture is $(P_{rm}) = 1.4$ and $(T_{rm}) = 8.1$. The ideal gas heat capacity can be calculated from the tabulated virial coefficients[5]. The ideal gas heat capacity for the mixture is calculated from the individual ideal gas heat capacity.

$$C_{p,CO}^o = 6.994 \text{ Cal/gmol-K}$$

$$C_{p,H_2}^o = 7.124 \text{ Cal/gmol-K}$$

$$C_{p,m}^o = y_{CO}C_{p,CO}^o + y_{H_2}C_{p,H_2}^o = 7.037 \text{ Cal/gmol-K}$$

The mixture Pitzer's acentric factor is $\omega_m = -0.1313$. The zero and first order deviation function between the real specific heat and the ideal gas specific heat can be found from tabular listings of deviation functions in Reid, Prausnitz and Sherwood[5]. But, there are no listings above $T_r > 4$, in our case the reduced temperature is 7.5, however, the deviation function decreases with increase in reduced temperature. Thus a good upper bound on the zero and first order deviation function can be estimated at $T_r = 4$, and are

$$\left(\frac{C_p - C_p^o}{R} \right)^{(0)} = 0.010$$

$$\left(\frac{C_p - C_p^o}{R}\right)^{(1)} = 0.003$$

Thus, indeed the deviation functions are negligible as compared to the ideal gas heat capacity.

A.2.1 Fluid to Particle Heat Transfer

Now the fluid to particle heat transfer resistance can be evaluated. The best way to do this is to find the temperature drop across the "film". Equation (A.8) is an steady-state energy balance over the film.

$$n_p 4\pi r_p^2 (T_g - T_p^s) = (\Delta H) r_w W \quad (\text{A.8})$$

where

n_p is the number of particles in the bed

T_g = gas phase temperature

T_p^s = temperature at the surface of the catalysts particle

ΔH = heat of reaction

r_w = rate per unit weight of catalyst

W = weight of the catalysts

The heat transfer coefficient can be found by equating j_D and j_H . j_D was calculated while evaluating fluid to particle mass transfer. Thus the heat transfer coefficient was 11.4×10^{-5} cal/cm²-sec-K. The weight of the catalysts is 0.6 gm and there approximately 70000 particles of diameter 0.025cm in 0.6gm of catalysts. The average heat of reaction is 30kcal/gmol and the rate is 0.5×10^{-6} gmol·sec-gm. The gas phase temperature is assumed to be 500K. Substituting the above

parameters in the equation (A.8), we get

$$T_p^3 - 500 = 0.54K$$

Thus the fluid to particle heat transfer does not cause a significant increase in the temperature of the particle. However, these calculations assumed that the gas hourly space velocity was 1000 hr^{-1} . For lower gas hourly space velocity the temperature rise across the film may be substantial. The GHSV used in the runs described in chapter 8 was greater than 2000 hr^{-1} . The lowest GHSV used on Rh-Na/Al₂O₃ was 350 hr^{-1} , and here the temperature rise across the film is substantial.

A.2.2 Intraparticle Gradients

According to Mears[1], the intraparticle gradients are not significant when

$$\frac{qr d_p^2 E}{4kRT_0^2} < 0.75 \quad (\text{A.9})$$

where

q = heat of reaction

r = rate of reaction

k = thermal conductivity of the catalyst particle

E = activation energy

A good estimate of thermal conductivity of gamma-Al₂O₃ is 7×10^{-4} cal/cm-sec-K[6]. Also chapter 8 shows that the activation energy for overall rate of reaction is approximately 21 Kcal/gmole. Substituting the above parameters in

equation (A.9) gives

$$0.0056 \ll 0.75$$

Hence the intraparticle thermal gradients can be neglected.

REFERENCES

1. D.E. Mears, *Ind. Eng. Chem. Proc. Des. Dev.* 1971, 10, 541.
2. G.F. Froment and K.B. Bischoff, "Chemical Reactor Analysis and Design", John Wiley, New York, 1979.
3. P.B. Weisz and C.D. Prater, *Adv. Catal.* 1954, 6, 143.
4. R.H. Perry and C.H. Chilton, "Chemical Engineers' Handbook", McGraw-Hill, New York, 1973.
5. R.C. Reid, J.M. Prausnitz and T.K. Sherwood, "The Properties of Gases and Liquids", McGraw-Hill, New York, 1977.
6. C.N. Satterfield, "Mass Transfer in Heterogeneous Catalysis". MIT Press, Cambridge, Massachusetts, 1970.

APPENDIX B

SALIENT FEATURES OF THE THEORY OF RELAXATION OF NUCLEAR SPINS

In this appendix an introduction to the theory of relaxation of nuclear spins is given. Special emphasis is given to relaxation of nuclear spins in solids. First the effect of random magnetic field on the relaxation of nuclear spins is discussed. Here only the main results and their physical significance is discussed. The reader is referred to excellent reviews in this field[1-7].

B.1 Randomly Fluctuating Magnetic Field

The Schrodinger equation has to be transformed into the rotating frame of reference or the zeeman frame of reference. The time fluctuating Hamiltonian induces fluctuating magnetic fields in the system that relax the nuclear magnetic moment from β state to α states. This fluctuating magnetic field can be because of many reasons such as dipole-dipole interaction, anisotropic chemical shift interaction, indirect coupling, quadrupolar interaction, electron-nucleus interaction.

In this section, the most simple equation for T_1 would be derived. The details of this derivation are given in Gerstein and Dybowski[2].

Let us evaluate the spin-lattice relaxation time under a randomly fluctuating magnetic field

$$H_{total} = H_{zeeman} + H_1(t) \quad (B.1)$$

where $\mathbf{H}_1(t)$ is the randomly fluctuating magnetic field given by equation (B.2).

$$\mathbf{H}_1(t) = h_z(t)\mathbf{I}_z + h_y(t)\mathbf{I}_y + h_x(t)\mathbf{I}_x \quad (\text{B.2})$$

where $h_i(t)$ is the component of the randomly fluctuating magnetic field in direction i . The single particle probability of a state i can be expressed in terms of Zeeman Liouville operator \mathbf{U}_0 .

$$\mathbf{U}_0 = \exp(-i\mathbf{H}_0 t) \quad (\text{B.3})$$

Let \mathbf{P} be the single particle probability operator, then transformation of equation (B.3) into the rotating frame is given by equation (B.4).

$$i \frac{\partial \bar{\mathbf{P}}}{\partial t} = [\bar{\mathbf{H}}_1(t), \bar{\mathbf{P}}] \quad (\text{B.4})$$

$\bar{\mathbf{H}}_1$ is the randomly varying magnetic field in the zeeman interaction frame

$$\bar{\mathbf{H}}_1 = \exp(-i\mathbf{H}_0 t)\mathbf{H}_1(t)\exp(i\mathbf{H}_0 t) \quad (\text{B.5})$$

A series solution to equation (B.4) can be derived. The details of this derivation are given in Gerstein and Dybowski[2]. After many algebraic manipulations one obtains

$$\frac{\partial \bar{\mathbf{P}}}{\partial t} = -i[\bar{\mathbf{H}}_1(t), \bar{\mathbf{P}}(0) - \mathbf{P}_{eq}] - \int_0^t d\tau [\bar{\mathbf{H}}_1(t), [\bar{\mathbf{H}}_1(t-\tau), \bar{\mathbf{P}}(t-\tau) - \bar{\mathbf{P}}_{eq}]] \quad (\text{B.6})$$

Substituting $\bar{\mathbf{H}}_1(t)$ from equation (B.4) gives

$$\bar{\mathbf{H}}_1(t) = \exp(-i\mathbf{H}_0 t) [h_x(t)\mathbf{I}_x - h_y(t)\mathbf{I}_y - h_z(t)\mathbf{I}_z] \exp(-i\mathbf{H}_0 t) \quad (\text{B.7})$$

where $\mathbf{H}_1(t)$ is the randomly fluctuating magnetic field given by equation (B.2).

$$\mathbf{H}_1(t) = h_z(t)\mathbf{I}_z + h_y(t)\mathbf{I}_y - h_x(t)\mathbf{I}_x \quad (\text{B.2})$$

where $h_i(t)$ is the component of the randomly fluctuating magnetic field in direction i . The single particle probability of a state i can be expressed in terms of Zeeman Louiville operator U_0 .

$$U_0 = \exp(-i\mathbf{H}_0 t) \quad (\text{B.3})$$

Let P be the single particle probability operator, then transformation of equation (B.3) into the rotating frame is given by equation (B.4).

$$i \frac{\partial \bar{P}}{\partial t} = [\tilde{\mathbf{H}}_1(t), \bar{P}] \quad (\text{B.4})$$

$\tilde{\mathbf{H}}_1$ is the randomly varying magnetic field in the zeeman interaction frame

$$\tilde{\mathbf{H}}_1 = \exp(-i\mathbf{H}_0 t)\mathbf{H}_1(t)\exp(i\mathbf{H}_0 t) \quad (\text{B.5})$$

A series solution to equation (B.4) can be derived. The details of this derivation are given in Gerstein and Dybowski[2]. After many algebraic manipulations one obtains

$$\frac{\partial \bar{P}}{\partial t} = -i[\tilde{\mathbf{H}}_1(t), \bar{P}(0) - \bar{P}_{eq}] - \int_0^t d\tau [\tilde{\mathbf{H}}_1(t), [\tilde{\mathbf{H}}_1(t-\tau), \bar{P}(t-\tau) - \bar{P}_{eq}]] \quad (\text{B.6})$$

Substituting $\tilde{\mathbf{H}}_1(t)$ from equation (B.4) gives

$$\tilde{\mathbf{H}}_1(t) = \exp(-i\mathbf{H}_0 t) [h_x(t)\mathbf{I}_x + h_y(t)\mathbf{I}_y - h_z(t)\mathbf{I}_z] \exp(-i\mathbf{H}_0 t) \quad (\text{B.7})$$

Combining equations (B.6) with equation (B.7) we get

$$\begin{aligned} \frac{\partial \bar{\mathbf{P}}}{\partial t} &= i \sum_j h_j(t) \exp(i\mathbf{H}_0 t) \mathbf{I}_j \exp(-i\mathbf{H}_0 t) \cdot \bar{\mathbf{P}}(0) - \bar{\mathbf{P}}_{eq} \\ &\quad - \int_0^t d\tau \sum_j h_j(t) h_m(t-\tau) \\ &\quad \times \left[e^{i\mathbf{H}_0 t} \mathbf{I}_j e^{-i\mathbf{H}_0 t} \cdot \left[e^{i\mathbf{H}_0(t-\tau)} \mathbf{I}_m e^{-i\mathbf{H}_0(t-\tau)} \cdot \bar{\mathbf{P}}(t-\tau) - \bar{\mathbf{P}}_{eq} \right] \right] \end{aligned} \quad (\text{B.8})$$

Equation (B.8) applies to a single nuclear spin. However, experiments are done on macroscopic systems, where there is an ensemble of spin states. Hence equation (B.8) has to be ensemble averaged. Equation (B.9) gives the ensemble average where $\bar{\rho}$ is the density of spin states in the zeeman interaction frame

$$\frac{\partial \bar{\rho}}{\partial t} = i \sum_j h_j(t) \left[\bar{\mathbf{I}}_j \cdot \bar{\rho}(0) - \bar{\rho}_{eq} - \int_0^t d\tau \sum_{j,m} \overline{h_j(t) h_m(t-\tau)} \left[\bar{\mathbf{I}}_j \left[\bar{\mathbf{I}}_m \cdot \bar{\rho}(t-\tau) - \rho_{eq} \right] \right] \right] \quad (\text{B.9})$$

where

$$\bar{\mathbf{I}}_j = \exp(i\mathbf{H}_0 t) \mathbf{I}_j \exp(-i\mathbf{H}_0 t)$$

$$\bar{\mathbf{I}}_m = \exp(i\mathbf{H}_0(t-\tau)) \mathbf{I}_m \exp(-i\mathbf{H}_0(t-\tau))$$

If $h_i(t)$ are random functions $\overline{h_i(t)} = 0$ thus

$$\begin{aligned} \frac{d\bar{\rho}}{dt} &= - \int_0^t d\tau \sum_{j,m} \overline{h_j(t) h_m(t-\tau)} \\ &\quad \times \left[e^{i\mathbf{H}_0 t} \mathbf{I}_j e^{-i\mathbf{H}_0 t} \cdot \left[e^{i\mathbf{H}_0(t-\tau)} \mathbf{I}_m e^{-i\mathbf{H}_0(t-\tau)} \cdot \bar{\rho}(t-\tau) - \bar{\rho}_{eq} \right] \right] \end{aligned} \quad (\text{B.10})$$

If the $h_j(t)$ are completely uncorrelated, or if there is no cross-correlation between different h_j , then

$$\overline{h_j(t) h_m(t-\tau)} = 0, \text{ unless } j = m$$

thus

$$\frac{d\bar{\rho}}{dt} = - \int_0^t d\tau \sum_j \overline{h_j(t)h_j(t-\tau)} \times [e^{i\mathbf{H}_0 t} \mathbf{I}_j e^{-i\mathbf{H}_0 t}, [e^{i\mathbf{H}_0(t-\tau)} \mathbf{I}_m e^{-i\mathbf{H}_0(t-\tau)}, \bar{\rho}(t-\tau) - \bar{\rho}_{eq}]] \quad (\text{B.11})$$

Gerstein and Dybowski[2] show that

$$\frac{\partial \langle \mathbf{I}_z \rangle}{\partial t} = \text{Tr} \left(\frac{\partial \bar{\rho}}{\partial t} \mathbf{I}_z \right) \quad (\text{B.12})$$

Combining equations (B.11) and (B.12), gives equation (B.13).

$$\frac{\partial \langle \mathbf{I}_z \rangle}{\partial t} = \int_0^t d\tau \sum_j \overline{h_j(t)h_k(t-\tau)} \text{Tr} [[\mathbf{I}_z, \mathbf{I}_j], e^{i\mathbf{H}_0 t} \mathbf{I}_j e^{-i\mathbf{H}_0 \tau}] \times (\bar{\rho}(t-\tau) - \rho_{eq}) \quad (\text{B.13})$$

Equation (B.13) can be simplified to

$$\begin{aligned} \frac{d \langle \mathbf{I}_z(t) \rangle}{dt} = & - \int_0^t d\tau \overline{h_x(t)h_x(t-\tau)} \cos(\omega_0 \tau) \text{Tr} \mathbf{I}_z (\bar{\rho}(t) - \bar{\rho}_{eq}) \\ & - \int_0^t d\tau \overline{h_y(t)h_y(t)(t-\tau)} \cos(\omega_0 \tau) \text{Tr} \mathbf{I}_z (\bar{\rho}(t) - \bar{\rho}_{eq}) \end{aligned} \quad (\text{B.14})$$

Equation (B.14) can be simplified to

$$\frac{d}{dt} \langle \mathbf{I}_z \rangle = - \frac{1}{T_1} [\langle \mathbf{I}_z(t) \rangle - \langle \mathbf{I}_z \rangle_{eq}] \quad (\text{B.15})$$

where

T_1 is the spin-lattice relaxation time

$\langle \mathbf{I}_z \rangle$ is the observed magnetization in the direction of the field

This equation ((B.15)), also known as Bloch Equation, is in terms of observables only and was first proposed on a phenomenological basis by Felix Bloch.

where T_1 is given by

$$\frac{1}{T_1} = \int_0^{\infty} [G_x(\tau) - G_y(\tau)] \text{Cos}(\omega_0\tau) d\tau \quad (\text{B.16})$$

$$G_j(\tau) = \overline{h_j(t)h_j(t-\tau)} \quad (\text{B.17})$$

Thus the relaxation of nuclear magnetic spins in a fluctuating magnetic field follow a first order rate process with a time constant known as the spin-lattice relaxation time(T_1). The above proof shows the various important steps and the assumptions involved in them. The exact nature of the correlation function $G_x(\tau)$ would depend on the mode of relaxation: i.e.. whether the relaxation is caused by dipole-dipole coupling or by anisotropic chemical shift anisotropy or by any other possible mode.

For a general case of exponentially decreasing correlation function

$$G_j(\tau) = G_j(0)\exp(-\tau/\tau_j) \quad (\text{B.18})$$

Combining equations (B.17) and (B.18) gives (B.19).

$$\frac{1}{T_1} = G_x(0) \frac{\tau_x}{1 - \omega_0^2\tau_x^2} - G_y(0) \frac{\tau_y}{1 - \omega_0^2\tau_y^2} \quad (\text{B.19})$$

B.2 Scalar Coupling of Spins

The relaxation of nuclear spins by fixed paramagnetic species in space is a well-developed and complex subject. Abragam has given an excellent exposition of this subject. To understand the relaxation of the nuclei in solids, the scalar relaxation phenomenon is first considered.

A nuclear spin I in a system is subject to various types of couplings with its surroundings and with the other spins. These couplings are described by tensors, whose components are functions of lattice parameters. There are two effects of this coupling. The first-order effect, is because of the diagonal part of the coupling tensor given by equation (B.20), and causes chemical shift. In contrast, the second order effect is due to the traceless part of the coupling tensor. This traceless tensor vanishes on random rotation and its second order effect is to induce relaxation.

$$\mathbf{H}_{\text{coupling}} = \mathbf{I} \cdot \hbar \mathbf{A}_m \cdot \mathbf{S} \quad (\text{B.20})$$

Relaxation of nuclear spins by coupling can be easily understood by an example. The coupling tensor \mathbf{A} has well-defined components with respect to the molecular axis. But in a NMR experiment, the orientation of the nuclear spins is fixed with respect to the laboratory frame of reference. If the molecular axis is fixed with respect to the laboratory frame than the tensor components can be transferred using a similarity transform. If the molecule is subject to random rotations, then the tensor components become random functions of time and a relaxation mechanism is provided.

Abraham has shown that in solids, a second scalar relaxation takes place. This implies that the local magnetic field $\mathbf{A} \cdot \mathbf{S}(t) / \gamma_I$ produced by spin S and 'seen' by the spin I , fluctuates at a rate that is fast compared with the frequency Δ of the splitting it would produce among the energy levels of I , if it did not fluctuate. Then, the spin S is lumped with the 'lattice' with which it is assumed to be in equilibrium because of its short relaxation time. The perturbing Hamiltonian is $\hbar \mathbf{H}_1$ causing the relaxation of spin I is

$$\hbar \mathbf{H}_1 = \hbar \mathbf{A} \cdot \mathbf{I} \cdot \mathbf{S} = \hbar \sum_q \mathbf{F}^{(q)} \mathbf{A}^{(q)} \quad (\text{B.21})$$

where the spin operators $\mathbf{A}^{(q)}$ are

$$A^{(0)} = I_z, A^{(1)} = I_+ \text{ and } A^{(-1)} = I_-$$

and the lattice operators $F^{(q)}$ are

$$F^{(0)} = AS_z, F^{(1)} = \frac{1}{2}AS_- \text{ and } F^{(-1)} = \frac{1}{2}AS_+$$

It has been shown by many authors that raising and lowering operators are useful in the analysis and hence they are used. An analysis similar to the one described in the previous section yields

$$\frac{1}{T_1} = \frac{2A^2}{3} S(S-1) \frac{\tau_2}{1 + (\omega_I - \omega_S)^2 \tau_2^2} \quad (\text{B.22})$$

In the solid the vector between the NMR-active nucleus and the second spin S has a fixed orientation hence the dipolar coupling will be much more important than the scalar one. In most solids the electron resonance frequency is much larger than the electron line width (except at low fields). In these cases the above equation can be simplified to

$$\frac{1}{T_1} = \frac{2}{5} \gamma_S^2 \gamma_I^2 \hbar^2 S(S+1) \frac{\tau}{1 + \tau^2 \omega_I^2} \quad (\text{B.23})$$

If $\omega_I \tau = \gamma_I H_0 \tau \gg 1$, then equation (B.23) can be simplified to equation (B.24)

$$\frac{1}{T_1} = \frac{2}{5} \frac{S(S+1)}{\tau} \left(\frac{H_e}{H_0} \right)^2 \quad (\text{B.24})$$

Thus the spin-lattice relaxation time can be related to separation distance between spin S and spin I.

REFERENCES

1. A. Abragam. "Principles of Nuclear Magnetism". Oxford University Press, 1961, London.
2. B.C. Gerstein and C.R. Dybowski, "Transient Techniques in the NMR of Solids". Academic Press, 1985. New York.
3. A. Abragam, J. Combrisson and I. Solomon, C.R. Acad. Sci. 246. 1035, 1958.
4. N. Bloembergen. Physica, 15. 386. 1949.
5. P.G. deGennes. Phys. Chem. Solids. 3, 345, 1958.
6. J.M. Winter, C.R. Acad. Sci. 1959, 249, 2192.
7. R.V. Pound, J. Phys. Chem. 1953. 57, 743.

SATISFACTION GUARANTEED

NTIS strives to provide quality products, reliable service, and fast delivery. Please contact us for a replacement within 30 days if the item you receive is defective or if we have made an error in filling your order.

▲ **E-mail: info@ntis.gov**

▲ **Phone: 1-888-584-8332 or (703)605-6050**

Reproduced by NTIS

National Technical Information Service
Springfield, VA 22161

This report was printed specifically for your order from nearly 3 million titles available in our collection.

For economy and efficiency, NTIS does not maintain stock of its vast collection of technical reports. Rather, most documents are custom reproduced for each order. Documents that are not in electronic format are reproduced from master archival copies and are the best possible reproductions available.

Occasionally, older master materials may reproduce portions of documents that are not fully legible. If you have questions concerning this document or any order you have placed with NTIS, please call our Customer Service Department at (703) 605-6050.

About NTIS

NTIS collects scientific, technical, engineering, and related business information – then organizes, maintains, and disseminates that information in a variety of formats – including electronic download, online access, CD-ROM, magnetic tape, diskette, multimedia, microfiche and paper.

The NTIS collection of nearly 3 million titles includes reports describing research conducted or sponsored by federal agencies and their contractors; statistical and business information; U.S. military publications; multimedia training products; computer software and electronic databases developed by federal agencies; and technical reports prepared by research organizations worldwide.

For more information about NTIS, visit our Web site at <http://www.ntis.gov>.

NTIS

**Ensuring Permanent, Easy Access to
U.S. Government Information Assets**



U.S. DEPARTMENT OF COMMERCE
Technology Administration
National Technical Information Service
Springfield, VA 22161 (703) 605-6000
